

MEASUREMENTS OF THE ALKALI-METAL SPIN-DESTRUCTION RATE
AND SPIN-EXCHANGE RATE COEFFICIENT IN
Xe-Rb AND Xe-Cs SYSTEMS

By

ZAHRA ARMANFARD

A dissertation submitted in partial fulfillment of
the requirements for the degree of

DOCTOR OF PHILOSOPHY

WASHINGTON STATE UNIVERSITY
Department of Physics and Astronomy

DECEMBER 2023

© Copyright by ZAHRA ARMANFARD, 2023
All Rights Reserved

© Copyright by ZAHRA ARMANFARD, 2023
All Rights Reserved

To the Faculty of Washington State University:

The members of the Committee appointed to examine the dissertation of ZAHRA ARMANFARD find it satisfactory and recommend that it be accepted.

Brian T. Saam, Ph.D., Chair

Peter W. Engels, Ph.D.

Brian A. Collins, Ph.D.

ACKNOWLEDGEMENTS

In the pursuit of knowledge and the exploration of the vast realms of atomic physics, this dissertation stands as a testament to the unwavering support, guidance, and mentorship I have received throughout this challenging yet rewarding journey.

First and foremost, I express my deepest gratitude to Dr. Brian Saam, whose guidance in the laboratory became the catalyst for my scientific transformation. Dr. Saam, you not only took the risk of welcoming me into your fold but also exhibited remarkable patience as I navigated the intricate pathways of research. Your mentorship went beyond the realms of academia; you nurtured my scientific curiosity, allowing me to face my fears, and fostering an environment where my strengths could flourish. I started as a novice, a girl unfamiliar with the names of tools, and under your guidance, I transformed into a skilled scientist and a capable handyman. Your belief in my potential provided the fertile ground for me to grow intellectually, emotionally, and personally. I am now equipped not only to enter the scientific world but to thrive and contribute meaningfully.

My gratitude extends to Dr. Adnan Nahlawi, a co-advisor, in every sense. Dr. Nahlawi, you mirrored Dr. Saam's role in shaping my academic trajectory. Your willingness to share knowledge, answer questions, and work side by side with me in the laboratory has been invaluable and got me through the rough times. Throughout my Ph.D. journey, your presence has been a constant source of inspiration and guidance,

I cannot thank you enough for that.

I extend my appreciation to my lab mates. Each of you has played a pivotal role in my growth, and I have learned immeasurable lessons from our shared experiences in Dr. Saam's lab.

To my committee members, Dr. Engles and Dr. Brian Collins, I am indebted to your bold roles in facilitating my understanding of the tools and fundamentals of my work. The courses you offered paved the way for my academic success.

A heartfelt shout-out to the entire WSU physics department for fostering a kind and friendly environment that has contributed to my academic and personal development, and to all my friends who made my time in Pullman memorable.

To my parents Ali and Parvin and brothers Mohammad and Hossein, I owe my deepest gratitude. Your support, sacrifices, and unconditional love have been the bedrock of my existence. You sacrificed your own aspirations to ensure that I could pursue my passion and desires. Dad, your tireless dedication is the foundation of where I stand today. Your inspirational words at the start of each academic year, urging me to be mindful of time, resonate now more than ever. It's surreal to realize that six years have passed since I left home to pursue my Ph.D. I assure you, I've imbibed your wisdom and endeavor to use my time wisely. Mom, you are my guiding light, my confidante, and my everything. Without your unwavering support, I might have faltered in the third year. Thank you for not only giving me life but being

present for every moment, offering encouragement that carried me through. To my brothers, my cherished protectors, you are my pillars of strength and the source of my peace of mind. Your advice and support have been indispensable, and I couldn't have embarked on this journey without you. Your guidance has led me down the right path, and my success is a reflection of the love and sacrifices you have made.

This Ph.D. in atomic physics is not merely an academic achievement; it is the culmination of tireless effort, sacrifice, love, and unbridled passion. I carry with me the lessons and support of those who have been instrumental in this journey, and I embark on the next chapter with a profound sense of gratitude and purpose.

This research was funded by the National Science Foundation. I express gratitude to the National Science Foundation and Polarean, our valued goali partner, for their support in this endeavor.

MEASUREMENTS OF THE ALKALI-METAL SPIN-DESTRUCTION RATE
AND SPIN-EXCHANGE RATE COEFFICIENT IN
Xe-Rb AND Xe-Cs SYSTEMS

Abstract

by Zahra Armanfard, Ph.D.
Washington State University
December 2023

Chair: Brian T. Saam

Despite the practice of noble gas spin-exchange optical pumping (SEOP) since 1960, various fundamental aspects of this method, including the values of the spin-destruction rate, numerous elements of alkali-metal polarization, and spin-exchange coefficient, still need to be explored. The mechanisms governing ^{129}Xe polarization, and the spin-exchange efficiency have also been noted as areas of exploration. This thesis explains the results of our efforts to measure these features and initiates an understanding of some of these mysteries. This document includes measurements of the alkali-metal spin-destruction rate, alkali-metal-Xe spin-exchange rate coefficient, and spin-exchange efficiency. We made a comparison between Xe-Rb and Xe-Cs systems by comparing the SEOP efficiency for the two systems to understand which

alkali-metal can be a better partner for polarizing Xe. The results show that Xe-Cs system has $\sim 35\%$ higher spin-exchange rate coefficient and $\sim 30\%$ higher spin-destruction rate than Xe-Rb system, resulting in a slightly better SEOP efficiency for Xe-Cs system than Xe-Rb system.

TABLE OF CONTENTS

	Page
ACKNOWLEDGEMENTS	iii
ABSTRACT	vi
LIST OF FIGURES	xi
LIST OF TABLES	xix
CHAPTER	
1. INTRODUCTION	1
Motivation	1
Hyperpolarized Noble Gas	3
Hyperpolarization Techniques	4
Structure of this Thesis	10
2. GENERAL THEORY OF SEOP	13
The Hyperfine Structure of Alkali-Metal Atoms	13
Optical Pumping	19
Anisotropic Excitation	21
Repopulation Pumping	22
Depopulation Pumping	23
Magnetic Resonance	29
The spin-exchange and spin-destruction Interactions	35

Collisional Hamiltonian	35
Alkali-Metal-Alkali-Metal Binary Collision	36
Alkali-Metal-Gas Binary Collision	37
Molecular Formation	37
3. GENERAL APPARATUS	42
Cell Fabrication	45
Oven	52
Magnetic Fields	53
Static Magnetic Field	53
The Oscillating Magnetic Field	55
Pump Laser	59
Optical Detection and Probe laser	62
4. SPIN-DESTRUCTION RATE MEASUREMENTS	66
Introduction	66
Theory	68
Alkali-Metal Polarimetry	70
Alkali-Metal Relaxation Rate Measurement	73
Experimental Setup and Procedure	87
Results and Analysis	96
Conclusion	106

5. SPIN-EXCHANGE RATE COEFFICIENT MEASUREMENTS	108
Introduction	108
Theory	110
The Noble Gas Density	117
The Noble Gas Polarization	117
The Alkali-Metal Back Polarization	120
Experimental Setup and Procedure	121
Results and Analysis	134
Conclusion	143
6. SUMMARY AND CONCLUSION	145
REFERENCES	154

LIST OF FIGURES

	Page
2.1 Diagram of ^{87}Rb in an external magnetic field, showing the Zeeman effect and hyperfine sublevels.	15
2.2 ^{87}Rb ground state hyperfine energy levels vs. the magnetic field. The top manifold is $F = 2$, and the bottom manifold is $F = 1$. The lines show the hyperfine states, where they are labeled as F and m_F for small fields and m_J and m_I for large fields. At low fields, the energies are linear. As we move toward higher fields, the energy levels become nonlinear with the field [40].	18
2.3 Schematics of anisotropic optical excitation, in this method, the $m = 0$ sublevel of the excited states gets populated using a laser. The pump light polarization direction defines the quantization axis [42].	22
2.4 Depopulation optical pumping of the alkali-metal atom with the assumption there is no nuclear spin. The alkali-metal atoms are optically pumped from $(m_j = +\frac{1}{2})$ states by D_1 , left circularly polarized light (σ^-), inducing selection rule $\Delta m = -1$ to the possible transition . The excited state population reaches equilibrium by collisional mixing of alkali-metal atoms with each other and with buffer gases, and then N_2 acts as quenching gas to help the excited atoms to have a nonradiative decay resulting in population accumulation in one sub-level of the ground state $(m_j = -\frac{1}{2})$	24
2.5 Optical pumping of ^{87}Rb with left circularly polarized light while it is placed in an external magnetic field ($B_0 = 28$ G). The thin arrows show the allowed transition based on the selection rule $\Delta m = -1$, and the bold arrows show the decay of atoms to the ground state sublevels. This optical pumping results in populating the $ 2, -2\rangle$ sub-level because it is the only sub-level for which there is no allowed transition to the excited states.	26
2.6 Precession of spins about the magnetic field at Larmor frequency. . .	32
2.7 Motion of spins in the rotating frame about B_{eff}	33

3.1	spin-destruction rate measurement setup: The polarizing beam splitter and balanced photodetectors are labeled PBS and BPD, respectively. Switching between Rb and Cs lasers was achieved using a sliding mirror in front of the Cs laser. The symbols labeling the wire going to the EPR coils and the wire fed into the spectrometer represent the generated pulses and collected free induction decays FIDs. The inset at the lower left corner shows the timeline of the pulse sequence and the periodic light blocking (dark).	42
3.2	Frequency shift measurement setup: 1) 795 and 895 nm pump lasers for Rb and Cs respectively, narrowed to ~ 0.3 nm. 2) 852 nm Cs and 780 nm Rb probe lasers detuned by ≈ 0.6 nm for optical detection of alkali-metal polarization; the probe beam after the cell is focused onto fast-balanced photodiodes. 3) The EPR coil, which is positioned in the normal direction to the main static field. 4) The NMR coil, which is a surface coil placed right below the cell and is driven by a frequency generator and an audio amplifier to produce RF pulses at the noble gas nuclear resonance frequency in order to destroy the noble gas polarization.	43
3.3	Pyrex manifold.	46
3.4	Gas handling and vacuum system.	47
3.5	Schematic of the gas handling system. A glass blower makes the manifold containing the cells, and then it is attached to the vacuum system, and the volumes are measured. An ampule containing about 1 gram of alkali-metal is introduced into the retort. Subsequently, a section of the manifold containing the cells is sealed, and heating is applied while keeping the Turbo pump operational for a duration of several days. The heat facilitates the transfer of the alkali-metal into the cells. Precisely measured volumes are then filled with enriched Xe at a pre-determined pressure, after which the Xe is frozen into the cells using liquid nitrogen (LN ₂). Next, the manifold is filled with ⁴ He and N ₂ . The cell is submerged in LN ₂ , and a torch is used to melt through the pull-off, detaching the cell from the manifold.	49
3.6	Sample cell containing alkali-metal and desired gases.	50

3.7	Schematic of cell volume measurement using Archimedes principle. Where F_b , m , and V_c are the buoyant force, mass, and volume of the cell, respectively, and F_B , M , and V_w are the buoyant force, mass, and volume of the weight. T and T_s are the string forces.	51
3.8	spin-exchange oven.	53
3.9	Helmholtz coils producing the static magnetic field $B_0 \sim 28$ G and $B_0 \sim 46$ G, being water cooled using copper tubes and room-temperature chiller.	54
3.10	Tuning circuit: to tune the EPR coil to resonate at the alkali-metal hyperfine frequency and to be impedance matched with the amplifier.	56
3.11	Tuning circuit: for spoiling the Q of the EPR coil while being tuned to the EPR frequency and impedance matched with the output impedance of the amplifier, one can add a resistor parallel to the inductor to reduce the current to the inductor.	58
3.12	^{87}Rb FID signal (figures on the right) and spectrum (figures on the left) which is the result of FFT on the FID before (top figures) and after (bottom figures) spoiling the Q of the EPR coil. The ringdown was introducing noise to the FID signal (top left figure) and it was distorting the baseline of the spectrum (top right figure). After spoiling the Q the spectrum baseline issue got resolved (bottom right figure).	59
3.13	Schematic of narrowing a diode laser array using a Littrow cavity. . .	61
3.14	Picture of our pump laser optical table. Elements A-D show the narrowing arm and elements F-I show the pumping arm. ‘A’ is a $1/2$ wave plate to adjust the amount of light that goes to each arm. ‘B’ is a polarizing beam splitter that splits the beam in the directions of the narrowing and pumping arms. ‘C’ is a spherical lens with a 50 mm focal length and 50 mm diameter. ‘D’ is a spherical lens with a 100 mm focal length and 100 mm diameter. ‘F’ is a set of mirrors on a rotational base, changing between Rb and Cs lasers. ‘G’ is a $1/4$ wave plate to change the linearly polarized laser beam to a circularly polarized beam. ‘H’ is a spherical lens with a 50 mm focal length and 100 mm diameter to expand the beam and reflect it on the cell. ‘I’ is an optical chopper for measurements in the dark.	62

3.15	The schematics of our detection setup.	63
3.16	Picture of our detection setup.	64
4.1	^{87}Rb spectrum with high polarization and in the presence of ~ 28 G magnetic field, all the resonance peaks are well resolved.	74
4.2	Sample pulse sequence for Rb. The sequence starts with a fixed delay of $\sim 150 \mu\text{s}$ (columns 1 and 2) as a warm-up time for Tecmag. Next, the delay table for the chopper (column 3) starts. The Tecmag receives the trigger from the chopper and will continue the pulse sequence based on the delay table entries ($1000 \mu\text{s}$ - $8000 \mu\text{s}$ in the case of Rb and $1000 \mu\text{s}$ - $12000 \mu\text{s}$ in the case of Cs with step size $100 \mu\text{s}$). After the delay time, the receiver window opens (column 5), since we do optical detection, the detection part is decoupled from the RF excitation allowing us to open the detection window even before the pulse comes. Then the pulse with a specific pulse width and amplitude is sent to the RF amplifier and then the corresponding FID signal is received from the photodetector. This sequence repeats based on the number of scans and the entries of the delay table for the chopper.	90
4.3	Rb spectrum after applying a $\pi/2$ pulse. The top figure is from a simulation being done in MatLab, and the bottom figure is an experimental Rb spectrum after applying a $\pi/2$ pulse.	91
4.4	The relaxation in the dark measurement using pulsed EPR. The optical chopper runs at 40 Hz and triggers the Tecmag by sending a TTL pulse to start the pulse sequence. Tecmag sends the RF pulse to the Tomco amplifier to get amplified, and after amplification, it is sent to the EPR coil to generate the oscillating magnetic field that will excite the spins. Larmore precession of the spins is detected via Faraday rotation of the probe beam through the balanced photodetectors and is sent to Tecmag. We process the FID signals using TNMR software.	93
4.5	The figure on the top shows all the 70 Rb spectra as a result of relaxation in the dark measurement using the optical chopper to detect the Rb polarization decay in the course of time. The bottom left figure is the first spectrum, which was taken in the light, and the bottom right figure is the spectrum corresponding to ~ 6 ms delay time in the dark.	94

4.6	The figure on the top shows all the 110 Cs spectra as a result of relaxation in the dark measurement using the optical chopper to detect the Cs polarization decay in the course of time. The bottom left figure is the first spectrum, which was taken in the light, and the bottom right figure is the spectrum corresponding to ~ 6 ms delay time in the dark.	95
4.7	Sample FID for Rb, this FID was taken while the pump laser was on.	96
4.8	Plot of the area under the resonance peaks vs. time for Rb (left) and Cs (right) based on the spectra taken from the measurements in the dark.	96
4.9	Sample Rb (a) and Cs (b) polarization decay and single exponential fitting procedure to get the electron spin-relaxation rate γ_A . The figures on the left show the sample decay transient, and the figures on the right show the fitting procedure of fitting the transient with single exponential decay while eliminating points from the beginning of the transient until the time constant of the single exponential decay stays unchanged within its error.	97
4.10	Rb and Cs measured spin-relaxation rate γ_A vs. total gas density. . .	98
4.11	Rb and Cs measured relaxation rate γ_A vs. temperature.	100
4.12	Rb and Cs electron-randomization rate Γ_A vs. total density.	102
4.13	Rb and Cs measured relaxation rate γ_A vs. total density for fixed gas composition 94% ^4He , 3% N_2 and 3% Xe at 130°C . The blue line is Nelson and Walker's model adjusted for Rb under our experimental conditions of 3% Xe and 130°C temperature. The red line is what Nelson and Walker's model would predict in the case of Cs under our experimental conditions.	104
5.1	Rb spectra from the relaxation in the dark measurement. Shows the polarization decay of the alkali-metal atom as the delay time or, correspondingly, the time spent in the dark increases.	124
5.2	Cs spectra from the relaxation in the dark measurement. Shows the polarization decay of the alkali-metal atom as the delay time or, correspondingly, the time spent in the dark increases.	125

5.3	The figure on the top left shows the Rb spectrum in the light, and the top figure on the right shows the Rb spectrum after being in the dark for 10 ms. The figures on the bottom show the Cs spectrum in the light (left) and Cs spectrum after being 10 ms in the dark (right). . .	126
5.4	Rb polarization decay vs. time as a result of the measurement in the dark. The value of polarization at each timestamp is calculated by integrating the total area under the corresponding spectrum and using the polarization in the light and its area as a reference to calculate the polarization value.	127
5.5	Cs polarization decay vs. time as a result of the measurement in the dark. The value of polarization at each timestamp is calculated by integrating the total area under the corresponding spectrum and using the polarization in the light and its area as a reference to calculate the polarization value.	128
5.6	Rb and Cs frequency shift measurement schematics and setup in our lab. For measuring the alkali-metal frequency shift, the VCO provides the RF signal and sends it to the RF amplifier, and then the EPR coils to generate the oscillating magnetic field B_1 to excite the alkali-metal spins. The Faraday rotation signal from the photodiode is sent to an RF mixer to mix with the reference signal and get demodulated to an audio frequency. The signal from the mixer gets amplified, and then it is fed to the lock-in amplifier, which is referenced to the modulated frequency from the audio source. The lock-in amplifier generates the error signal based on the derivative of the EPR absorptive peak, and this error signal gets processed using the adder circuit. Then, it is sent back to the VCO, which will output an RF frequency to make the lock-in amplifier output voltage zero. This frequency is shown on the frequency counter. Using the frequency generator and the home-built RF pulse generator, a train of $\sim \pi/2$ pulses is sent to the NMR coil to flip the Xe nuclear spins and saturate them to generate the maximum change in the magnetic field that the alkali-metal electron spins sense and hence get the maximum frequency shift.	130
5.7	The frequency shift measurement electronics used in our laboratory. .	131

5.8	Rb and Cs sample Frequency Shift. The frequency counter dwell time was 500 ms. The VCO was locked to the EPR frequency. We allowed the system to become fully polarized and reach equilibrium while the optical chopper was on. Then, using an RF pulse generator, we sent a train of pulses to the NMR coil to destroy the Xe magnetization, which changed the magnetic field sensed by the alkali-metal electron and resulted in the EPR frequency shift. We kept sending the pulses until the Xe magnetization was fully destroyed and the alkali-metal EPR frequency was stable.	133
5.9	Rb and Cs polarization decay single exponential fit procedure. Points were progressively eliminated from the beginning of the decay transient, and the fit was done until the value of the relaxation rate reached a plateau (figures on the right). The single exponential time constant and the Y_0 values from the fit were recorded as the alkali-metal spin-relaxation time and back polarization.	135
5.10	Rb polarization decay vs. time, the Xe polarization was destroyed by a train of $\pi/2$ pulses throughout the whole decay to make sure there is no source of polarization to repolarize Rb.	136
5.11	Rb polarization decay vs. time, for both cases of having polarized Xe and not having polarized Xe during the relaxation in the dark measurement, on top of each other. It can be seen that in the case of having no polarized Xe, the Rb polarization decays to zero, but in the case that we have polarized Xe, Rb polarization decays to a non-zero level, which indicates the equilibrium state that it reaches with polarized Xe.	137
5.12	Rb and Cs frequency shift calculation. About 10 seconds before and after the shift, corresponding to about 20 points on each side, were chosen to be averaged to get the EPR frequencies before and after the shift. The shifts were calculated by subtracting these two frequencies, and the errors were based on the standard deviation of the chosen points.	138
5.13	Xe-Rb and Xe-Cs spin-exchange rate coefficient vs. $1/\text{total density}$. The parameters of the linear fit will provide us with information about the contributions of binary collisions and van der Waals molecules to the spin-exchange process.	141

5.14 Spin-exchange rate coefficient for Xe-Rb and Xe-Cs systems vs. $1/\text{total}$
density on the same graph. It suggests that at any corresponding total
density and respective temperatures k_{se} for Xe-Cs system is larger than
Xe-Rb system. 142

LIST OF TABLES

	Page
1.1 Values of measured spin-destruction rate γ_A and electron-randomization rate Γ_A for Xe-Rb and Xe-Cs systems.	11
1.2 Calculated values of spin-exchange rate coefficient k_{se} and SEOP efficiency η_{se} for Xe-Rb and Xe-Cs systems.	12
4.1 Volume and gas pressures of the eight cells, gas pressures are measured at room temperature $\sim 20^\circ$ C. Xe gas we used in our cells is enriched to 90% ^{129}Xe . The errors on the pressures and cell volumes are $\sim 4 - 5\%$ and $\sim 2\%$, respectively.	87
4.2 The RF pulse configuration for different alkali-metals in the relaxation in the dark measurement.	92
4.3 Values of measured spin-destruction rate γ_A , which comes from the single exponential decay fit of the alkali-metal polarization decay and electron-randomization Γ_A values which are related to γ_A through the paramagnetic coefficient $\Gamma_A = (1 + \bar{\epsilon}) \gamma_A$	99
4.4 Values of measured spin-destruction rate γ_A , for cells 309A and 310A with the fixed total density of ~ 1.5 amagat containing Rb and Cs respectively, at three different temperatures to understand the effect of temperature on the spin-relaxation rate of the alkali-metal atoms. .	99
4.5 Rb and Cs parameters that are needed to determine the fundamental decay rates γ_{Rb} and γ_{Cs} according to Eq. 4.46.	103
4.6 Rb and Cs parameters used to plot the solid lines of Fig. 4.13.	105
5.1 The values of constants in Eq. 5.5. The values of the gyromagnetic ratios for the alkali-metal atoms are the corrected values based on the effect of the static magnetic field.	128

5.2	Values of measured alkali-metal frequency shift $\Delta\nu_A$, spin-destruction rate γ_A , electron-randomization rate Γ_A , and back polarization P_A from polarized Xe, which come from the single exponential fit of the alkali-metal polarization decay and frequency shift measurements.	139
5.3	Calculated values of spin-exchange rate coefficient k_{se} and steady-state Xe polarization P_{Xe} using the measured values in table 5.2, the constants and parameters in table 5.1 and Eqs. 5.10 and 5.5.	139
5.4	Calculated values of spin-exchange efficiency η_{se}	144

Dedication

dedicated to

My Beloved Parents

and

My cherished brothers.

CHAPTER 1

INTRODUCTION

1.1 Motivation

Numerous physics research fields frequently employ optically pumped alkali-metal vapors and nuclear spin-polarized noble gases. Optical pumping is being used more often in various sectors, including atomic magnetometers and optically pumped atomic clocks [1, 2]. Additionally, it has become more common to create samples with strongly polarized nuclei using the spin-exchange method between optically polarized alkali-metals and noble gases like ^3He or ^{129}Xe . Numerous scientific techniques use the high nuclear spin polarization values reached in hyperpolarized noble gases, including atomic magnetometers, spin filters, atomic gyroscopes, searches for atomic electric dipole moments, and tests of fundamental symmetries [3, 4, 5]. They also have a variety of potential uses in the fields of biomedicine and clinical fields [6, 7, 8, 9].

Hyperpolarized Gas MRI, a brand-new type of magnetic resonance imaging (MRI) created in 1994 [6], has been practical for imaging the functional lungs. This technology uses pre-polarized noble gas, such as ^3He or ^{129}Xe , created via the spin-exchange Optical Pumping (SEOP) technique, in contrast to conventional MRI, which uses proton thermal polarization. Magnetization can be utilized to obtain an MRI image when these polarized noble gases are inhaled. Despite the low physical density of the

gas, noble gases have substantially more significant polarization than water thermal polarization, which results in a significant MR signal size that allows for clear viewing of the lung airspaces. Interestingly, the noble gas polarization is unaffected by the B_0 holding field strength, allowing for much lower field strengths to be used for MRI [10]. This lowers the cost of the scanner while providing unique benefits, including a more uniform holding field and improved metal penetration. Simpler solenoids can now be used in place of large superconducting magnets. He and Xe are the two most popular noble gases for hyperpolarized gas MRI. The latter is especially intriguing because Xe is a lipophilic gas that can diffuse into the bloodstream and allow hyperpolarized ^{129}Xe to image bodily areas other than the lungs [10].

For these hyperpolarized gases to be used in practice, it is essential to understand their properties, prepare them, store them, and transport them to the subject. In addition to being biologically compatible, a hyperpolarized gas must be stable for a sufficient amount of time before being transported to a sample or target organ for imaging or spectroscopy. Because of this, only a few selections of gases can be employed as hyperpolarized agents, but it's crucial to consider practical constraints while working with these gases to preserve and benefit from their hyperpolarization [10]. The amount of time that polarization is maintained after the drug is delivered is a helpful method for establishing contrast, along with other significant aspects like density, position, mobility, spectrum frequency, and signal behavior resulting from a

chemical interaction [11].

To create hyperpolarized ^{129}Xe , a common technique is SEOP [12, 13]. Using circularly polarized laser beams, SEOP polarizes the nuclear spin of ^{129}Xe by polarizing the valence electrons of alkali-metal atoms. K and Cs are potential substitutes for Rb, the alkali-metal now most frequently used to polarize ^{129}Xe . According to [13, 14], the spin-exchange mechanism happens during alkali-metals- ^{129}Xe van der Waals molecules formation and binary collisions. For molecular formation, a third body must be present. The polarization of ^{129}Xe depends critically on the constants associated with these mechanisms, such as the spin-exchange rate, spin-destruction rate, and efficiency. The polarization of ^{129}Xe can, therefore, be optimized by understanding these constants for various alkali-metals.

1.2 Hyperpolarized Noble Gas

Nuclei with nuclear spin polarization higher than that anticipated by Curie's law in thermal equilibrium are said to be hyperpolarized. Different methods for creating nuclear hyperpolarization are studied in the field of dynamic nuclear polarization [10].

Nuclear magnetism is incredibly weak. For instance, the magnetic moment of a ^{129}Xe nucleus is over 2300 times smaller than the magnetic moment of a single electron [15], resulting in significantly weaker nuclear magnetic resonance (NMR) signals than their equivalent electron resonance signals. The maximum thermal equilibrium nuclear polarizations that may be attained are typically on the order of 10^{-6} , even

with large magnetic fields. In other words, only a small percentage of particles contribute to the signal, making the NMR signal substantially weaker than the electron resonance counterparts. Despite this, due to their high particle density, which can be as high as 10^{23} atoms in just a few milliliters, NMR can create discernible signals in a variety of solids and liquids [15].

On the other hand, the gas phase's physical characteristics make it more suitable for applications involving hyperpolarized nuclei. At standard pressure and temperature, an ideal gas has a density of 2.69×10^{19} atoms/cc, which is three orders of magnitude smaller than the typical liquid density [15]. As a result, gas-phase samples in thermal equilibrium produce weaker signals due to low density and take longer to acquire. To overcome this density restriction, hyperpolarization techniques are used to enhance the polarization of the gas and increase the number of particles that contribute to the signal. Nuclear polarization can be improved using a variety of techniques, some of which have the potential to increase polarization by up to 100,000 times. In order to overcome the low density of gas-phase samples, nuclear polarizations of 80% or higher can be produced, yielding signals equal to or even stronger than those obtained from thermally polarized solid samples [15].

1.3 Hyperpolarization Techniques

Critically significant are the hyperpolarization techniques. Although these techniques were primarily created for physics or chemistry fundamental research, they are

currently being applied in research on a larger scale. The amount and polarization of hyperpolarized gases that can be created and the alternatives for these gases determine how well hyperpolarization techniques perform in various applications. Noble gases are the most frequently employed research agents, but tiny hydrocarbons and gases made of small molecules also have potential. The following techniques are the most used for producing hyperpolarized gases [10]:

- Dynamic nuclear polarization (DNP),
- Metastability exchange optical pumping (MEOP),
- Parahydrogen-induced polarization (PHIP),
- Spin-exchange optical pumping (SEOP),

Understanding how each approach functions is crucial for successfully integrating them into applications involving hyperpolarized gases. Each approach has benefits and drawbacks.

DNP takes advantage of the fact that unpaired electrons can be subjected to extremely low temperatures and powerful magnetic fields, generally reaching several Tesla, to achieve a significant degree of polarization. Nuclear spin polarization increases significantly after this polarization transfer to nuclear spins via dipolar or scalar couplings. In order to inject the required unpaired electrons into a sample, persistent radicals are typically utilized [16].

The dissolution DNP technique, known as d-DNP, is typically applied to tiny molecules. This method is based on the cross effect, a mechanism that involves two electrons and one nucleus and causes three spins to interact. Microwaves drive the electron spin transitions in this process, and the energy required to flip the nuclear spin is comparable to that needed to flip the electron spin [17, 18]. The d-DNP hyperpolarizer device was created in 2003 [16]. There are three essential components to the apparatus [11]:

- A superconducting magnet that establishes the magnetic field strength,
- A helium cryostat that cools the sample to very low temperatures,
- A microwave device that polarizes nuclear spins by transferring polarization from unpaired electron spins.

The DNP approach may successfully hyperpolarize ^{129}Xe by homogeneously mixing Xe with radical agents and a cosolvent, such as ethanol or propanol [19]. Sublimation DNP is the process by which the hyperpolarized ^{129}Xe is transformed from its solid state into a pure gas. Despite the fact that the polarization levels for ^{129}Xe are frequently lower than those that may be obtained with SEOP polarizers, advancements in DNP technology may allow for the polarization of ^{129}Xe to be almost 100% [11].

MEOP involves polarizing the spin angular momentum of an atom's metastable

state using optical pumping. The electron and nuclear spins of several atoms, including ^4He , ^3He , ^{21}Ne , ^{83}Kr , and ^{131}Xe , have been successfully polarized using this technique. While optical pumping had previously been used to polarize the electron and nuclear spins of alkali atoms and mercury [20], it wasn't until 1960 that it was used to polarize the electronic $^4\text{He } 2^3\text{S}_1$ metastable state [21] and then to polarize ^3He in 1962 [22].

In the case of ^{131}Xe , the atom is pumped by an electron beam as opposed to an optical source [23]. ^{129}Xe electronic states were polarized using the MEOP technique, but it did not lead to nuclear polarization, most likely because powerful nuclear relaxation mechanisms were present [24].

It is necessary for all H_2 molecules to be in the state $J = 0$ for there to be 'para-hydrogen' or para- H_2 , which is an antisymmetric singlet spin state. On the other hand, 'ortho-hydrogen', a triplet nuclear spin state, requires all H_2 molecules in the antisymmetric $J = 1$ state [10]. However, para- H_2 's singlet state cannot be detected by NMR as a pure spin order. Instead, through PHIP, para- H_2 generates hyperpolarized gases. By adding para- H_2 in pairs to an unsaturated precursor molecule, this technique breaks the symmetry, and the spin order created by the para- H_2 singlet state can be converted into detectable nuclear spin polarization [10]. The unsaturated bond must be structurally asymmetrical for this process to succeed and for the resulting nascent ^1H locations to be magnetically different [25]. Although the PHIP

approach has been known for a while, it has only recently proven practical to produce hyperpolarized gases on a wide scale by using effective heterogeneous catalysts that encourage significant pairwise addition of para- H_2 [10].

Another technique is SEOP, which results in highly polarized noble gas nuclei. An alkali-metal, such as Rb, Cs, or K, can have its electronic ground state excited by a circularly polarized laser beam. This process results in polarization transfer from the alkali-metal electrons to the noble gas nuclei by collisions, which is facilitated by the Fermi-contact interaction. This technique, which polarizes electron spins using light, was initially shown by Kastler [20]. Later, Bouchiat [26] and then Grover [27] exploited spin-exchange with optically pumped alkali-metal vapors to show that noble gas nuclei are polarized. The SEOP method has been improved by researchers including Happer, Cates, and Walker [12, 28, 29, 30, 31]. In addition to polarizing the nuclear spin of noble gas nuclei like ^{21}Ne , ^{83}Kr , and ^{131}Xe , SEOP is frequently employed to polarize the nuclear spin of ^{129}Xe and ^3He . The field of hyperpolarized noble gases, particularly ^{129}Xe , has seen significant progress with the emergence of MRI for human subjects utilizing hyperpolarized noble gases. The choice of alkali-metal in spin-exchange optical pumping (SEOP) plays a crucial role in this process. Our collaborators at Polerean, a medical imaging company, use hyperpolarized ^{129}Xe to do medical imaging of human lungs, they produce the hyperpolarized ^{129}Xe using the SEOP method with Rb, and they are interested in knowing which alkali-metal is

a better partner for polarizing ^{129}Xe . While Rb has been traditionally favored due to the availability of inexpensive high-power diode lasers [11], recent studies suggest Cs might offer practical advantages with a higher spin-exchange cross-section, higher vapor pressure than Rb at a given temperature, and faster optical pumping rate. The goal is to compare the SEOP efficiency for Xe-Rb and Xe-Cs systems.

$$\eta_{\text{se}} = \frac{\gamma_{\text{se}}/[A]}{\Gamma_{\text{A}}^{(\text{Xe})}/[\text{Xe}]} = \frac{k_{\text{se}}[\text{Xe}]}{\Gamma_{\text{A}}^{(\text{Xe})}} \quad (1.1)$$

where $[A]$ and $[\text{Xe}]$ are the alkali-metal and noble gas Xe number densities, γ_{se} is the alkali-metal-noble gas spin-exchange rate due to collisions with Xe, $\Gamma_{\text{A}}^{(\text{Xe})}$ is the alkali-metal electron-randomization rate due to collisions with Xe, and k_{se} is the alkali-metal-noble gas spin-exchange rate coefficient.

This study focuses on comparing the SEOP efficiency of Xe-Rb and Xe-Cs systems in different pressure regimes and fixed gas mixtures of $^4\text{He}(94\%)\text{-N}_2(3\%)\text{-Xe}(3\%)$, which is similar to the ones used in magnetic resonance imaging polarizers. The spin-exchange efficiency η_{se} is determined by factors such as alkali-metal-noble gas spin-exchange rate γ_{se} , alkali-metal electron-randomization rate Γ_{A} , and alkali-metal-noble gas spin-exchange rate coefficient k_{se} . Despite the widespread use of high-pressure He in SEOP experiments, there's a notable lack of comprehensive studies on spin-relaxation and spin-exchange rates, especially in the Xe-Cs system.

This research delves into the ‘short’ and ‘very short’ lifetime regimes, where bi-

nary collisions primarily contribute to the alkali-metal spin-destruction. Molecular contributions are considered, emphasizing the dependence on gas density. Theoretical insights are provided in the following chapters to create a framework for understanding the alkali-metal spin-relaxation and alkali-metal-noble gas spin-exchange phenomena.

In summary, this research aims to contribute to the understanding of alkali-metal-noble gas interactions, measuring the needed parameters, the alkali-metal-noble gas spin-exchange rate coefficient, and the alkali-metal electron-randomization rate in order to calculate the alkali-metal-noble gas spin-exchange efficiency using reliable methods such as ‘relaxation in the dark’ and ‘repolarization’, providing insights into the optimal choice of alkali-metal for hyperpolarized ^{129}Xe production.

The literature contains numerous comprehensive listings and detailed descriptions of hyperpolarization and dynamic nuclear polarization, which readers can consult for further information [10, 11, 32, 33]. In this research, the nuclear polarization of the samples was raised through the utilization of SEOP.

1.4 Structure of this Thesis

Chapter 2 outlines a brief theoretical background of SEOP, including the alkali-metal hyperfine structure, the optical pumping process and its different methods, the alkali-metal electron magnetic resonance, the basics behind the EPR spectroscopy, and then moves on to different mechanisms happening in an SEOP process such as the spin-exchanged between the alkali-metal and noble gas and the alkali-metal

electron spin polarization relaxation.

Chapter 3 contains the details of our experiment, general apparatus, cell making, a description of different pieces of our experimental setup for relaxation in the dark, and frequency shift measurements, such as pump and probe lasers, magnetic fields, and the electronics used in the setup.

Chapter 4 is a detailed description of our relaxation in the dark experiment for measuring the alkali-metal spin-relaxation rate γ_A and calculating the alkali-metal electron-randomization rate Γ_A for the final purpose of measuring the SEOP efficiency η_{se} , we give an overview of the theory of our work, the experimental setup and procedure. We measured Γ_{Xe-Rb} to be about 30% smaller than that of Xe-Cs system ($\Gamma_{Rb} = 0.7\Gamma_{Cs}$) (table. 1.1) and compared our results with Nelson and Walker’s theoretical model [34] and showed that our results are compatible with their theoretical model.

Cell	$\gamma_A(1/s)$	$\Gamma_A(1/s)$
309A (Rb)	1170±80	12636±864
309B (Rb)	1504±86	16243±928
309C (Rb)	1657±105	17895±1134
309D (Rb)	1865±200	20142±2160
310A (Cs)	678±45	14916±990
310B (Cs)	899±35	19778±704
310C (Cs)	1131±42	24882±924
310D (Cs)	1238±68	27236±1496

Table 1.1: Values of measured spin-destruction rate γ_A and electron-randomization rate Γ_A for Xe-Rb and Xe-Cs systems.

Chapter 5 represents our experimental work on measuring the spin-exchange rate

coefficient k_{se} , which is another piece for calculating the SEOP efficiency η_{se} . First, we briefly review the theory and then move on to the experimental setup and procedure. In the end, we report our measured values for k_{se} for both Xe-Rb and Xe-Cs systems as well as the calculated η_{se} for the systems. We got that Cs has $\sim 35\%$ higher spin-exchange rate coefficient than Rb, pairing these results (table. 1.2) with the electron-randomization results (table. 1.1), we get that Cs has slightly better SEOP efficiency (table. 1.2), besides these results, Cs has other advantages compared to Rb, such as having a higher vapor density than Rb at a given temperature, and more photons per watt of D₁ laser. These can suggest that Cs may be a better partner for polarizing Xe.

Cell	$k_{se} \times 10^{-16}$ (cm ³ /s)	η_{se}
309A (Rb)	7.52±0.34	0.0604±0.0035
309C (Rb)	4.47±0.20	0.0475±0.0024
309D (Rb)	4.43±0.20	0.0471±0.0023
310A (Cs)	12.23±0.96	0.0789±0.0067
310B (Cs)	8.87±0.40	0.0687±0.0034
310C (Cs)	7.33±0.52	0.0567±0.0041
310D (Cs)	6.93±0.27	0.0591±0.0024

Table 1.2: Calculated values of spin-exchange rate coefficient k_{se} and SEOP efficiency η_{se} for Xe-Rb and Xe-Cs systems.

Chapter 6 is the conclusion, where we summarize our work and overview our results.

CHAPTER 2

GENERAL THEORY OF SEOP

In general, spin-exchange optical pumping has two steps in which the polarization of the alkali-metal atom is transferred to the noble gas nuclei through binary collisions or molecular formation after it has been optically polarized using a resonant circularly polarized light. A fairly thorough description of the SEOP procedure can be found in the Refs. [35, 29]. Only the highlights will be briefly explained in this chapter.

2.1 The Hyperfine Structure of Alkali-Metal Atoms

Schrödinger's wave equation $i\hbar(\partial\Psi/\partial t) = \hat{H}\Psi$ [36] is used in quantum mechanics to describe the evolution of a physical state over time. The equation involves the Hamiltonian \hat{H} , which combines the system's kinetic energy \hat{T} and potential energy \hat{V} , \hbar , which is the Planck's constant divided by 2π , and the wave function Ψ that represents the system's state. One can write the equation in terms of density matrix ρ to provide a more convenient representation. This alternative form is called the Liouville - Neumann equation, expressed as [37]:

$$i\hbar\frac{\partial\rho}{\partial t} = [\rho, \hat{H}] \quad (2.1)$$

in Eq. 2.1, $[\rho, H]$ represents a commutator [38]. based on Dirac's 'bra-ket' notation in each basis $|\phi_m\rangle$, one can write the density matrix (ρ) as [37]

$$\rho_{mn} = \langle \phi_m | \rho | \phi_n \rangle = \sum_i p_i \langle \phi_m | \psi_i \rangle \langle \psi_i | \phi_n \rangle \quad (2.2)$$

where p_i denotes the probability of the system being in the state $|\psi_i\rangle$. Quantum states are completely described by the density operator ρ , including the particle's intrinsic angular momentum or 'spin,' which adds an extra degree of freedom beyond the three generalized coordinates typically used to describe classical physical systems. Meanwhile, the degrees of freedom for motion are either constrained or represented by different relaxation rates. The gyromagnetic ratio γ , controls the magnetic moment $\boldsymbol{\mu}$, which is linked to the spin [36]. The electron spin direction is indicated by the spin operator \mathbf{S} , and the magnetic moment can be expressed as $\boldsymbol{\mu}_S = \gamma \mathbf{S}$ (or $\boldsymbol{\mu}_S = g_S \mu_B \mathbf{S} / \hbar$), where μ_B is the Bohr magneton. All spin states have the same energy without a magnetic field or coupling. However, based on the Zeeman effect, a magnetic field can lift this degeneracy along the magnetic field direction. This effect can be represented by the coupling component $-\boldsymbol{\mu}_S \cdot \mathbf{B}$ in the spin Hamiltonian, where \mathbf{B} stands for an external magnetic field [36].

One can solve the radial Schrödinger's equation in the presence of Coulomb potential and get the energy levels of the Hydrogen atom. Three quantum numbers n, l, m describe the spatial part of the hydrogen atom wave function, n is the princi-

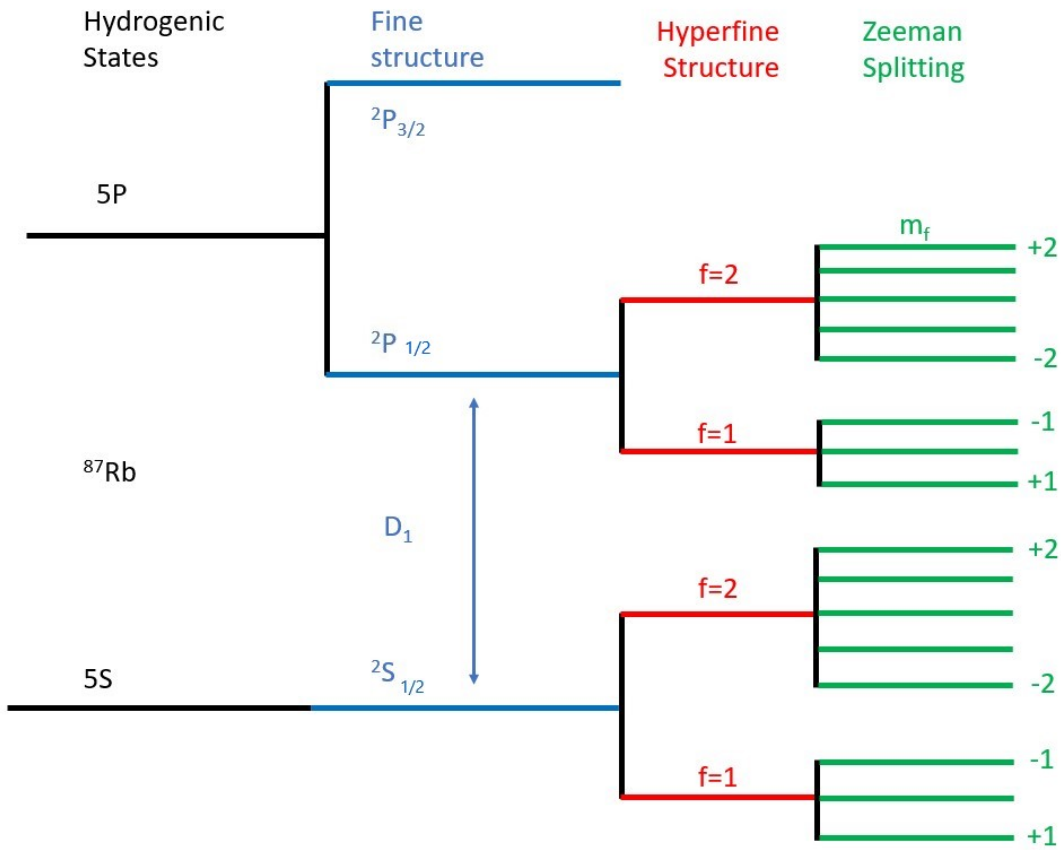


Figure 2.1: Diagram of ^{87}Rb in an external magnetic field, showing the Zeeman effect and hyperfine sublevels.

pal quantum number and represents the atom's total energy, $l = 0, 1, \dots, n - 1$ is the angular momentum quantum number showing the magnitude of the orbital angular momentum, and $m = -l, \dots, l$ is the projection of l into a specific axis, known as the magnetic quantum number. Along those quantum numbers, $I, S, m_I,$ and m_s are quantum numbers presenting the nuclear and electron spins and their projections, respectively [36].

When placed in a weak magnetic field, the good quantum number for a Hydrogen-like atom with no nuclear spin is m_J , the projection of the total electron angular momentum $J = S + L$ into a particular axis. J, L, S , and I , are the total angular momentum, orbital angular momentum, electron spin, and nuclear spin angular momenta operators, respectively. For each angular momentum of the system, there exists an associated magnetic moment ($\boldsymbol{\mu}_J = g_J \mu_B \mathbf{J} / \hbar = \gamma_J \mathbf{J}$, $\boldsymbol{\mu}_I = g_I \mu_N \mathbf{I} / \hbar = \gamma_I \mathbf{I}$), where μ_N is a nuclear magneton [36]. The atom's total angular momentum is $F = I + S$ and $\boldsymbol{\mu}_F = g_F \mu_B \mathbf{F} / \hbar$. The outcome of the magnetic field and angular momentum coupling is a Zeeman interaction, which exists for each angular momentum ($-\boldsymbol{\mu} \cdot \mathbf{B}$). Alkali-metal atoms like Rb and Cs are hydrogen-like atoms due to their single valance electron. The core electrons only cause a screening of the nuclear charge and lead to an effective spherically symmetric coulomb potential. Fig. 2.1 shows, as an example, the gross, the fine, and the hyperfine Hydrogen-like structure of ^{87}Rb energy levels. The diagram also shows the Zeeman splitting in the presence of a weak magnetic field, a situation commonly encountered in optical pumping experiments.

The total Hamiltonian describing an alkali-metal atom in an external magnetic field \mathbf{B} is given by [12]

$$H = H_0 + A_{\text{Spin-Orbit}} \mathbf{L} \cdot \mathbf{S} + A_{\text{Hyperfine}} \mathbf{I} \cdot \mathbf{J} - \boldsymbol{\mu}_J \cdot \mathbf{B} - \boldsymbol{\mu}_I \cdot \mathbf{B} \quad (2.3)$$

where H_0 is the Hamiltonian describing the kinetic energy and the effective Coulomb

potential energy of the single valence electron (i.e., all the terms that don't involve spin), $A_{\text{Spin-Orbit}}\mathbf{L}\cdot\mathbf{S}$ is the spin-orbit interaction between the orbital angular momentum \mathbf{L} and the spin angular momentum \mathbf{S} of the electron, $A_{\text{Hyperfine}}\mathbf{I}\cdot\mathbf{J}$ is the hyperfine interaction between the electron total angular momentum \mathbf{J} and the nuclear spin \mathbf{I} , and the last two terms are the electron and nuclear Zeeman interactions, respectively. The ground state spin Hamiltonian is given by [12]

$$H_g = A\mathbf{I}\cdot\mathbf{S} - \boldsymbol{\mu}_s\cdot\mathbf{B} - \boldsymbol{\mu}_I\cdot\mathbf{B} \quad (2.4)$$

where we omitted the constant H_0 and the vanishing spin-orbit term ($L=0$). This Hamiltonian has the virtue that it can be diagonalized, and the corresponding energy levels can be found analytically. G. Breit and I. I. Rabi [39] diagonalized this Hamiltonian for an arbitrary nuclear spin I and found the ground state eigenenergies as a function of the magnetic field [40]

$$\frac{E}{h} = -\frac{\nu_{\text{HF}}}{2(2I+1)} \pm \frac{\nu_{\text{HF}}}{2} \left(1 + \frac{2m_F}{I+1/2} \left(\frac{g_s\mu_B}{h\nu_{\text{HF}}}\mathbf{B} \right) + \left(\frac{g_s\mu_B}{h\nu_{\text{HF}}}\mathbf{B} \right)^2 \right)^{1/2} \quad (2.5)$$

where ν_{HF} is the hyperfine splitting for $B = 0$. Fig. 2.2 is a plot of Eq.2.5 as a function of the field for ^{87}Rb . In Eq. 2.5 the effect of nuclear Zeeman energy ($\boldsymbol{\mu}_I\cdot\mathbf{B}$) has been ignored, which is a valid assumption, since at high enough magnetic fields (~ 28 G in our case) the quadratic electron term dominates the linear nuclear term

resulting in $g_s + g_I \rightarrow g_s$.

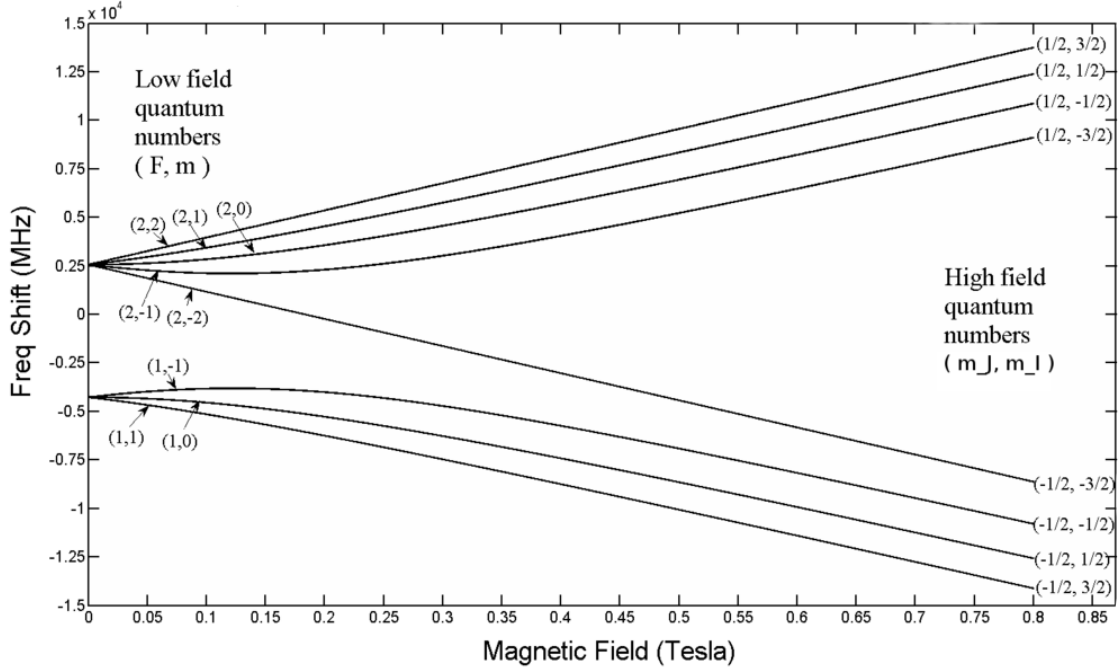


Figure 2.2: ^{87}Rb ground state hyperfine energy levels vs. the magnetic field. The top manifold is $F = 2$, and the bottom manifold is $F = 1$. The lines show the hyperfine states, where they are labeled as F and m_F for small fields and m_J and m_I for large fields. At low fields, the energies are linear. As we move toward higher fields, the energy levels become nonlinear with the field [40].

The size of the hyperfine coupling and the magnetic field strength define the good quantum numbers that properly describe the states of the system. In the weak-field regime (up to ~ 1 kG for ^{87}Rb [40]), \mathbf{I} and \mathbf{S} are well coupled, and the good quantum numbers are $F = I + S$, and $m_F = -F, \dots, 0, \dots, +F$ [37]. In this case, the hyperfine states are labeled as $\langle F, m_F \rangle$, and the hyperfine transitions are denoted by $\langle F, m_F \pm 1/2 \rangle = \langle F, m_F \rangle \leftrightarrow \langle F, m_F \pm 1 \rangle$. For example, the transition $\langle 2, 1 \rangle \leftrightarrow \langle 2, 0 \rangle$

is labeled as $\langle 2, 1/2 \rangle$. Those good quantum numbers remain valid until the magnetic field gets strong enough to cause the constituent angular momenta to be coupled to the magnetic field B rather than to each other. Eq. 2.5 is a non-linear relation between the hyperfine sub-level energies and the magnetic field. By applying a large magnetic field, \mathbf{I} and \mathbf{S} get decoupled, and the good quantum numbers become m_I and m_S . In this case, the product states $\langle m_I, m_S \rangle$ serve as a good representation of the system.

2.2 Optical Pumping

Photons can transfer angular momentum to atoms and molecules by resonant scattering. A. Kastler was the first to introduce this concept of optical pumping in 1966 [41]. Optical pumping produces a population imbalance between the spin or the magnetic sub-levels of some gaseous atoms using resonant light with specific polarization. A spin has no preferred direction without a magnetic field and the spin states are said to be degenerate. Applying a magnetic field B_0 lifts the degeneracy. This is called the Zeeman effect (Fig. 2.1). It causes the spin up and spin down states to split by energy $E = \hbar\gamma B_0$, where γ is the gyromagnetic ratio. In contrast to an isolated single spin, an ensemble of spins exchanging energy and interacting with each other have two relevant observables: the longitudinal relaxation and thermal spin polarization of the sample. Boltzmann distribution governs the thermal polarization, and for $S = 1/2$, it is the difference between the two spin states' population normalized

by the total number of spins [40],

$$P = \frac{n_+ - n_-}{n_+ + n_-} = \tanh \frac{\mu B_0}{k_B T} \quad (2.6)$$

where n_+ and n_- are the populations of $S = +1/2$ and $S = -1/2$ states, k_B is the Boltzmann constant and T is the absolute temperature of the sample. The typical thermal polarization at $B_0 = 2$ T and room temperature is about 10^{-5} to 10^{-6} . When spins are directly detected, their density, polarization, and magnetic moment determine the magnetization of the sample, which in turn determines the magnitude of the signal. Considering the case where we have a large ensemble of electron spins that have been optically pumped and acquired the net magnetization under certain conditions, the steady state polarization of alkali-metal atoms is defined by Eq. 2.6, and this polarization is orders of magnitude larger than thermal polarization. For particles with $S \neq \frac{1}{2}$ using the Boltzmann distribution to describe the population distribution through the hyperfine states, polarization can be defined as, $P = \langle S_z \rangle / S$ [40].

Optical pumping experiments can provide spectroscopic information regarding interatomic forces. The basic parts for doing optical pumping are a light source for pumping, a sample to absorb and scatter photons and become spin-polarized, and a detector part to observe the polarization of the sample [42]. There can be different buffer gases in the sample to help the process. For example, an inert buffer gas like

^4He helps with the collisional mixing of the atoms in the excited state and pressure broadening of the alkali-metal absorption lines to prevent light loss, and it also helps to hinder the wall relaxation of polarized atoms. Molecular or buffer gases, like N_2 are used as quenching gases to avoid radiation trapping and help the excited atoms to de-excite irradiatively. There are three different methods of optical pumping [42]:

- Anisotropic excitation.
- repopulation pumping.
- depopulation pumping.

2.2.1 *Anisotropic Excitation*

This method is one of the simplest methods of optical pumping. In this method, linearly polarized light is used such that the axis of quantization is the same as the light polarization direction and the applied magnetic field. The purpose of the applied field is to protect spins from the ambient fields that are not in the direction of the quantization axis [42]. As shown in Fig. 2.3, the atoms in the ground state $J = 0$ get excited to the sub-level $m = 0$ of the excited state $J = 1$. Since magnetic sub-levels are not populated equally, spin polarization is created in the excited state. A way of detecting the spin polarization in this method is by detecting the dipole radiation pattern of fluorescent light [42]. High polarization can be achieved using this method, but the problem is that the atoms in the excited state are unstable and quickly decay.

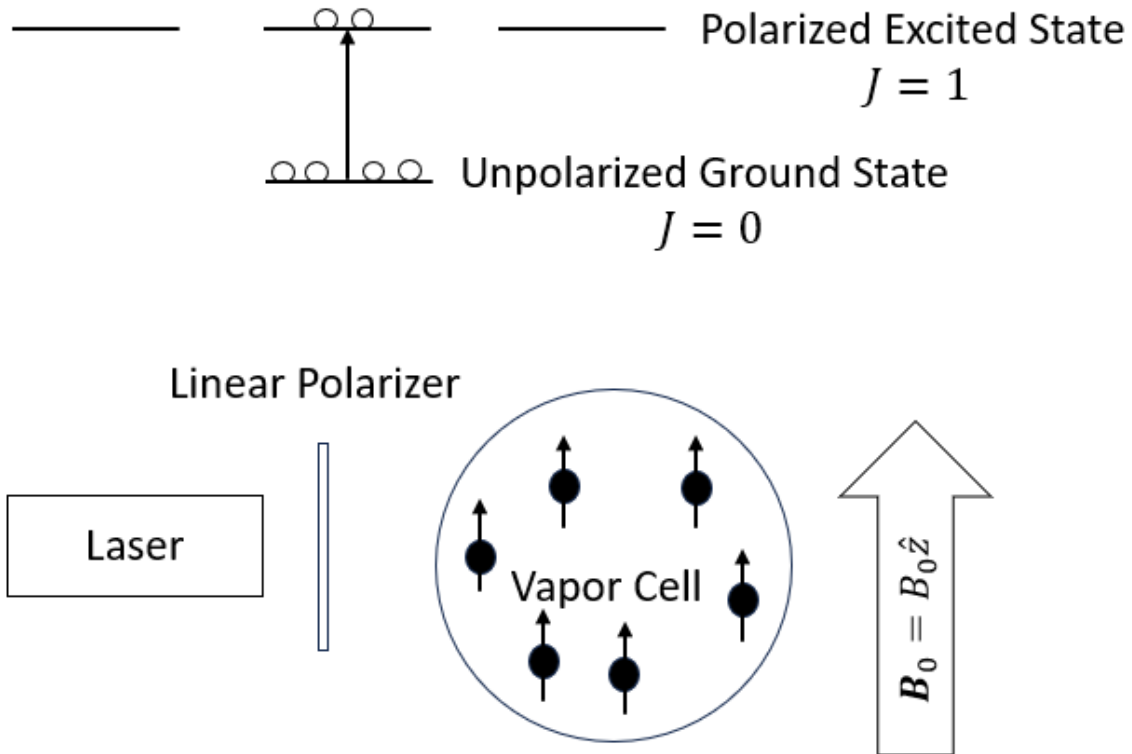


Figure 2.3: Schematics of anisotropic optical excitation, in this method, the $m = 0$ sublevel of the excited states gets populated using a laser. The pump light polarization direction defines the quantization axis [42].

2.2.2 Repopulation Pumping

In this method, the polarization of the excited state gets transferred to a lower state due to the unequal branching ratios of the lower sub-levels. The spin-polarized atoms in the excited state spontaneously decay and unevenly populate the sub-levels of the lower state following the relevant selection rules. In this method, the excited state collisional mixing should be avoided to prevent the loss of polarization before

the spontaneous emission takes place. Therefore, this method is more practical when there is a low pressure of buffer gas and collisions between the excited atoms are minimized [42].

2.2.3 Depopulation Pumping

The third method of optical pumping that we use in our experiments is depopulation pumping. With this method, one can generate a large number of spin-polarized atoms in the ground state. In this method, because of the specific selection rules being imposed on the system, one or more particular sub-levels of the ground state atoms get excited by light; hence, the population of those states decreases (gets depopulated), and the ground state eventually becomes spin polarized. The optical pumping process can be understood by considering the simple case of a hypothetical alkali-metal atom that has no nuclear spin, $I = 0$ (Fig. 2.4). The alkali-metal atoms are excited from $m_j = +1/2$ states by D_1 , right circularly polarized light σ^- , inducing selection rule $\Delta m = -1$ to the possible transition. The excited state population reaches equilibrium by collisional mixing of the alkali-metal atoms with each other and with a coexisting buffer gas. The buffer gas also acts as a quenching gas and the excited atoms undergo a nonradiative decay resulting in population accumulation in the sub-level $m_j = -1/2$ of the ground state [12]. If the excited atoms decay radiatively, the emitted unpolarized photon can get trapped and scattered several times and cause alkali-metal atoms to undergo transitions without obeying the $\Delta m = \pm 1$

selection rule. Hence the population imbalance will be ruined. Therefore, molecular buffer gases like N_2 are used to help prevent the so-called radiation trapping [42].

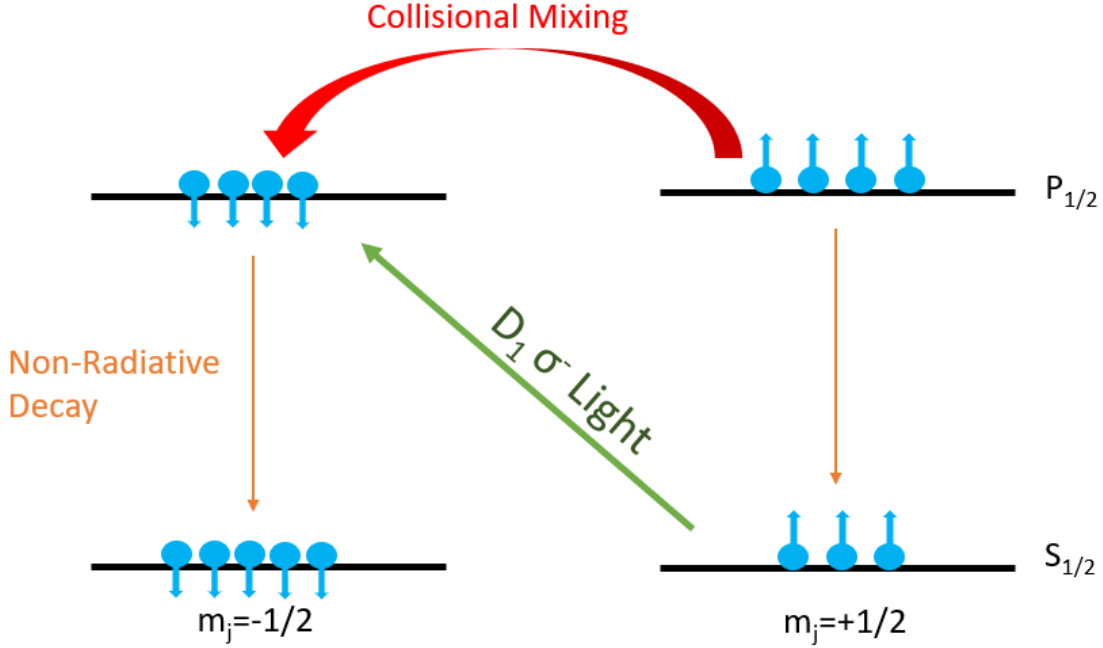


Figure 2.4: Depopulation optical pumping of the alkali-metal atom with the assumption there is no nuclear spin. The alkali-metal atoms are optically pumped from $(m_j = +\frac{1}{2})$ states by D_1 , left circularly polarized light (σ^-), inducing selection rule $\Delta m = -1$ to the possible transition. The excited state population reaches equilibrium by collisional mixing of alkali-metal atoms with each other and with buffer gases, and then N_2 acts as quenching gas to help the excited atoms to have a nonradiative decay resulting in population accumulation in one sub-level of the ground state ($m_j = -\frac{1}{2}$).

In reality, the nuclear spin \mathbf{I} and its hyperfine interaction $\mathbf{I} \cdot \mathbf{S}$ with the electron spin is nonzero for the alkali-metal atoms. Hence, the ground and excited states are divided into hyperfine sub-levels. In addition, the presence of an external magnetic

field produces Zeeman splitting of those hyperfine sub-levels, see Fig. 2.1. In our experiments, we use Rb and Cs as the alkali-metals of interest. Circularly polarized light with a specific helicity (σ^+ or σ^-) tuned to the D_1 transition of the alkali-metal atoms irradiates a vapor cell of alkali-metal and excites the valance electron of the ground state $5S_{1/2}$ in the case of Rb and $6S_{1/2}$ in the case of Cs, to the first excited state $5P_{1/2}$ and $6P_{1/2}$, respectively. The specific helicity of light adds an extra selection rule $\Delta m = \pm 1$ to the possible transitions. As an example, Fig. 2.5 shows the full picture of ^{87}Rb optical pumping in the presence of a weak external magnetic field. The thin arrows show the allowed transition based on the selection rule $\Delta m = -1$, and the bold arrows show the decay of atoms to the ground state sub-levels. By choosing the σ^- light, this optical pumping results in populating the $|2, -2\rangle$ sub-level because it is the only sub-level for which there is no allowed transition to the excited states [12].

For these metals D_1 ($5S_{1/2} \rightarrow 5P_{1/2}$ and $6S_{1/2} \rightarrow 6P_{1/2}$) and D_2 ($5S_{1/2} \rightarrow 5P_{3/2}$ and $6S_{1/2} \rightarrow 6P_{3/2}$) hyperfine transitions are far enough apart that when we use D_1 light for optical pumping, the D_2 transition is considered negligible due to low optical pumping power. D_1 light is more favorable for optical pumping than D_2 light for a couple of reasons, such as with the D_2 light, no matter what helicity of light is used, the atoms from all sub-levels of the ground state can be pumped to the excited states, and the high-power diode laser, for D_1 light is more affordable [40]. Although optical

pumping can be carried out in the absence of a magnetic field and the direction of the pump laser will be determined as the quantization axis, as previously said, any variation in the magnetic field within the sample would sabotage the spins and disrupt the intended population build-up. To avoid this, we use an external static magnetic field $\simeq 28$ G aligned with the direction of pump light to dominate any ambient fields in the surroundings.

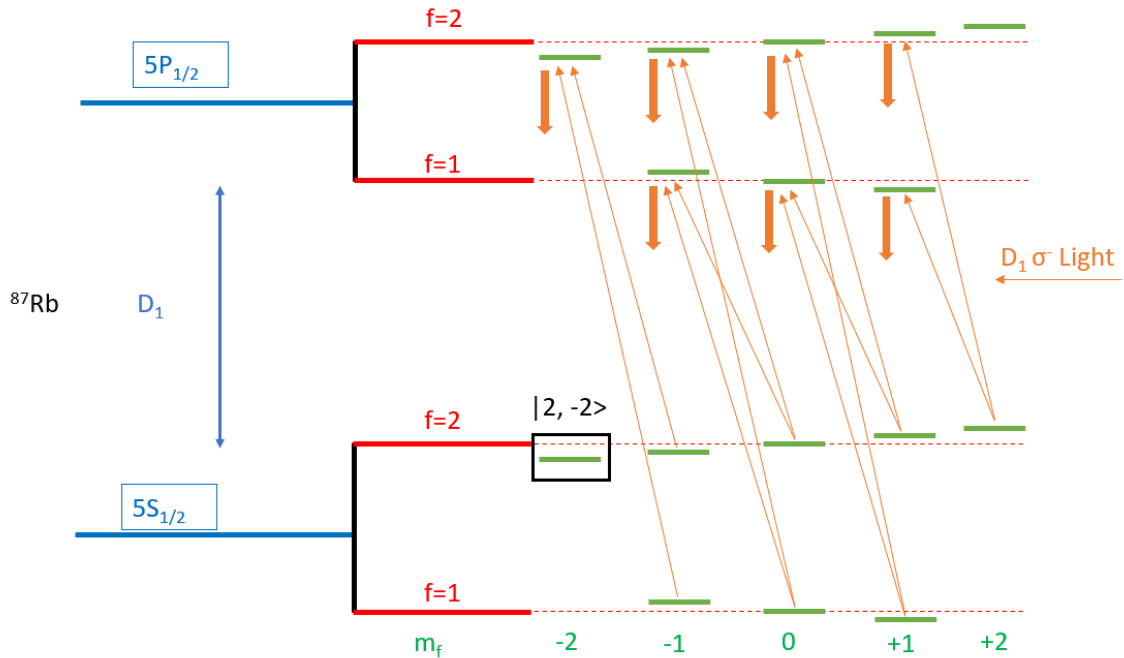


Figure 2.5: Optical pumping of ^{87}Rb with left circularly polarized light while it is placed in an external magnetic field ($B_0 = 28$ G). The thin arrows show the allowed transition based on the selection rule $\Delta m = -1$, and the bold arrows show the decay of atoms to the ground state sub-levels. This optical pumping results in populating the $|2, -2\rangle$ sub-level because it is the only sub-level for which there is no allowed transition to the excited states.

In the simplified picture of Fig. 2.4, the rate equations that govern the population transfer between the $m_j = -1/2$ and $m_j = +1/2$ ground states are given by

$$\begin{aligned}\frac{dn_+}{dt} &= -(2R)n_+ + \frac{1}{2}(2R)n_+ = -\frac{1}{2}(2R)n_+ \\ \frac{dn_-}{dt} &= \frac{1}{2}(2R)n_+\end{aligned}\tag{2.7}$$

where n_+ and n_- denote the number of atoms in the sub-levels $m_j = +1/2$ and $m_j = -1/2$, respectively. R is the optical pumping rate, and it is given by

$$R = \int_0^\infty \frac{I(\nu)\sigma(\nu)}{h\nu} d\nu\tag{2.8}$$

here $I(\nu)$ is the spectral intensity of incident light, and $\sigma(\nu)$ is the cross section for the scattering of light by unpolarized atoms [43]. Eq. 2.7 and 2.8 can be written in terms of the sum $N = n_- + n_+$ and difference $n = n_- - n_+$ of the sub-level populations

$$\begin{aligned}\frac{dN}{dt} &= 0 \quad \rightarrow \text{(It is the result of the conservation of number of atoms)} \\ \frac{dn}{dt} &= (2R)n_+ = (2R)\left(\frac{N-n}{2}\right) = \frac{(2R)}{2}N - \frac{(2R)}{2}n\end{aligned}\tag{2.9}$$

with the solution $n(t) = N\left(1 - e^{-(2R)\frac{t}{2}}\right)$, where $n(t=0) = 0$. The alkali-metal polarization $P = \frac{n}{N}$ evolution is governed by

$$\frac{dP}{dt} = \frac{(2R)}{2}(1 - P)\tag{2.10}$$

with the solution $P(t) = 1 - e^{-(2R)\frac{t}{2}}$. Eq. 2.10 shows that the alkali-metal polarization can reach 100% regardless of the pumping rate R . In reality, the rate equations should include the relaxation terms that account for the alkali-metal relaxation processes and lead to a more realistic steady-state polarization

$$\begin{aligned}\frac{dn_+}{dt} &= -\frac{(2R)}{2}n_+ - \Gamma n_+ \\ \frac{dn_-}{dt} &= +\frac{(2R)}{2}n_+ - \Gamma n_-\end{aligned}\tag{2.11}$$

where Γ is the alkali-metal polarization relaxation rate. Taking the difference between these two equations, we get

$$\begin{aligned}\frac{dn}{dt} &= (2R)n_+ - \Gamma(n_- - n_+) = (2R)\left(\frac{N-n}{2}\right) - \Gamma n \\ &= \frac{(2R)}{2}N - \left(\frac{(2R)}{2} + \Gamma\right)n\end{aligned}\tag{2.12}$$

The suggested solution for Eq. 2.12 can be

$$n(t) = \frac{\frac{(2R)}{2}}{\frac{(2R)}{2} + \Gamma} N \left(1 - e^{-\left(\frac{(2R)}{2} + \Gamma\right)t}\right)\tag{2.13}$$

In the case of alkali-metal polarization, considering the polarization relaxation term, the polarization time evolution will be

$$\frac{dP}{dt} = \frac{(2R)}{2}(1 - P) - \Gamma P\tag{2.14}$$

which has the solution of

$$P(t) = \frac{n(t)}{N} = \frac{\frac{(2R)}{2}}{\frac{(2R)}{2} + \Gamma} \left(1 - e^{-\left(\frac{(2R)}{2} + \Gamma\right)t} \right) \quad (2.15)$$

As one can see from Eq. 2.15, the steady state polarization when we wait long enough is

$$P(\infty) = \frac{\frac{(2R)}{2}}{\frac{(2R)}{2} + \Gamma} < 1 \quad (2.16)$$

The optical pumping rate should be large compared to the alkali-metal atoms' spin-relaxation rate to have high alkali-metal polarization.

2.3 Magnetic Resonance

Alkali-metal polarization can be measured using transverse electron paramagnetic resonance (EPR) technique [44, 45]. In this method, an alternating (RF) magnetic field \mathbf{B}_1 perpendicular to the main field \mathbf{B}_0 is applied to nutate the spins into the transverse plane where they can be detected by Faraday rotation measurements. The mathematical formalisms are described thoroughly in [46]. A simplified version will be discussed here. This alternating magnetic field will manipulate the alkali-metal spins. Viewing the process from the rotating frame is helpful. If one transfers the vector \mathbf{A} from its inertial frame to a rotating frame which rotates with frequency ω ,

then vector \mathbf{A} can be written as

$$\left(\frac{d\mathbf{A}}{dt}\right)_{\text{Inertial}} = \left(\frac{d\mathbf{A}}{dt}\right)_{\text{Rotating}} + \boldsymbol{\omega} \times \mathbf{A} \quad (2.17)$$

$$\left(\frac{d\mathbf{A}}{dt}\right)_{\text{Rotating}} = \left(\frac{d\mathbf{A}}{dt}\right)_{\text{Inertial}} - \boldsymbol{\omega} \times \mathbf{A} \quad (2.18)$$

Now considering a spin \mathbf{S} in the magnetic field \mathbf{B}_0 as the vector of interest in the lab frame, it undergoes a Larmor precession [46]

$$\left(\frac{d\mathbf{S}}{dt}\right)_{\text{Inertial}} = \gamma \mathbf{S} \times \mathbf{B}_0 \quad (2.19)$$

In the rotating frame, we get

$$\left(\frac{d\mathbf{S}}{dt}\right)_{\text{Rotating}} = \gamma \mathbf{S} \times \mathbf{B}_0 - \boldsymbol{\omega} \times \mathbf{S} = \gamma \mathbf{S} \times \left(\mathbf{B}_0 + \frac{\boldsymbol{\omega}}{\gamma}\right) \quad (2.20)$$

in this frame, the system experiences an effective magnetic field, defined as [46]

$$\mathbf{B}_{\text{eff}} = \mathbf{B}_0 + \frac{\boldsymbol{\omega}}{\gamma} \quad (2.21)$$

and spins start to precess around that. Now, if we apply an oscillating magnetic field,

which can be separated into counter-rotating components [46]

$$\mathbf{B}_{1R} = B (\cos \omega t \hat{x} + \sin \omega t \hat{y}) \quad (2.22)$$

$$\mathbf{B}_{1L} = B (\cos \omega t \hat{x} - \sin \omega t \hat{y}) \quad (2.23)$$

and consider the rotating frame to rotate synchronously with one of the components, for example, \mathbf{B}_{1R} , in this case, \mathbf{B}_{1R} becomes stationary in the rotating frame, and \mathbf{B}_{1L} rotates with angular velocity 2ω which is far enough from resonance that can be neglected. Since we chose the axis of rotation to be the same as the axis of \mathbf{B}_0 , it is also stationary in the rotating frame, so \mathbf{B}_{eff} will be [46]

$$\mathbf{B}_{\text{eff}} = B_0 \hat{z} + B_1 \hat{x} + \frac{\omega}{\gamma} \hat{z} \quad (2.24)$$

Now if we set the frequency of the oscillating field and rotating frame to be the Larmor frequency $\omega_L = -\gamma B_0/2\pi$, then $\mathbf{B}_{\text{eff}} = B_1 \hat{x}$. This means spins experience a static field transverse to \mathbf{B}_0 , and this field exerts a torque on spins, which causes them to nutate about \mathbf{B}_1 with angular velocity $\omega_1 = -\gamma B_1$, which is called the Rabi frequency, and then they will start to precess about \mathbf{B}_0 at Larmor frequency Fig. (2.6).

In the case where $\omega \neq \omega_L$, then the effect of \mathbf{B}_0 on \mathbf{B}_{eff} is not fully canceled,

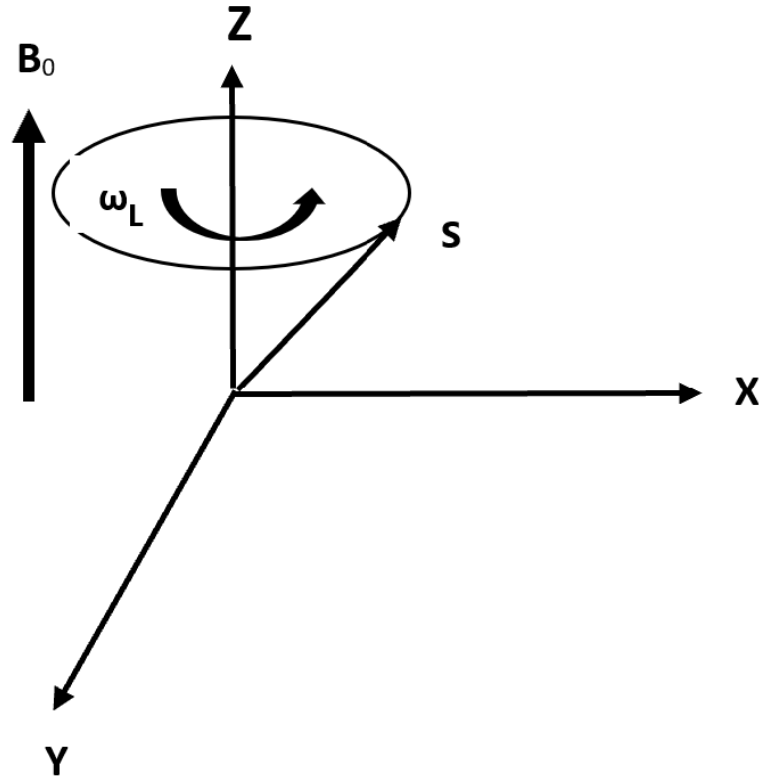


Figure 2.6: Precession of spins about the magnetic field at Larmor frequency.

causing the atoms to experience the static magnetic field $B_1 \hat{x}$ as well as $\frac{\omega - \omega_L}{\gamma} \hat{z}$, then the spins now precess about the effective field in the rotating frame (Fig. 2.7) [46].

If the frequency sweep time of the oscillating field is slow enough, the spins have time to follow the change in the field and precess about the effective field, but this frequency sweep cannot be arbitrarily slow; otherwise, the spins lose their polarization due to dephasing. Regardless of the processes and mechanisms that drive the relaxation, it can be divided into spin-spin and spin-lattice relaxations, which are characterized by time constants T_2 and T_1 , respectively. The spin-lattice or longi-

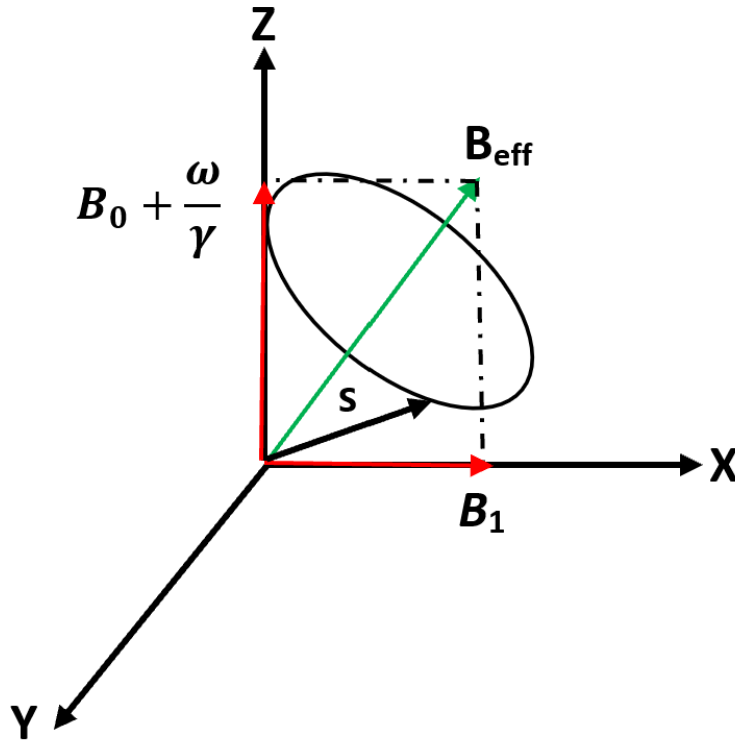


Figure 2.7: Motion of spins in the rotating frame about B_{eff} .

tudinal relaxation T_1 describes how fast the longitudinal magnetization will return to its equilibrium value, and it involves an energy and entropy exchange with the environment. The spin-spin or transverse relaxation T_2 describes how quickly the transverse magnetization disappears, and it is due to microscopic interactions, which are irreversible processes in which order is lost, as opposed to spin-lattice relaxation that both energy and order are lost. Hence, the frequency sweep should be faster than T_1 to prevent spins from losing their polarization. The alternating magnetic field B_1 can be applied by two methods:

1. Continuous wave or CW: in this method, the RF producing the time-dependent \mathbf{B}_1 field is applied such that \mathbf{B}_1 is on all the time and weak enough to preserve the steady-state longitudinal magnetization and prevents RF broadening, i.e., $T_1 \ll \frac{1}{(-\gamma B_1)}$. The resonance is created by having B_0 fixed at some value (in our experiment ~ 28 G) and sweeping the RF frequency of \mathbf{B}_1 through the alkali-metal resonance frequency. When The Rf field hits the resonance frequency corresponding to the transition between two ground states hyperfine sub-levels, an oscillating transverse spin at the frequency of the applied RF field is generated, and detected by measuring the polarization rotation of a probe laser beam. The output is the resonance lines which can be shown on an oscilloscope.

2. Pulsed: in this method, the RF producing the time-dependent \mathbf{B}_1 field is turned on for a specific amount of time. The RF frequency is always set equal to the resonance frequency corresponding to the transition between the two hyperfine sub-levels. For instance, a square $\pi/2$ pulse with the alkali-metal resonant frequency and specific duration is usually used to put the spins into the transverse plane suddenly. For this purpose, in contrast to CW, the RF field should be large enough to flip the spins before spin dephasing takes place, i.e., $T_2 \gg \frac{1}{(-\gamma B_1)}$. The transverse magnetization is then monitored by measuring the polarization rotation of a probe laser beam.

2.4 The spin-exchange and spin-destruction Interactions

2.4.1 Collisional Hamiltonian

Besides the collision-free Hamiltonian Eq. 2.4, there is a collisional Hamiltonian that includes two other interactions, the alkali-metal-Xe binary collisions and the alkali-metal-Xe molecular formation. The spin-rotation interaction [13]

$$V_{\text{sr}} = \gamma \mathbf{N} \cdot \mathbf{S} \quad (2.25)$$

shows the coupling between electronic spin \mathbf{S} and the relative angular momentum \mathbf{N} of the colliding pair. The magnetic dipole coupling or the nuclear electron spin-exchange interaction between the noble gas nucleus and the alkali-metal electron is [13]

$$V_{\text{se}} = \alpha \mathbf{K} \cdot \mathbf{S} \quad (2.26)$$

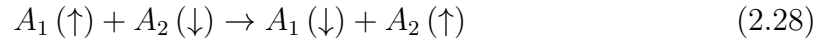
which couples the noble gas nuclear spin \mathbf{K} to the alkali-metal electronic spin. γ and α are the coupling coefficients that depend on R , which is the alkali-metal-buffer gas or noble gas inter-atomic distance, and by increasing R they approach zero. Mixing the collision-free and collisional Hamiltonian provides the final Hamiltonian of the system [13]

$$H = A\mathbf{I} \cdot \mathbf{S} - \boldsymbol{\mu}_I \cdot \mathbf{B} - \boldsymbol{\mu}_s \cdot \mathbf{B} + \gamma(R) \mathbf{N} \cdot \mathbf{S} + \alpha(R) \mathbf{K} \cdot \mathbf{S} \quad (2.27)$$

Interactions like V_{sr} or similar ones that couple electron spin to the orbital angular momentum of the colliding pair result in a huge loss of electron spin polarization. The hyperfine coupling A is also a function of R and rapidly decreases as R increases.

2.4.2 Alkali-Metal-Alkali-Metal Binary Collision

The interaction between pairs of alkali-metal atoms leads to both spin-relaxation of alkali-metal and efficient spin-exchange between the pair [13]



where A_1 and A_2 could be the same isotopes like $A_1 = A_2 = {}^{87}\text{Rb}$ or different isotopes of the same species $A_1 = {}^{87}\text{Rb}$ and $A_2 = {}^{85}\text{Rb}$ or two totally different species like Rb and Cs. The binary spin-exchange between alkali-metal atoms is sudden relative to the nuclear polarization. The spin-exchange rate is

$$\frac{1}{T_{AA}} = [A] \langle \sigma_{AA} V \rangle \quad (2.29)$$

where $[A]$ is the alkali-metal density, V is the relative velocity of the colliding pair and σ_{AA} is the cross-section. This process is considered an S-damping process, which is sudden with respect to hyperfine interaction. During the S-damping process, the alkali-metal electron spin is affected, while the nuclear spin is unaffected. Meaning

the duration of the S-damping process is shorter than the hyperfine period of the alkali-metal ground state [13].

2.4.3 Alkali-Metal-Gas Binary Collision

Collisions between alkali-metal and buffer gases are considered S-damping processes due to their period being much smaller than the hyperfine period. The rate for this process is [13]

$$\frac{1}{T_{\text{sr}}} = [\text{Y}] \langle \sigma_{\text{sr}} V \rangle \quad (2.30)$$

where $[\text{Y}]$ is the buffer gas density and σ_{sr} is the alkali-metal buffer gas, cross-section, and V is the relative velocity. The rate coefficient depends on the temperature [47]. During binary collisions between alkali-metal and noble gas atoms, the alkali-metal loses its electron spin polarization to transfer it to the noble gas nucleus. The binary rate per alkali-metal atom for collisions between alkali noble gas is [13]

$$\frac{1}{T_{\text{se}}} = [\text{Xe}] \langle \sigma_{\text{se}} V \rangle \quad (2.31)$$

2.4.4 Molecular Formation

The van der Waals molecular formation is another process during which electron spin polarization from the alkali-metal is transferred to the noble gas atom. A third

body is needed for the creation and destruction of these molecules [13].



For the formation side, Y_i carries off the binding energy, and it supplies the breakup energy for the breakup side. Molecules are weak enough that any collision can break them apart. The molecular formation rate per alkali-metal atom is

$$\frac{1}{T_{vW}} = \sum_i Z_i [Y_i] [Xe] \quad (2.33)$$

where $[Xe]$ is the number density of Xe, $[Y_i]$ is the number density of the third body, which can be either ^4He , N_2 or Xe depending on the gas mixture, and Z_i is the rate coefficient of the three body process, and the mean molecular lifetime τ is

$$\frac{1}{\tau} = \sum_i [Y_i] \langle \sigma_{vW} V \rangle_i \quad (2.34)$$

κ is called the chemical equilibrium coefficient, and it is defined at temperature T , which is based on Z_i the formation rate coefficient, $\langle \sigma_{vW} V \rangle_i$ the breakup rate coefficient, $1/T_{vW,A}$ the formation rate per alkali-metal atom, $1/T_{vW,Xe}$ the formation

rate per Xe atom and the mean molecular lifetime τ [13]

$$\kappa = \frac{AXe}{[A][Xe]} = \frac{Z_i}{\langle \sigma_{vW} V \rangle_i} = \frac{\tau}{T_{vW,A}[Xe]} = \frac{\tau}{T_{vW,Xe}[A]} \quad (2.35)$$

The interactions $V_{sr} = \gamma \mathbf{N} \cdot \mathbf{S}$ and $V_{se} = \alpha \mathbf{K} \cdot \mathbf{S}$ couple the electron spin \mathbf{S} to the rotational angular momentum \mathbf{N} of the molecules and the nuclear spin \mathbf{K} of the noble gas respectively. The molecular breakup rate is fast, so spins \mathbf{S} and \mathbf{K} will rotate only at a small angle during interactions [13]. These angles are defined as

$$\phi_\alpha = \frac{\alpha\tau}{\hbar} \quad \text{and} \quad \phi_\gamma = \frac{\gamma N\tau}{\hbar} \quad (2.36)$$

Considering the frequencies related to hyperfine $\mathbf{I} \cdot \mathbf{S}$, spin-rotation $\mathbf{N} \cdot \mathbf{S}$ and nuclear electron spin-exchange $\mathbf{K} \cdot \mathbf{S}$ interactions

$$\omega_{HF} = \frac{(2I+1)A}{2\hbar} \quad \text{and} \quad \omega_\alpha = \frac{\alpha}{\hbar} \quad \text{and} \quad \omega_\gamma = \frac{\gamma N}{\hbar} \quad (2.37)$$

one can define different regimes based on frequency, at frequencies lower than the ω_{HF} , both $\Delta F = 0$ and $\Delta F = 1$ transitions happen, which result in a fraction of van der Waals molecules that have short correlation time τ_c and are due to the S-damping interactions [13]

$$f_S = \frac{1}{1 + (\omega_{HF}\tau_c)^2} \quad (2.38)$$

On the other hand, at frequencies that are comparable to or higher than ω_{HF} , τ_c is long enough to allow only $\Delta F = 1$ transitions to happen, resulting in

$$f_{\text{F}} = \frac{(\omega_{\text{HF}}\tau_c)^2}{1 + (\omega_{\text{HF}}\tau_c)^2} \quad (2.39)$$

which is a fraction of van der Waals molecules that is due to F-damping interactions that their period is comparable to or longer than the hyperfine period. Another interpretation of the F-damping and S-damping interactions is that f_{F} is the fraction of molecules with a ‘short lifetime’, and f_{S} is the fraction of molecules with a ‘very short lifetime’ [13]. During spin-exchange collisions, the colliding pair’s spin angular momentum is conserved and distributed between the ground state sub-levels. Since the spin-exchange collisions are sudden with respect to hyperfine interaction during spin-exchange collision, the nucleus of the alkali-metal atom will not get involved and will stay still, but between the collisions, the hyperfine interaction distributes the angular momentum between the nuclear and electron spins of the alkali-metal atom. This process leads to spin-temperature distribution [48]. In the spin-temperature distribution, the density matrix is

$$\rho = \frac{e^{\beta F_z}}{Z} = \frac{e^{\beta I_z} e^{\beta S_z}}{Z_I Z_S} \quad (2.40)$$

where Z the spin partition function and for a spin of an integer or half-integer quantum

number J is [45]

$$Z_J = \sum_{m=-J}^J e^{\beta m} = \frac{\sinh \beta (2J + 1) / 2}{\sinh \beta / 2} = \frac{(1 + P)^{(2J+1)} - (1 - P)^{(2J+1)}}{2P (1 - P^2)^J} \quad (2.41)$$

and β is the spin-temperature parameter, which determines the spin sub-level population distribution [45]

$$\langle S_z \rangle = \frac{\epsilon(S, \beta)}{2} \tanh \frac{\beta}{2} \quad (2.42)$$

where $\epsilon(S, \beta) = 2\langle S(S + 1) - S_z^2 \rangle$ is called the paramagnetic coefficient. The extreme cases of ϵ are $\epsilon = 4S(S + 1)/3$ at small polarization $\beta \ll 1$ and $\epsilon = 2S$ for large polarization $\beta \gg 1$, and in the case of $S = 1/2$, $\epsilon(1/2, \beta) = 1$.

CHAPTER 3

GENERAL APPARATUS

To measure the spin-destruction rate and spin-exchange rate coefficient of an alkali-metal atom, we utilize the relaxation in the dark measurement [49]. Fig. 3.1 and Fig. 3.2 show the schematics of our experimental apparatus.

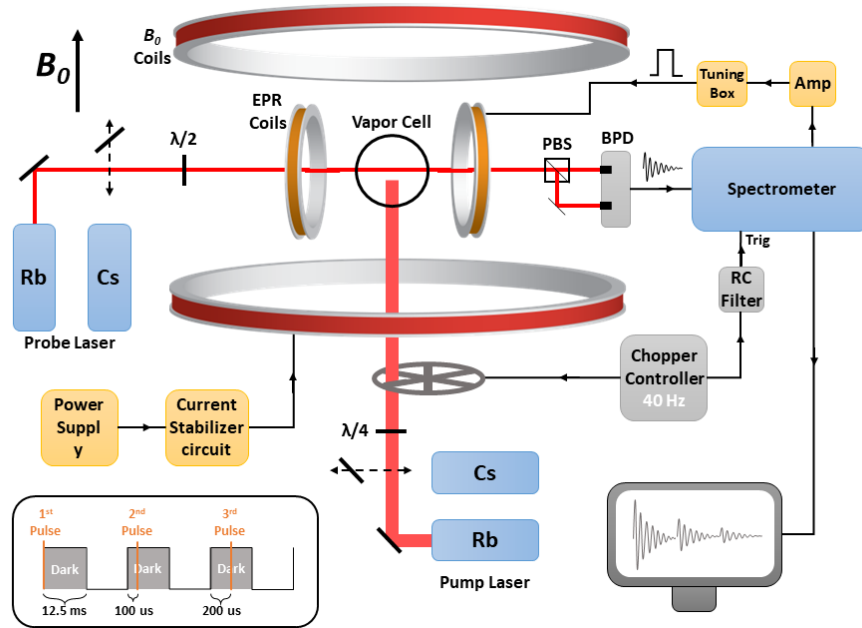


Figure 3.1: spin-destruction rate measurement setup: The polarizing beam splitter and balanced photodetectors are labeled PBS and BPD, respectively. Switching between Rb and Cs lasers was achieved using a sliding mirror in front of the Cs laser. The symbols labeling the wire going to the EPR coils and the wire fed into the spectrometer represent the generated pulses and collected free induction decays FIDs. The inset at the lower left corner shows the timeline of the pulse sequence and the periodic light blocking (dark).

The experiments that we perform to do our measurements consist of five main

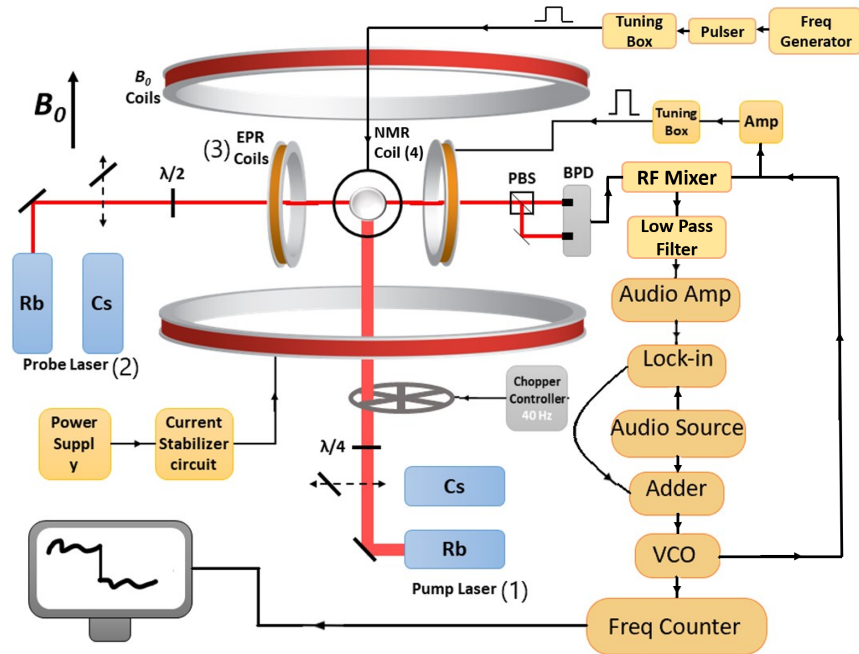


Figure 3.2: Frequency shift measurement setup: 1) 795 and 895 nm pump lasers for Rb and Cs respectively, narrowed to ~ 0.3 nm. 2) 852 nm Cs and 780 nm Rb probe lasers detuned by ≈ 0.6 nm for optical detection of alkali-metal polarization; the probe beam after the cell is focused onto fast-balanced photodiodes. 3) The EPR coil, which is positioned in the normal direction to the main static field. 4) The NMR coil, which is a surface coil placed right below the cell and is driven by a frequency generator and an audio amplifier to produce RF pulses at the noble gas nuclear resonance frequency in order to destroy the noble gas polarization.

parts:

1. Vapor cell (sample): one-inch diameter sealed, uncoated Pyrex-glass spheres were fabricated. They are filled with alkali-metal(s), noble gas (Xe), and buffer gases (^4He and N_2) using our gas handling system.
2. Oven: a chamber to keep the sample and heat it to put the alkali-metal in the

- vapor phase (the oven is being omitted in Fig. 3.1 and Fig. 3.2 for simplicity).
3. Magnetic field: we use Helmholtz configuration for our static magnetic field and EPR coils to ensure that the sample experiences a homogeneous magnetic field.
 4. Pump lasers: we use high-power diode lasers that are tuned to D_1 transitions of alkali-metals to polarize the alkali-metal vapor in our sample optically.
 5. Probe lasers and optical detection: we use low-power diode lasers tuned to ≈ 0.6 nm off the D_2 transition of the alkali-metals and a fast photodiode to monitor the transverse magnetization of our sample via Faraday rotation after applying the RF field.
 6. Pulsed and CW EPR: we use a commercial spectrometer, Redstone (Tecmag), to produce the RF pulse, induce transitions between the hyperfine sub-levels in our polarized sample, and record the resulting FIDs. We use a home-built circuitry with a lock-in scheme to produce the CW RF and monitor the frequency of the alkali-metal hyperfine sub-levels and their frequency shifts.

We use the pulsed EPR technique to measure the alkali-metal spin-destruction rate and polarization, this powerful technique has provided us with advantages over the CW EPR, like producing signals with a higher signal-to-noise ratio and requiring less time to acquire the alkali-metal spectrum. In this technique, only one pulse with a pulse width as short as 300ns in our case is enough to

get the free induction decay signal and do a Fourier transform on it to obtain the alkali-metal frequency spectrum as opposed to the CW method which will take 10s to 100s ms to get the whole spectrum which is not in our favor since the time needed to see changes in the hyperfine populations on the time scales that matter for spin-destruction is in the order of 100 to 1000 μ s.

I will briefly explain parts 1-5 of our experimental setup in the following sections and will explain part 6 in detail in the respective chapters.

3.1 Cell Fabrication

A glass-blower-constructed Pyrex ‘manifold’, consisting of four one-inch diameter spherical cells (Fig. 3.3), is first connected to the vacuum system (Fig. 3.4).

The manifold is designed such that one end is ‘T’ shaped and the other end has a large U-bend, serving as a kinetic trap to prevent the alkali-metal from entering the vacuum system. ‘Retort’ is the upper part of the ‘T’ where the alkali-metal ampule goes. A thorough leak check is conducted using a helium spray and a residual gas analyzer (RGA). Subsequently, after placing the alkali-metal ampule into the retort, we seal the top of the retort by melting the Pyrex using a torch.

After placing the alkali-metal ampule into the retort and sealing it, it is crucial to ensure that the interior of the cells remains isolated from the air. Nevertheless, the cells must be cleaned before introducing the desired gas composition. This cleaning

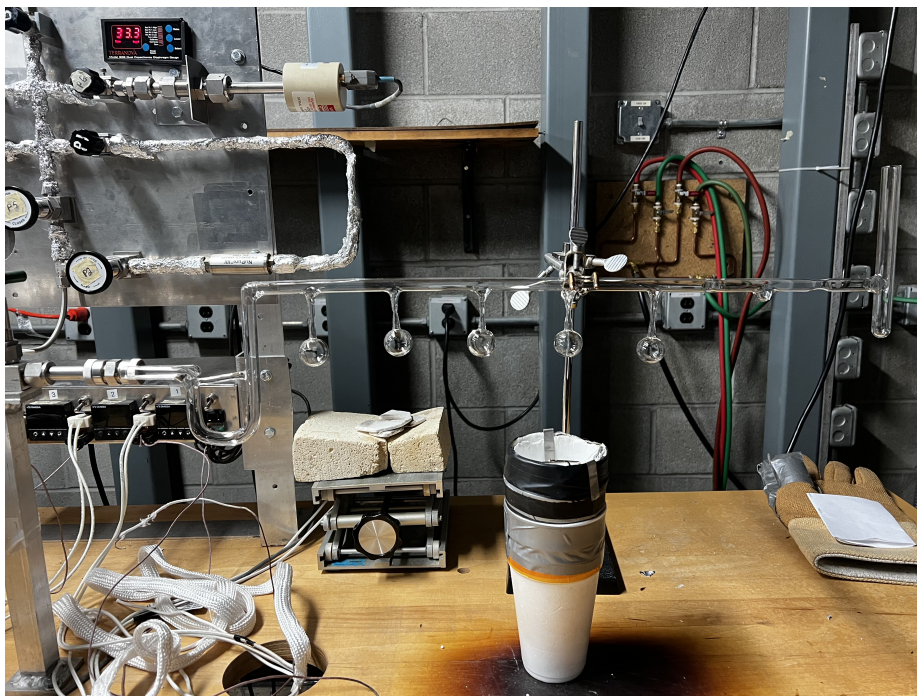


Figure 3.3: Pyrex manifold.

involves wrapping the entire manifold with heat tape, excluding the U-bend and retort. The manifold is then heated to a temperature of 140°C for a few days, and when the pressure gauge on the Turbo pump reads its lowest value and stabilizes for a few hours, the manifold is ready. Once the cells are thoroughly cleaned, the transfer of alkali-metal from the retort to the cells is achieved by gently heating the manifold using a torch set to low heat. The heat causes the alkali-metal to evaporate from the walls of the retort, and due to the maintained vacuum, the alkali-metal easily moves towards the cooler regions of the walls within the cells, where it is collected.

The gas-filling process commences after successfully introducing the alkali-metal into the cells and cooling down the manifold. First, Xe is introduced, which can

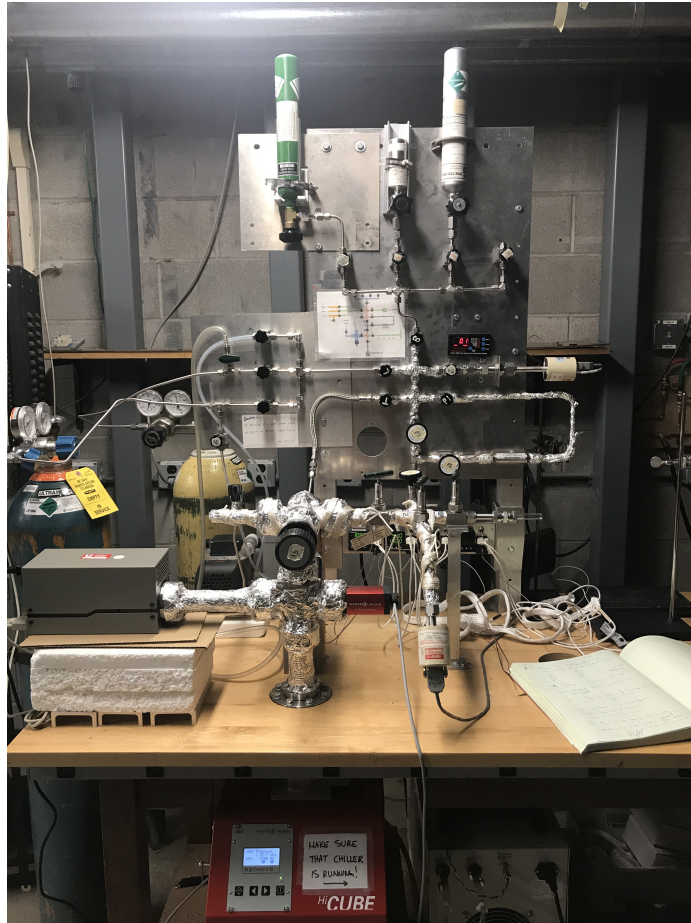


Figure 3.4: Gas handling and vacuum system.

be frozen into the cells using liquid Nitrogen LN_2 . As the entire system is under vacuum, most of the Xe efficiently finds its way to the cell submerged in LN_2 within a few minutes. A pre-measured volume of Xe gas from a container is used to achieve the desired pressure inside the cell. When frozen and then expanded, this volume corresponded to the desired pressure. Opening the Xe gas volume to the manifold while one cell remains under LN_2 instantly causes all pressure gauges to drop to zero. To ensure the presence of Xe in the cells, the LN_2 level is kept constant, and a wait

of a few minutes is required. Next, desired pressures of ^4He and N_2 are trapped in a well-known volume of the gas handling system to give them time to mix before introducing them to the manifold; after mixing, we open that volume to the cell manifold. The final gas pressures in the cell are calculated using the ideal gas law.

After introducing all the desired pressures of gases, we remove the cell from the manifold. The process involves sealing the Pyrex by melting it at the ‘Pulloff’ point while the one-inch sphere is held under LN_2 . Fig. 3.6 is a sample cell we perform experiments on.

We measure the cell volume using Archimedes’ Principle, a fundamental principle in fluid mechanics and hydrostatics. Archimedes’ Principle states that when an object is submerged in a fluid (liquid or gas), it experiences an upward buoyant force equal to the weight of the fluid that it displaces. In simpler terms, when an object is placed in a fluid, it seems to weigh less due to the fluid’s buoyant force exerted on it. This principle explains why things float in water and other fluids. The buoyant force results from the pressure difference between the top and bottom of the submerged object. The pressure at the bottom of the object is greater than the pressure at the top, and this pressure difference creates an upward force that counteracts the object’s weight. The amount of fluid displaced by the object determines the magnitude of the buoyant force [50].

Following the force diagrams in Fig. 3.7, one can find the cell volume V_c which is

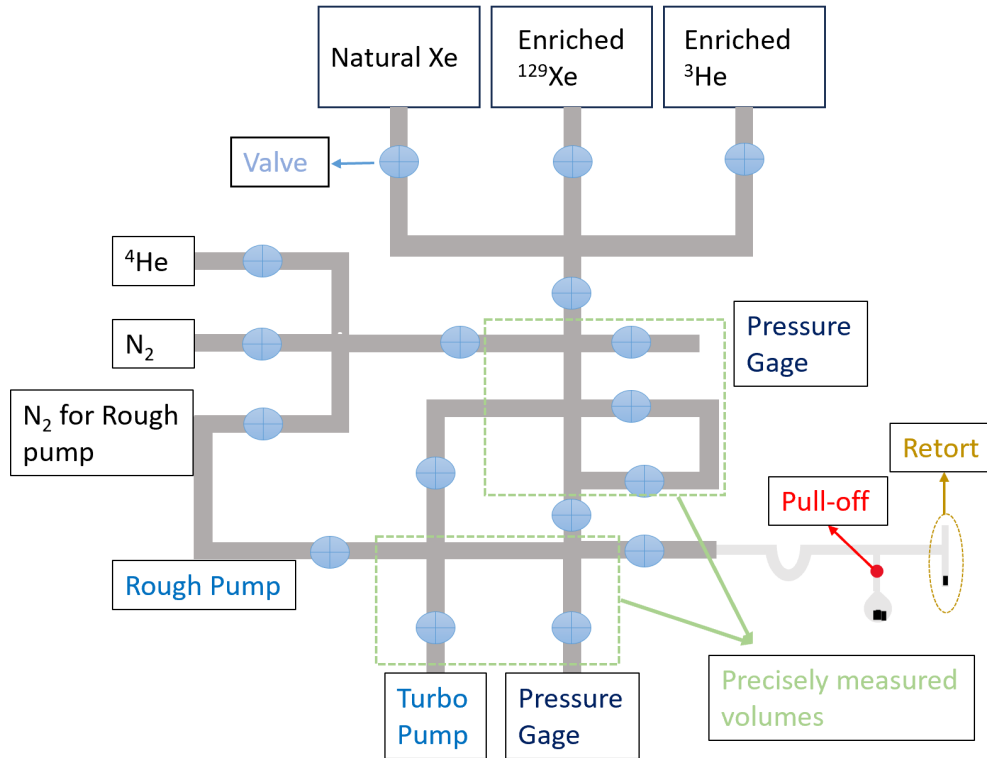


Figure 3.5: Schematic of the gas handling system. A glass blower makes the manifold containing the cells, and then it is attached to the vacuum system, and the volumes are measured. An ampule containing about 1 gram of alkali-metal is introduced into the retort. Subsequently, a section of the manifold containing the cells is sealed, and heating is applied while keeping the Turbo pump operational for a duration of several days. The heat facilitates the transfer of the alkali-metal into the cells. Precisely measured volumes are then filled with enriched Xe at a predetermined pressure, after which the Xe is frozen into the cells using liquid nitrogen (LN_2). Next, the manifold is filled with ^4He and N_2 . The cell is submerged in LN_2 , and a torch is used to melt through the pull-off, detaching the cell from the manifold.

the sum of the alkali-metal V_a , gas V_g and Pyrex $V_p = m_p/\rho_p$ volumes using Newton's



Figure 3.6: Sample cell containing alkali-metal and desired gases.

laws.

$$F_b = \rho_w g V_c \quad (3.1)$$

$$F_B = \rho_w g V_w \quad (3.2)$$

$$T = Mg - \rho_w g V_w \quad (3.3)$$

$$T_s = m_b g \quad (3.4)$$

m_b is the buoyant mass that can be measured using the scale while experimenting,

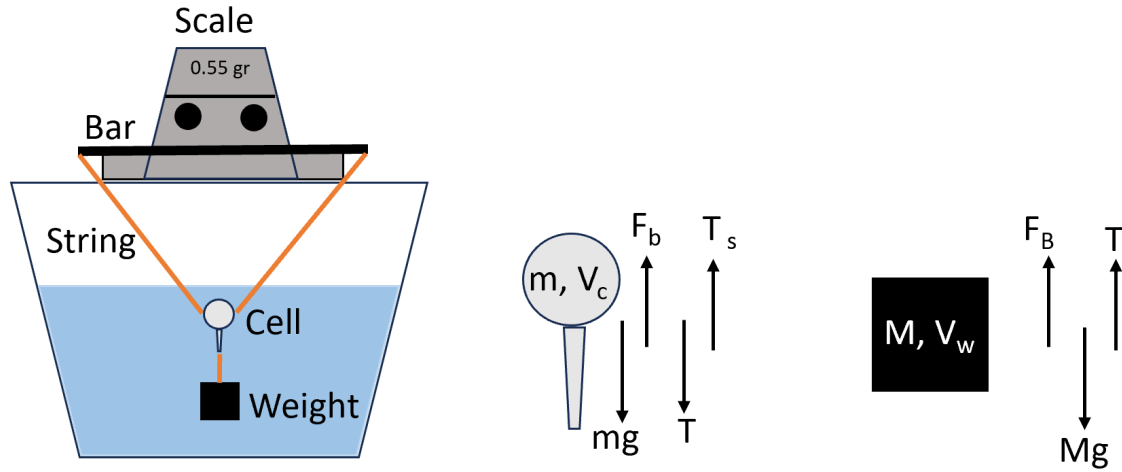


Figure 3.7: Schematic of cell volume measurement using Archimedes principle. Where F_b , m , and V_c are the buoyant force, mass, and volume of the cell, respectively, and F_B , M , and V_w are the buoyant force, mass, and volume of the weight. T and T_s are the string forces.

ρ_w is the water density, F_b and F_B are the buoyant forces of the cell and the weight respectively, m and M are the measured masses of the cell and the weight respectively, V_w is the volume of the weight, T and T_s are the string forces. By applying the Newton's law and simplifying it, we get the following:

$$\rho_w V_c + m_b = m + M - \rho_w V_w \quad \rightarrow \quad V_c = \frac{M + m - m_b}{\rho_w} - V_w \quad (3.5)$$

We know $V_c = V_g + V_a + V_p$ and $m = \rho V$ so

$$V_g = V_c - V_a - V_p = V_c - \frac{m - m_a - m_g}{\rho_p} - V_a \quad (3.6)$$

resulting in

$$V_g = \left(\frac{M}{\rho_w} - V_w \right) + m \left(\frac{1}{\rho_w} - \frac{1}{\rho_p} \right) - \frac{m_b}{\rho_w} + \frac{m_g}{\rho_p} + V_a \left(\frac{\rho_a}{\rho_p} - 1 \right) \quad (3.7)$$

where in this equation M , V_w , ρ_w , ρ_p , ρ_a are known; m , m_b , and m_g are measured; and we estimate V_a when filling the cell.

3.2 Oven

The cell is placed into a specially designed oven, a 5" \times 5" \times 5" box made from 1/8" thick Aluminum sheets held together with non-magnetic brass components and covered with fiberglass insulation to prevent heat loss. We were diligent in avoiding the use of any materials with even slight magnetic properties in and around the spin-exchange oven, as magnetic field variations can lead to spin-relaxation. The oven is equipped with windows that extend alongside the cell. These windows enable a probing beam to traverse through the cell, exiting on the other side perpendicular to the primary magnetic field direction and parallel to the EPR coil axis; another window facilitates optical access from the front to the rear of the oven for optical pumping (Fig. 3.8).

To regulate the temperature, we utilized forced air, which was heated by a process air heater and then directed into the oven through insulated copper tubing (Fig. 3.8). Temperature measurements were obtained using a resistive thermal device (RTD) at-

tached right below the cell. These measurements were fed back to a PID temperature controller, which, in turn, supplied 110 volts to the process air heater as necessary, accomplished through a zero-switching solid-state relay.



Figure 3.8: spin-exchange oven.

3.3 Magnetic Fields

3.3.1 *Static Magnetic Field*

We need a static magnetic field to have a Zeeman splitting, help the spins' alignment, and prevent them from losing their polarization due to stray of magnetic fields. The static magnetic field in our setup is produced by a set of coils having Helmholtz configuration with a diameter of 24", 283 turns per coil, and 3.16 A through each coil (total of 6.33 A) to produce a magnetic field of ~ 28 G in the case of ^{87}Rb measurements, and having a total current of ~ 10 A to produce a magnetic field of ~ 46 G in the case of Cs measurements (Fig. 3.9).

The coils are mounted on a table so that the produced field has the same axis as



Figure 3.9: Helmholtz coils producing the static magnetic field $B_0 \sim 28$ G and $B_0 \sim 46$ G, being water cooled using copper tubes and room-temperature chiller.

the pumping laser optical axis. The coils are operated with a water cooling system and are driven with two power supplies from Hewlett-Packard with a maximum output voltage of 40 V and a maximum output current of 10 A, giving us the ability to increase the output current to the coils without pushing the power supplies to their limits. To stabilize B_0 , we use a home-built current stabilization circuit to stabilize the current through the coils, the details of which can be found in [51].

3.3.2 *The Oscillating Magnetic Field*

The oscillating magnetic field B_1 will induce the spin transition between the hyperfine sublevels, and two Teflon coils of diameter 3.5" with a single turn of copper tape around them having quasi-Helmholtz configuration produce this field, and the cell is placed in the middle of the two coils, these coils are called the EPR coil. The EPR coil is driven by an RF wave at the alkali-metal resonance frequency. To have a maximum power transmission between the amplifier and the EPR coil, we do an impedance match at 50 Ω between the EPR coil, which is an inductor, and the amplifier. We also want the EPR coil to resonate at the hyperfine frequency. For tuning and matching the EPR coil, we use the concept of tank circuits in which the inductor is capacitively coupled such that at the desired frequency, the amplifier output impedance and the inductor impedance are matched.

One problem with a tuned and matched coil (high Q coil) is that it will ring down when it resonates. For the pulsed EPR experiment, the goal is to always generate the largest possible oscillating magnetic field B_1 with the shortest pulse width, such that the product of the two generates the desired tip angle to put the spins into the transverse plane. The short pulse width allows it to cover the spectrum so that its Fourier transform is broad enough that all the hyperfine transitions are equally excited. The ringdown is a problem for two reasons: (1) it makes the effective pulse longer and narrows the corresponding excitation spectrum, so that it might not be

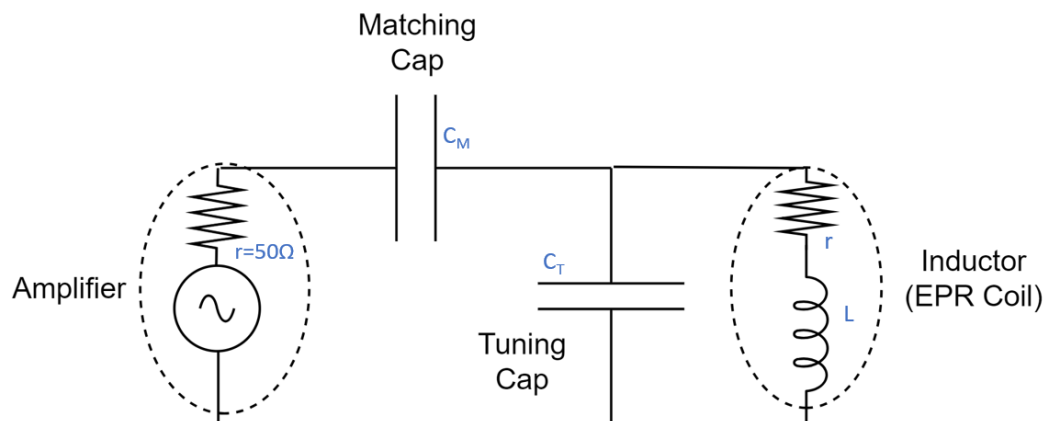


Figure 3.10: Tuning circuit: to tune the EPR coil to resonate at the alkali-metal hyperfine frequency and to be impedance matched with the amplifier.

covering the spectrum equally and (2) it can lead to a longer dead time, where we are trying to optically detect the early part of the decay of the precessing magnetization but the pulse is still going and the resulting nutation of the spins interferes with free precession (Fig. 3.12).

In our experiments, we use the pulsed EPR technique to assess the longitudinal magnetization as a function of time. For that assessment to be accurate, i.e., for

the area under the spectrum to be proportional to the longitudinal magnetization, we need to tip all the electrons by the same amount and do it so quickly that they don't have time to start decohering significantly before we optically detect them. The orientation of the EPR coil plays a significant role in this assessment as well, since particularly at low polarization where there is a significant population in the $F = 1$ manifold, it's crucial that the peaks in this manifold point downward, opposite to those in the upper manifold ($F = 2$), for that reason we placed the EPR coil in a way that its axis was perpendicular to the static magnetic field B_0 and parallel to the direction of the probe beam. The accuracy of our data depends on this. One possible solution to reduce the ringdown is to spoil the Q of the EPR coil, and this has the effect of reducing B_1 , but, for example, if we just turned down the power amplifier, this wouldn't solve the problem because the spectral coverage would be the same and the ringdown time would be exactly the same. For spoiling the probe Q we added a resistance component parallel to the EPR coil to dump some of the power on the resistor while keeping the impedance of the coil matched at 50Ω (3.11).

Using a known dummy signal, we measured and calculated the inductance and resistance of our EPR coil to be $L = 0.6 \mu\text{H}$, $r_{\text{DC}} = 0.08 \Omega$ and $r_{\text{AC}} = 1.2 \Omega$ at 20 MHz. We used the LTspice simulation software to estimate the values of the capacitors needed for the tuning box, which came out to be ~ 70 pf for the tuning capacitor and ~ 30 pf for the matching capacitor, in the case of ^{87}Rb at ~ 19 MHz

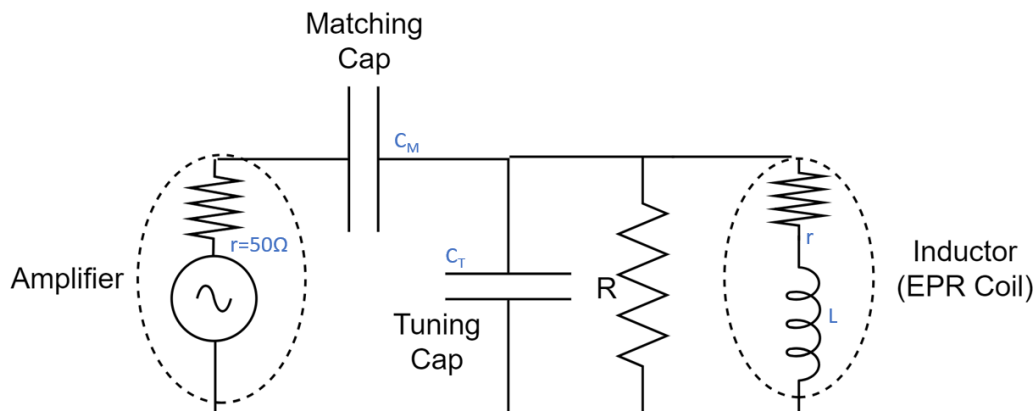


Figure 3.11: Tuning circuit: for spoiling the Q of the EPR coil while being tuned to the EPR frequency and impedance matched with the output impedance of the amplifier, one can add a resistor parallel to the inductor to reduce the current to the inductor.

resonance frequency. In the case of Cs at ~ 14 MHz resonance frequency the tuning capacitor turned out to be ~ 65 pf and matching capacitor was ~ 40 pf, knowing that these values were not the absolute values but giving us an idea about the range of capacitors we needed. For building the tuning boxes, we used Voltronics variable capacitors to be able to fine-tune the values of capacitors and tune and match the coils more easily. We used the vector network analyzer (VNWA) from SRD kits to find the sweet spot for the capacitors where the EPR coil was both matched and tuned, and by adding a resistor $\sim 120 \Omega$ parallel to the coils to spoil the Q of the EPR coil, we reduced the strength of B_1 and were able to get clean FID signals (Fig. 3.12).

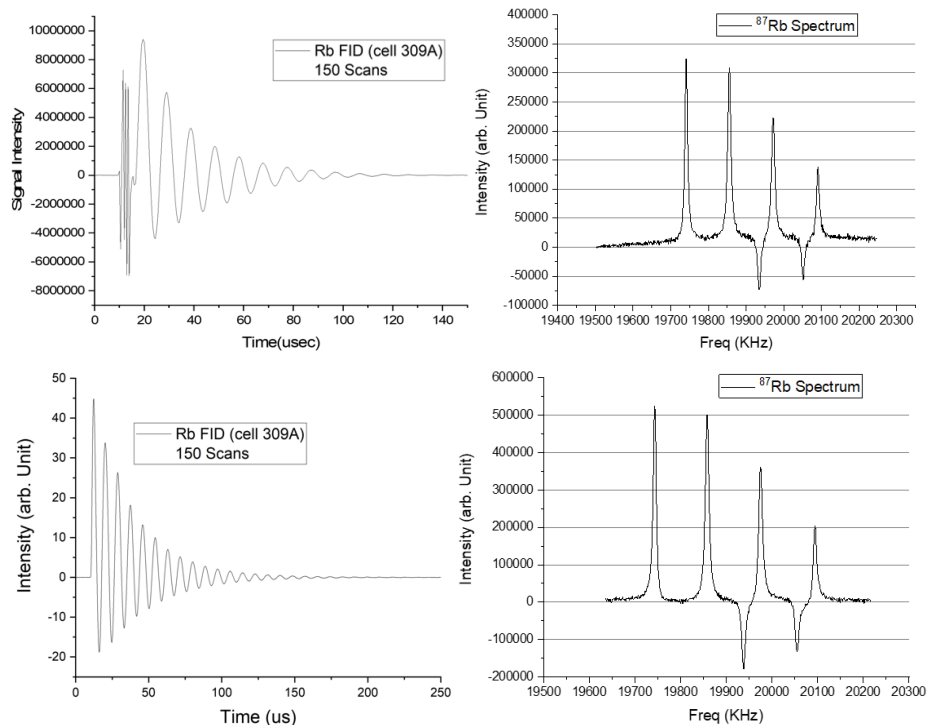


Figure 3.12: ^{87}Rb FID signal (figures on the right) and spectrum (figures on the left) which is the result of FFT on the FID before (top figures) and after (bottom figures) spoiling the Q of the EPR coil. The ringdown was introducing noise to the FID signal (top left figure) and it was distorting the baseline of the spectrum (top right figure). After spoiling the Q the spectrum baseline issue got resolved (bottom right figure).

3.4 Pump Laser

The diode-laser array (DLA) is the preferred type of laser for SEOP. This preference primarily arises from its cost-effectiveness and straightforward capability to deliver substantial power, potentially reaching wattage in the hundreds. This sets it apart from alternatives like dye or Ti:Sapphire lasers functioning at 795 nm [43, 52]. It's crucial to keep in mind that the typical DLA exhibits a line width of roughly

1000 GHz (~ 2 nm), which is significantly wider than the 20 GHz/bar absorption line width of alkali-metal atoms like Rb, according to [53]. Traditionally, the method of broadening the absorption line width of alkali-metal atoms involves subjecting the system to elevated pressures of ^3He or ^4He gas, typically ranging from 3 to 10 bars. However, even when utilizing the high pressure of 10 bars, a substantial portion of the light remains unabsorbed. Specific applications, such as neutron spin filters, which necessitate low-pressure cells at around 1 bar ([43]), further reduce the effectiveness of using these types of lasers. Consequently, people tried to amplify the efficiency of using DLA lasers. A promising approach involves utilizing diode arrays with 1-2 emitters capable of generating power outputs ranging from 2 to 4 w. These arrays have showcased improved performance in SEOP when their emission is refined through external cavities. This approach is detailed in the discussions presented in Ref. [54]. Furthermore, a technique proposed in Ref. [55] outlines the usage of Etalon for feedback in order to narrow the line width of a DLA.

In our setup, we use two 40 W diode-laser arrays from DILAS laser, one for Rb and one for Cs, to optically polarize the alkali-metal vapor. These lasers are tuned to resonate precisely at the 795 nm D_1 frequency for ^{87}Rb and 895 nm D_1 frequency for Cs and subsequently refined with great care, resulting in a notably narrow bandwidth of ~ 0.3 nm (equivalent to roughly 130 GHz). This refinement process was conducted using a Littrow cavity, as explained in Ref. [56]. In this technique, the laser acts as an

almost concentrated point source, with divergence being diffraction-limited in both directions. To collimate and expand the laser beam, we use two spherical lenses. The outcome of this collimated emission is then guided towards an adjustable diffraction grating, serving the purpose of selectively directing a specific wavelength back into the diode array. This feature enables the controlled tuning of the output wavelength. In particular, the first-order diffraction from the grating is the feedback for frequency and line width adjustment. Fig. 3.13 shows the schematic of the Littrow cavity in our setup, and Fig. 3.14 shows a picture of our setup.

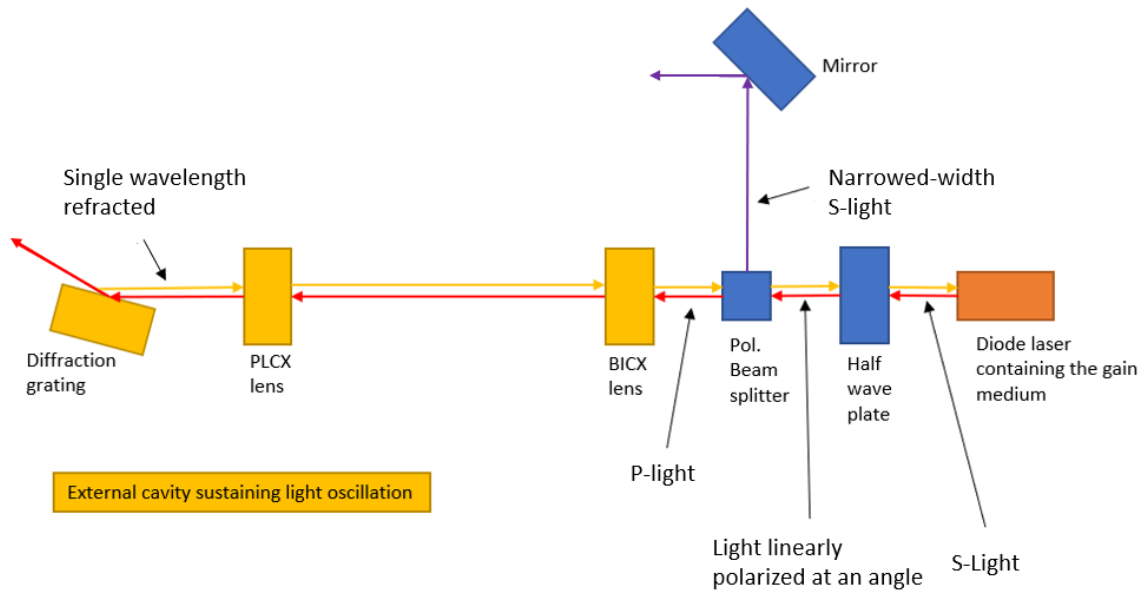


Figure 3.13: Schematic of narrowing a diode laser array using a Littrow cavity.

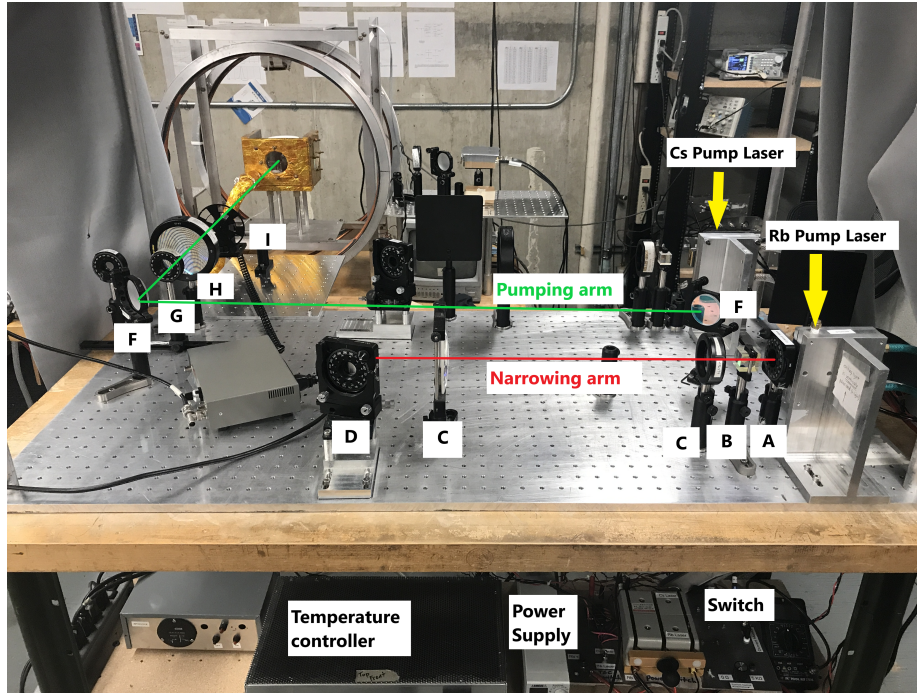


Figure 3.14: Picture of our pump laser optical table. Elements A-D show the narrowing arm and elements F-I show the pumping arm. ‘A’ is a 1/2 wave plate to adjust the amount of light that goes to each arm. ‘B’ is a polarizing beam splitter that splits the beam in the directions of the narrowing and pumping arms. ‘C’ is a spherical lens with a 50 mm focal length and 50 mm diameter. ‘D’ is a spherical lens with a 100 mm focal length and 100 mm diameter. ‘F’ is a set of mirrors on a rotational base, changing between Rb and Cs lasers. ‘G’ is a 1/4 wave plate to change the linearly polarized laser beam to a circularly polarized beam. ‘H’ is a spherical lens with a 50 mm focal length and 100 mm diameter to expand the beam and reflect it on the cell. ‘I’ is an optical chopper for measurements in the dark.

3.5 Optical Detection and Probe laser

We do optical detection based on Faraday rotation, using a 120 mW distributed-Bragg-reflection (DBR) diode laser array from Photodigm. The laser propagates transverse to the applied field and is detuned ≈ 0.6 nm from the D₂ resonance (780

nm and 852 nm for Rb and Cs, respectively). In the Faraday effect, the plane of polarization of a linearly polarized light rotates when it passes through a magnetized material. Faraday rotation within a magnetic field has been thoroughly investigated and utilized to measure both the density of alkali-metal vapor and its polarization [57, 58, 59]. We detect the Faraday rotation of the linearly polarized probe beam. In our detection setup, as shown in Fig. 3.15, after the probe lasers, we have a $\lambda/2$ wave plate, the sample cell, a lens to focus the light, a polarizing beam splitter cube, and a set of balanced photodiodes from Thorlabs that will subtract and amplify the two input signals (Fig. 3.16).

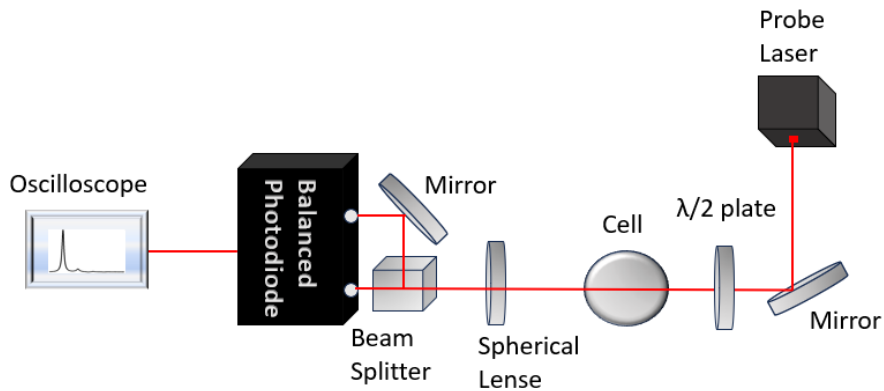


Figure 3.15: The schematics of our detection setup.

Under conditions of no optical pumping, the $\lambda/2$ wave plate is configured such that the photodiodes yield a combined output current of zero (meaning equal light to each arm of the photodiode). However, when the alkali-metal vapor possesses a

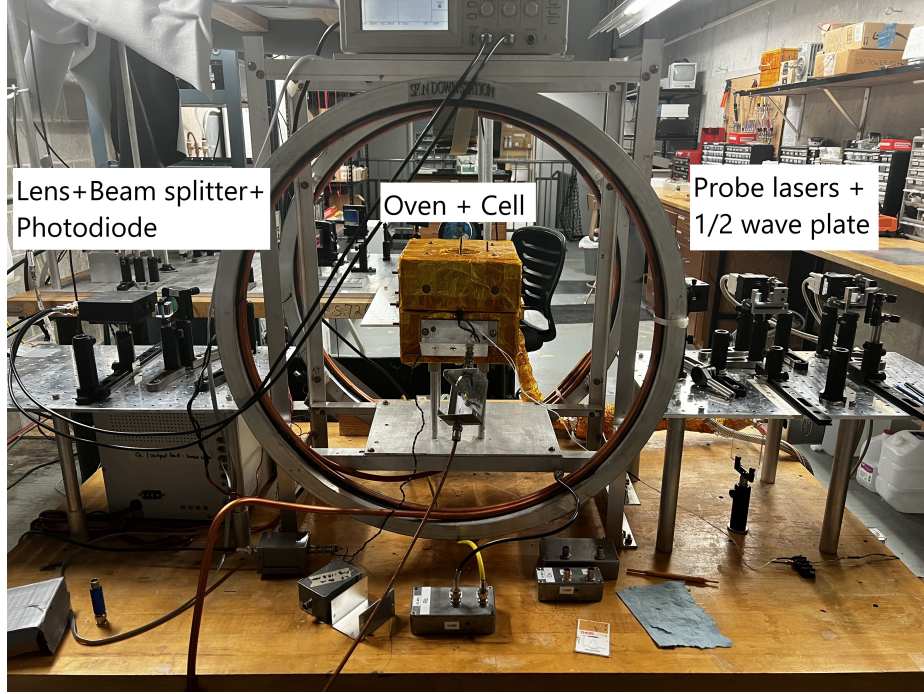


Figure 3.16: Picture of our detection setup.

polarization, it induces a Faraday rotation angle θ on the linear polarization of the probe beam, as explained by [43].

$$\theta = \frac{\pi[A]le^2}{3m_e c} \left(\frac{1}{\Delta_{3/2}} - \frac{1}{\Delta_{1/2}} \right) P \quad (3.8)$$

where $[A]$ is the alkali-metal number density, l is the path length through the alkali-metal vapor, e and m_e are the electron charge and mass, respectively, P is the alkali-metal polarization, $\Delta_{3/2}$ and $\Delta_{1/2}$ are the angular frequency detunings of the probe beam from the D_2 and D_1 resonances, respectively. In practice, we use D_2 light for Faraday rotation, and the $1/\Delta_{1/2}$ term is negligible. The photodiode produces a

current proportional to $\sin(\theta)$, as long as θ is small, the photodiode current directly maps the shape of each of the hyperfine resonances and is directly proportional to the Rb magnetization.

CHAPTER 4

SPIN-DESTRUCTION RATE MEASUREMENTS

4.1 Introduction

The emergence of MRI for human subjects through the utilization of hyperpolarized noble gases [6] has spurred significant advancements in Xe-alkali-metal SEOP [29] within high-pressure buffer gases [52]. One crucial question is which alkali-metal is the best partner for polarizing Xe. Rb has generally been favored in this respect over the past few decades due to the availability of inexpensive high-power diode lasers at the Rb D₁ wavelength (795 nm). However, Cs has some practical advantages: it has a higher vapor pressure than Rb at a given temperature, and the optical pumping rate per watt for Cs is 12% faster than Rb. So, studying the SEOP efficiency in different systems is essential to understand which alkali-metal Rb or Cs is the best candidate for producing hyperpolarized Xe. The SEOP efficiency is:

$$\eta_{\text{se}} = \frac{\gamma_{\text{se}}/[A]}{\Gamma_{\text{A}}^{(\text{Xe})}/[\text{Xe}]} = \frac{k_{\text{se}}[\text{Xe}]}{\Gamma_{\text{A}}^{(\text{Xe})}} \quad (4.1)$$

where $[A]$ and $[\text{Xe}]$ are the alkali-metal and noble gas Xe number densities, γ_{se} is the alkali-metal-noble gas spin-exchange rate due to collisions with Xe, $\Gamma_{\text{A}}^{(\text{Xe})}$ is the alkali-metal electron-randomization rate due to collisions with Xe, and k_{se} is the alkali-metal-noble gas spin-exchange rate coefficient.

Although high-pressure of He is widely used for spin-exchange between Xe and alkali-metals, there is a significant absence of thorough studies on spin-relaxation and spin-exchange rates in these particular high-pressure circumstances, especially in the case of the Xe-Cs system. Some studies have presented spin-relaxation rates for the Xe-Rb system [45, 34], but few studies on Xe-Cs exist. In this study, we present the alkali-metal spin-destruction rates for Xe-Rb and Xe-Cs systems at different pressures with the same gas composition ${}^4\text{He}(94\%)\text{-N}_2(3\%)\text{-Xe}(3\%)$, which is similar to the ones used in magnetic resonance imaging polarizers, and compare the two. Collision-related phenomena govern the characteristics of spin-relaxation in the Xe-alkali-metal SEOP process, and a comprehensive theory outlining their impacts can be found in [13]. As introduced in Chapter 2, the alkali-metal-Xe van der Waals molecules with a binding energy of roughly 20 meV [60] and binary collisions between the two species result in the alkali-metal electron spin-relaxation. In typical SEOP experiments at pressures on the order of an atmosphere, the primary share of spin-relaxation stems from binary collisions since the molecules are loosely bound and can be easily broken up by any collisions. However, the contribution from molecules is still significant.

The molecular behavior of alkali-metal-noble gas is a function of gas density as explained in [13, 12]. Based on what was described in Chapter 2, section 4, considering the hyperfine period \hbar/A where A is the hyperfine interaction coefficient as a reference, at low enough gas pressure, the molecular lifetime τ is longer than the

hyperfine period, preserving the coupling of alkali-metal electron spin \mathbf{S} to both its nucleus \mathbf{I} and the molecule's rotational angular momentum \mathbf{N} via the spin-rotation interaction. In this regime, which is known as the 'long lifetime' regime [34], the molecular contribution to the spin-relaxation rate increases as the gas density increases due to the consequent increase of the molecular formation rate $1/T_{\text{vw}}$. As the gas pressure increases, there is a region where τ and hyperfine period are comparable, resulting in the saturation of molecules' contribution to the spin-relaxation rate. As the molecular formation and break-up rates compete, it results in a short molecular lifetime that interferes with the coupling of \mathbf{S} to \mathbf{N} , but $\mathbf{I} \cdot \mathbf{S}$ coupling is still strong. This is called the 'short lifetime' regime. At even higher gas pressure where τ is much shorter than the hyperfine and spin-rotation (\hbar/γ where γ is the spin-rotation interaction coefficient) periods, both $\mathbf{I} \cdot \mathbf{S}$ and $\mathbf{N} \cdot \mathbf{S}$ become weak. This is known as the 'very short lifetime' regime [34]. This chapter represents the study of the alkali-metal spin-destruction rate for Xe-Rb and Xe-Cs systems in the short and very short lifetime regimes, where the spin-destruction of the alkali-metal atoms is primarily due to the binary collisions with Xe. Still, we measure the molecular contribution as well.

4.2 Theory

The alkali-metal vapor polarimetry technique we follow draws inspiration from a procedure introduced by the team at Princeton [44]. Their approach involves utilizing

a transverse RF field adjusted to match the resonance frequency of the alkali-metal electron paramagnetic resonance (EPR). This configuration generates a transition of spins between the hyperfine sub-levels, which depends on the polarization of the alkali-metal atoms, and a transversely probing beam with circular polarization detects this transition. One can establish the relative populations of different energy levels by sweeping the RF frequency across all the Zeeman sub-levels of the alkali-metal atoms. When integrated, the appropriate proportion of these sub-level transition areas represents the absolute polarization of alkali-metal. In this study, we follow a version of this technique, building upon the principles of Faraday rotation as described in Refs. [59, 58]. Instead of directing a circularly polarized probing beam perpendicular to the sample cell, we require a weak, linearly polarized probe beam. As a result of Faraday rotation, when the RF frequency aligns with the Rb resonance, the probe beam undergoes a rotation due to the circular dichroism. The degree of rotation angle is inversely correlated with the Rb polarization. By sweeping the RF frequency across all the Zeeman sub-levels of alkali-metal atoms, one can derive information about the relative populations of each sub-level.

4.2.1 Alkali-Metal Polarimetry

The alkali-metal ground state Hamiltonian in the presence of an oscillating transverse magnetic field $B_x \cos(\omega t)\hat{i}$ and, in the absence of light, is [13]

$$H = H_0 + g_s \mu_B S_x B_x \cos \omega t \quad (4.2)$$

where H_0 is the RF-free Hamiltonian with eigenenergies E_m and eigenstates $|m\rangle$. The resonance peaks will be resolved completely with high polarization and a large enough static magnetic field. The time evolution of population transfer between the two states $|m\rangle$ and $|m-1\rangle$ due to the oscillating magnetic field is [61]

$$\begin{aligned} \frac{d\rho_{m,m-1}}{dt} = & (E_m - E_{m-1} - \omega) \rho_{m,m-1} - i\gamma_A \rho_{m,m-1} \\ & + V_{m,m-1} (\rho_{m-1} - \rho_m) \end{aligned} \quad (4.3)$$

where $\rho_{m,m-1} = \langle m|\rho|m-1\rangle$ is the transition probability, ρ_m and ρ_{m-1} are the number densities of states $|m\rangle$ and $|m-1\rangle$ with energies E_m and E_{m-1} , respectively, γ_A is the spin-destruction rate of the alkali-metal and

$$V_{m,m-1} = \langle m|g_s \mu_s S_x B_x|m-1\rangle \quad (4.4)$$

Considering the form of Eq. 4.3, it is valid to assume exponential form $\rho_{m,m-1} =$

$\sigma e^{-i\omega t}$ as a solution and by substituting it into Eq. 4.3 we get

$$\frac{id\sigma}{dt} = (E_m - E_{m-1} - \omega)\sigma - \frac{i\gamma_A\sigma}{2} + \frac{\langle m|V|m-1\rangle(\rho_{m-1} - \rho_m)}{2} \quad (4.5)$$

In the steady state where $\frac{id\sigma}{dt} = 0$ one can get

$$\sigma = \frac{\langle m|V|m-1\rangle(\rho_{m-1} - \rho_m)/2}{(E_m - E_{m-1} - \omega) - i\gamma_A/2} \quad (4.6)$$

The time evolution of density for each $|m\rangle$ and $|m-1\rangle$ sub-level is [61]

$$\frac{id\rho_m}{dt} = \langle m|V|m-1\rangle(\sigma^*/2) - \langle m-1|V|m\rangle(\sigma/2) \quad (4.7)$$

$$\frac{id\rho_{m-1}}{dt} = \langle m-1|V|m\rangle(\sigma/2) - \langle m|V|m-1\rangle(\sigma^*/2) \quad (4.8)$$

then one can use Eqs. 4.6, 4.7 and 4.8 and get

$$\begin{aligned} \frac{d\rho_m}{dt} - \frac{d\rho_{m-1}}{dt} &= \langle m|V|m-1\rangle(\sigma^*/2) - \langle m-1|V|m\rangle(\sigma/2) \\ &\quad - \langle m-1|V|m\rangle(\sigma/2) + \langle m|V|m-1\rangle(\sigma^*/2) \\ &= 2\langle m|V|m-1\rangle(\sigma^*/2) - 2\langle m-1|V|m\rangle(\sigma/2) \\ &= \frac{|\langle m|V|m-1\rangle|^2\gamma_A(\rho_m - \rho_{m-1})}{(E_m - E_{m-1})^2 + \gamma_A^2/4} \end{aligned} \quad (4.9)$$

knowing $\langle m|V|m-1\rangle = \frac{F(F+1)-m(m-1)}{4(2I+1)^2}g_s\mu_B B_x$ [13], the simple form of Eq. 4.9 is

$$\frac{d(\rho_m - \rho_{m-1})}{dt} = \left(\frac{\gamma_A}{(E_m - E_{m-1} - \omega)^2 + \gamma_A^2/4} \right) \left(\frac{g_s\mu_B B_x}{4(2I+1)^2} \right) (F(F+1) - m(m-1)) \left(\frac{\rho_m - \rho_{m-1}}{4} \right) \quad (4.10)$$

So one can say that the time evolution of population transition between two sub-levels $|m\rangle$ and $|m-1\rangle$ is proportional to $(F(F+1) - m(m-1))(\rho_m - \rho_{m-1})$ [61]. Being in the spin temperature limit [13] where $\rho = \frac{e^{\beta I_z} e^{\beta S_z}}{Z_I Z_s}$ with Z_I and Z_s being the nuclear and electron partition function and β being the spin temperature parameter and based on Eq. 4.10 one can assume the ratio of areas under the two successive resonance peaks is [61]

$$A = \frac{F(F+1) - m(m-1)}{F(F+1) - (m-1)(m-2)} e^\beta \quad (4.11)$$

In Refs. [29] and [13], it is indicated that while being in the spin temperature limit, the alkali-metal polarization is

$$P = 2\langle S_z \rangle = \tan(\beta/2) = \frac{e^{\beta/2} - e^{-\beta/2}}{e^{\beta/2} + e^{-\beta/2}} = \frac{e^\beta - 1}{e^\beta + 1} \quad (4.12)$$

Substituting e^β from Eq. 4.11 into Eq. 4.12 we get

$$P = \frac{[F(F+1) - (m-1)(m-2)]A - [F(F+1) - m(m-1)]}{[F(F+1) - (m-1)(m-2)]A + [F(F+1) - m(m-1)]} \quad (4.13)$$

For example, in the case of ^{87}Rb with $I = 3/2$ we have

$$P = \frac{3A - 2}{3A + 2} \quad (4.14)$$

where here A is the ratio of areas under the peaks of the $|22\rangle \rightarrow |21\rangle$ and $|21\rangle \rightarrow |20\rangle$ transitions (Fig. 4.1).

If the polarization of the sample is not high enough, and the static magnetic field is not large enough, then we have partially resolved peaks and in this case [61]

$$P = \frac{2A - 1}{2A + 1} \quad (4.15)$$

where now A is the ratio of the area under the peak of $|22\rangle \rightarrow |21\rangle$ transition to the combined area of $|21\rangle \rightarrow |20\rangle$ and $|11\rangle \rightarrow |10\rangle$ transitions.

4.2.2 Alkali-Metal Relaxation Rate Measurement

By measuring the relaxation of the spin polarization in the dark, an experimental technique developed by Franzen [49], significant information can be learned regarding the relaxation mechanisms of alkali-metal atoms. For this technique, we use an optical

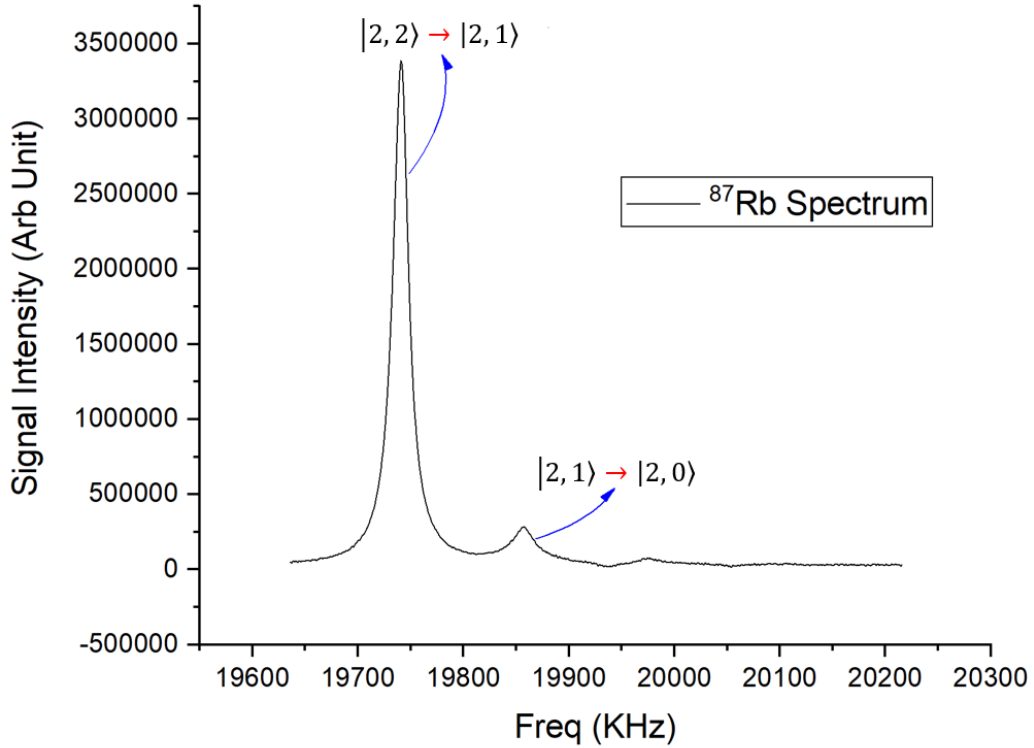


Figure 4.1: ^{87}Rb spectrum with high polarization and in the presence of ~ 28 G magnetic field, all the resonance peaks are well resolved.

chopper, which is placed in the way of our pump laser beam path, close to the focal point of the last lens in the optical train of the pump beam. Then, we record the FID at different time intervals to get the alkali-metal polarization decay. The alkali-metal relaxation transient we observe experimentally refers to the longitudinal electron spin polarization $\langle S_z \rangle$. Working through the theory for a mono-isotopic alkali-metal like Cs is more convenient. Then, it can be generalized to a poly-isotopic alkali-metal like Rb, where the isotopic average should be incorporated. Longitudinal spin polarization

evolution is described as [13]

$$\frac{d\langle F_z \rangle}{dt} = \frac{d(\text{Tr}(F_z \rho))}{dt} = \text{Tr} \left(F_z \frac{d\rho}{dt} \right) \quad (4.16)$$

Eq. 4.16 is a nonlinear equation, so the solution to this equation cannot be described as a finite sum of exponentials. However, in the low polarization limit, the nonlinear terms become negligible compared to linear terms; hence, at this stage of polarization, $\langle F_z \rangle$ can be given as a linear combination of single exponential with different time constants. In the spin temperature limit, a paramagnetic coefficient ϵ can be introduced to express the alkali-metal atomic spin polarization $\langle F_z \rangle$ in terms of the electron spin polarization $\langle S_z \rangle$,

$$\langle F_z \rangle = (1 + \epsilon) \langle S_z \rangle \quad (4.17)$$

this paramagnetic coefficient at a low polarization limit is $\epsilon = (4/3) I(I + 1)$ [13]. We label the upper and lower manifolds of total spin projection as $\langle a_z \rangle$ with $a = I + 1/2$ and $\langle b_z \rangle$ with $b = I - 1/2$ respectively where $\langle F_z \rangle = \langle a_z \rangle + \langle b_z \rangle$. In general, the decays of $\langle F_z \rangle$ and consequently $\langle S_z \rangle$ are complicated, but as shown by [13] under certain conditions at low polarization, all spins decay similarly, and they can be described by multi-exponential decay with different time constants corresponding to all the relaxation modes of $\langle a_z \rangle$ and $\langle b_z \rangle$. At this low polarization, one of these relaxation

modes is much longer than the others, representing the slowest relaxation mode, enabling us to isolate it from the others and measure it. The time evolution of the upper $\langle a_z \rangle$ and lower $\langle b_z \rangle$ manifold spins is [13]

$$\frac{d}{dt} \begin{pmatrix} \langle a_z \rangle \\ \langle b_z \rangle \end{pmatrix} = \begin{pmatrix} A\langle a_z \rangle + B\langle b_z \rangle \\ C\langle a_z \rangle + D\langle b_z \rangle \end{pmatrix} \quad (4.18)$$

which can be written in a simpler and more familiar form of

$$\frac{d}{dt} \begin{pmatrix} \langle a_z \rangle \\ \langle b_z \rangle \end{pmatrix} = -\tilde{\Gamma} \begin{pmatrix} \langle a_z \rangle \\ \langle b_z \rangle \end{pmatrix} \quad (4.19)$$

with $-\tilde{\Gamma} = \begin{pmatrix} A & B \\ C & D \end{pmatrix}$. considering the equations for evolution of $\langle a_z \rangle$ and $\langle b_z \rangle$, it is valid to suggest the followings as possible solutions

$$\begin{aligned} \langle a_z \rangle &= c_1 e^{-\gamma_1 t} + c_2 e^{-\gamma_2 t} \\ \langle b_z \rangle &= d_1 e^{-\gamma_1 t} + d_2 e^{-\gamma_2 t} \end{aligned} \quad (4.20)$$

where γ_1 and γ_2 are the common time constants corresponding to different relaxation

modes of the decay. Substituting these suggested solutions into Eq. 4.19 we get

$$\begin{aligned}\tilde{\Gamma} \begin{pmatrix} c_1 \\ d_1 \end{pmatrix} &= \gamma_1 \begin{pmatrix} c_1 \\ d_1 \end{pmatrix} \\ \tilde{\Gamma} \begin{pmatrix} c_2 \\ d_2 \end{pmatrix} &= \gamma_2 \begin{pmatrix} c_2 \\ d_2 \end{pmatrix}\end{aligned}\tag{4.21}$$

One can write Eq. 4.21 in a more compact form, $\tilde{\Gamma}\mathbf{V} = \gamma\mathbf{V}$, in which \mathbf{V} and γ are the eigenvector and eigenvalue of the $\tilde{\Gamma}$, respectively, and the smallest eigenvalue corresponds to the slowest decay rate that we measure experimentally. In general, in every SEOP experiment, the evolution of spin polarization of the alkali-metal atom is governed by these processes [13]

- The hyperfine interaction $\mathbf{I} \cdot \mathbf{S}$.
- The Zeeman effect on both nuclear and electron spins $\mathbf{I} \cdot \mathbf{B}$ and $\mathbf{S} \cdot \mathbf{B}$.
- The optical pumping.
- Spatial diffusion of the polarized atoms.
- Alkali-metal-alkali-metal spin-rotation and spin-exchange collisions.
- Alkali-metal-buffer gas spin-rotation collisions.
- Alkali-metal-noble gas spin-rotation and spin-exchange collisions.

- Alkali-metal-noble gas van der Waals molecule formation in the presence of a third body.

Many of these processes are sudden with respect to alkali-metal nuclear polarization or with respect to the hyperfine period, meaning their correlation time τ_c is much shorter than $\tau_{\text{HF}} = \hbar/A\mathbf{I} \cdot \mathbf{S}$, resulting in the sudden processes that only involve electron spin and will leave nuclear spin intact. The nuclear polarization will be affected indirectly by interacting with electrons between collisions. Therefore, the density matrix is usually written as the sum of electron polarization part ρ_S and a part without electron polarization $\rho_{\bar{S}}$ which won't be affected by these sudden processes [13]

$$\rho = \rho_S + \rho_{\bar{S}} \quad (4.22)$$

where $\rho_{\bar{S}} = \frac{1}{4}\rho + \mathbf{S} \cdot \rho\mathbf{S}$ and $\rho_S = \frac{3}{4}\rho - \mathbf{S} \cdot \rho\mathbf{S}$ and they are labeled as ϕ and $\Theta \cdot \mathbf{S}$ in [13]. All the above processes govern the density matrix time evolution [13]:

- The hyperfine ($\mathbf{I} \cdot \mathbf{S}$) and Zeeman interactions ($\mathbf{I} \cdot \mathbf{B}$) and ($\mathbf{S} \cdot \mathbf{B}$):

$$\frac{d\rho}{dt} = \frac{1}{i\hbar}[H, \rho] \quad \text{where} \quad H = A\mathbf{I} \cdot \mathbf{S} + g_s\mu_B\mathbf{S} \cdot \mathbf{B} - \frac{\mu_I}{I}\mathbf{I} \cdot \mathbf{B}. \quad (4.23)$$

- The optical pumping with pumping rate R and the mean photon spin \mathbf{s} :

$$\frac{d\rho}{dt} = -R\rho_S + 2R\mathbf{s} \cdot \mathbf{S}\rho_{\bar{S}}. \quad (4.24)$$

- Spatial diffusion:

$$\frac{d\rho}{dt} = D\Delta^2\rho, \quad (4.25)$$

where D is the diffusion coefficient for the alkali-metal atoms.

- Alkali-metal-alkali-metal spin-rotation collisions with potential

$$V_{AA} = (3/2)\lambda(3S_\zeta S_\zeta - 2):$$

$$\frac{d\rho}{dt} = -\frac{1}{T_{AA}}\rho_S \quad \text{and} \quad \frac{1}{T_{AA}} = [A]\langle\sigma_{AA}\nu\rangle. \quad (4.26)$$

- Alkali-metal-alkali-metal binary spin-exchange collisions $V_{\text{ex}} = J\mathbf{S}_i \cdot \mathbf{S}_j$:

$$\frac{d\rho}{dt} = -\frac{1}{T_{\text{ex}}}\rho_S + \frac{1}{T_{\text{ex}}}4\langle\mathbf{S}\rangle \cdot \mathbf{S}\rho_{\bar{S}} \quad \text{and} \quad \frac{1}{T_{\text{ex}}} = [A]\langle\sigma_{\text{ex}}\nu\rangle. \quad (4.27)$$

- Alkali-metal-buffer gas spin-rotation collision $V_{\text{bsr}} = \gamma_{\text{bsr}}\mathbf{N} \cdot \mathbf{S}$:

$$\frac{d\rho}{dt} = -\frac{1}{T_{\text{bsr}}}\rho_S \quad \text{where} \quad \frac{1}{T_{\text{bsr}}} = [Y]\langle\sigma_{\text{bsr}}\nu\rangle. \quad (4.28)$$

- Alkali-metal-noble gas spin-rotation collision $V_{NS} = \gamma_{NS}\mathbf{N} \cdot \mathbf{S}$:

$$\frac{d\rho}{dt} = -\frac{1}{T_{NS}}\rho_S \quad \text{where} \quad \frac{1}{T_{NS}} = [\text{Xe}]\langle\sigma_{NS}\nu\rangle. \quad (4.29)$$

- Alkali-metal-noble gas binary spin-exchange collision $V_{KS} = \alpha_{KS} \mathbf{K} \cdot \mathbf{S}$:

$$\frac{d\rho}{dt} = -\frac{\eta_K}{T_{KS}} \rho_S + \frac{\eta_K}{T_{KS}} 4 \langle \mathbf{K} \rangle \cdot \mathbf{S} \rho_{\bar{S}}, \quad (4.30)$$

where \mathbf{K} is the noble gas nuclear spin, η_K is the isotopic fraction of noble gas ($\eta_{129} = 0.264$) and $1/T_{KS} = [\text{Xe}] \langle \sigma_{KS} \nu \rangle$.

- Alkali-metal-noble gas spin-rotation interaction during molecule formation

$$V_{mNS} = \gamma_{mNS} \mathbf{N} \cdot \mathbf{S}:$$

$$\frac{d\rho}{dt} = -\frac{1}{T_{vW}} \left(\frac{2\phi_\gamma^2}{3} \right) f_S \rho_S - \frac{1}{T_{vW}} \left(\frac{2\phi_\gamma^2}{3} \right) \frac{f_F}{(2I+1)^2} (\mathbf{F} \cdot \mathbf{F} \rho - \mathbf{F} \cdot \rho \mathbf{F}), \quad (4.31)$$

where $\phi_\gamma = \frac{\gamma_{mNS} N \tau_c}{\hbar}$ is the rms precession angle of alkali-metal electron spin around the molecular spin and $\frac{1}{T_{vW}}$ is the molecular formation rate, in the ‘short lifetime’ regime $\phi_\gamma = \omega_\gamma \tau_c$ and in the ‘long lifetime’ regime $\phi_\gamma = \frac{\omega_\gamma}{2I+1} \tau_c$, with τ_c being the correlation time which is equal to molecular lifetime under certain conditions [13].

- Alkali-metal-noble gas spin-exchange collision during molecule formation

$$V_{mKS} = \alpha_{mKS} \mathbf{K} \cdot \mathbf{S}:$$

$$\begin{aligned} \frac{d\rho}{dt} = & -\frac{1}{T_{\text{vW}}} \left(\frac{\phi_\alpha^2}{2} \right) \eta_K f_S \rho_S - \frac{1}{T_{\text{vW}}} \left(\frac{\phi_\alpha^2}{2} \right) \eta_K \frac{f_F}{(2I+1)^2} (\mathbf{F} \cdot \mathbf{F} \rho - \mathbf{F} \cdot \rho \mathbf{F}) \\ & + \frac{1}{T_{\text{vW}}} \left(\frac{\phi_\alpha^2}{2} \right) \eta_K f_S (4 \langle \mathbf{K} \rangle \cdot \mathbf{S}) \rho_S \\ & + \frac{1}{T_{\text{vW}}} \left(\frac{\phi_\alpha^2}{2} \right) \eta_K \frac{f_F}{(2I+1)^2} [\langle \mathbf{K} \rangle \cdot (\mathbf{F} \rho + \rho \mathbf{F} - 2i \mathbf{F} \times \rho \mathbf{F})], \end{aligned} \quad (4.32)$$

where $\phi_\alpha = \frac{\alpha_{mKS} \tau_c}{h}$ is the rms precession angle evolution for the van der Waals molecules.

f_S is the fraction of molecules with a ‘very short lifetime’ [13]

$$f_S = \frac{1}{1 + (\omega_{\text{HF}} \tau)^2} = \frac{1}{1 + (\omega_{\text{HF}} C / [G])^2} \quad (4.33)$$

and

$$\begin{aligned} f_F = & \frac{1}{1 + (\omega_\gamma \tau / 2I + 1)^2} - \frac{1}{1 + (\omega_{\text{HF}} \tau_c)^2} \\ = & \frac{1}{1 + (\omega_\gamma C / (2I + 1) [G])^2} - \frac{1}{1 + (\omega_{\text{HF}} C / [G])^2} \end{aligned} \quad (4.34)$$

is the fraction of molecules with a ‘short lifetime’. Here $\tau = \frac{C}{[G]}$ where C is the proportionality constant which has units of ‘amagat.s’ ($1 \text{ amagat} = 2.69 \times 10^{19} \text{ cm}^{-3}$) and can be defined as the molecular breakup rate coefficient $C = 1 / \langle \sigma_B \nu \rangle$ and $[G]$

is the total gas density. The effect of spin-rotation interactions always decreases $\langle \rho \rangle$ through the ρ_s part, as the negative sign in the differential equations indicates. On the other hand, the spin-exchange terms are divided into two parts: one part is those interactions that transfer polarization out of the alkali-metal atom, which acts like the spin-rotation terms, and the other part is those interactions that transfer polarization into the alkali-metal atom known as back polarization. Based on whether the correlation times of the damping terms stated above are shorter or longer than the hyperfine period $\tau_{\text{HF}} = \frac{\hbar}{A\mathbf{I}\cdot\mathbf{S}}$, they can be classified as S-damping or F-damping terms. An F-damping term's correlation time is equal to or larger than the τ_{HF} , indicating that \mathbf{I} and \mathbf{S} are well connected. As a result, an F-damping perturbation can only cause transitions within the same manifold when F is conserved in magnitude, i.e., when $\Delta m = \pm 1$ and $\Delta F = 0$. On the other hand, because an S-damping term's correlation time is much shorter than the τ_{HF} , \mathbf{I} and \mathbf{S} can be thought of as being uncoupled during the brief interaction. The S-damping perturbation can cause transitions from one manifold to another without conserving F , i.e., $\Delta m = \pm 1$ and $\Delta F = \pm 1$. The total time evolution of the density matrix will be the sum of all the above terms [13]

$$\begin{aligned}
\frac{d\rho}{dt} = & \frac{1}{i\hbar}[H, \rho] + (-R\rho_s + 2R\mathbf{s} \cdot \mathbf{S}\rho_{\bar{s}}) + D\Delta^2\rho - \frac{1}{T_{\text{ex}}}\rho_s \\
& + \frac{1}{T_{\text{ex}}}4\langle \mathbf{S} \rangle \cdot \mathbf{S}\rho_{\bar{s}} - \frac{1}{T_{\text{sd}}}\rho_s - \frac{1}{(2I+1)^2 T_{\text{fd}}}(\mathbf{F} \cdot \mathbf{F}\rho - \mathbf{F} \cdot \rho\mathbf{F}) \\
& + \frac{1}{T_{\text{se}}}4\langle \mathbf{K} \rangle \cdot \mathbf{S}\rho_{\bar{s}} + \frac{1}{(2I+1)^2 T_{\text{fe}}}[\langle \mathbf{K} \rangle \cdot (\mathbf{F}\rho + \rho\mathbf{F} - 2i\mathbf{F} \times \rho\mathbf{F})]
\end{aligned} \tag{4.35}$$

where $\frac{1}{T_{\text{ex}}}$ is the alkali-metal-alkali-metal spin-exchange rate, $\frac{1}{T_{\text{sd}}}$ is the sum of all S-damping rates, $\frac{1}{T_{\text{fd}}}$ is the sum of all F-damping rates, $\frac{1}{T_{\text{se}}}$ is the sum of all the spin-exchange rates between alkali-metal and noble gas atoms with lifetime much faster than the hyperfine period and $\frac{1}{T_{\text{fe}}}$ is the sum of all spin-exchange rates between alkali-metal and noble gas atoms with lifetime in the order of or longer than the hyperfine period. Eq. 4.35 under certain conditions have a simpler form. We can omit the optical pumping term for the ‘relaxation in the dark’ measurement. In the case of the ‘Pulsed-EPR’ experiment, where we don’t have any RF field and at low polarization, the density matrix is longitudinal, and the Hamiltonian has no direct effect on the relaxation so we can neglect the first term in Eq. 4.35 [62]. Since we are interested in the low polarization part, we make sure that we don’t keep the pumping light on long enough for nuclear polarization build-up so we can omit the terms proportional to $\langle \mathbf{K} \rangle$ as well [62]. In our case, the diffusion term is small enough to be neglected [13]. These simplifications result in a more compact form of Eq. 4.35

$$\frac{d\rho}{dt} = -\frac{1}{T_{\text{ex}}} (\rho_S - 4\langle \mathbf{S} \rangle \cdot \mathbf{S} \rho_{\bar{S}}) - \frac{1}{T_{\text{sd}}} \rho_S - \frac{1}{(2I+1)^2 T_{\text{fd}}} (\mathbf{F} \cdot \mathbf{F} \rho - \mathbf{F} \cdot \rho \mathbf{F}) \quad (4.36)$$

So, one can say, in general, under the defined conditions and simplifications, the time evolution of the density matrix is affected by three processes [13]

$$\frac{d\rho}{dt} = \left(\frac{d\rho}{dt} \right)_{\text{ex}} + \left(\frac{d\rho}{dt} \right)_{\text{sd}} + \left(\frac{d\rho}{dt} \right)_{\text{fd}} \quad (4.37)$$

Now that we have the rate equation of the density matrix, it is straightforward to get the time evolution of $\langle a_z \rangle$ and $\langle b_z \rangle$ based on Eq. 4.16 and different terms of Eq. 4.37

$$\begin{aligned} \frac{d\langle a_z \rangle}{dt} &= \text{Tr} \left(a_z \frac{d\rho}{dt} \right) \\ &= \text{Tr} \left(a_z \left(\frac{d\rho}{dt} \right)_{\text{ex}} \right) + \text{Tr} \left(a_z \left(\frac{d\rho}{dt} \right)_{\text{sd}} \right) + \text{Tr} \left(a_z \left(\frac{d\rho}{dt} \right)_{\text{fd}} \right) \end{aligned} \quad (4.38)$$

and the same differential equation holds for $\langle b_z \rangle$ as well

$$\begin{aligned} \frac{d\langle b_z \rangle}{dt} &= \text{Tr} \left(b_z \frac{d\rho}{dt} \right) \\ &= \text{Tr} \left(b_z \left(\frac{d\rho}{dt} \right)_{\text{ex}} \right) + \text{Tr} \left(b_z \left(\frac{d\rho}{dt} \right)_{\text{sd}} \right) + \text{Tr} \left(b_z \left(\frac{d\rho}{dt} \right)_{\text{fd}} \right) \end{aligned} \quad (4.39)$$

Considering Eqs. 4.38 and 4.39 and referring to Eq. 4.19 we can rewrite $\tilde{\Gamma}$ as

$$\tilde{\Gamma} = \tilde{\Gamma}_{\text{ex}} + \tilde{\Gamma}_{\text{sd}} + \tilde{\Gamma}_{\text{fd}} \quad (4.40)$$

By substituting different terms of Eq. 4.37 in Eqs. 4.38 and 4.39 and simplifying

them, one can get each term of Eq. 4.40[62]

$$\begin{aligned}
\tilde{\Gamma}_{\text{ex}} &= \frac{1}{3[I]^2 T_{\text{ex}}} \begin{pmatrix} [I]^2 - 3[I] + 2 & -[I]^2 - 3[I] - 2 \\ -[I]^2 + 3[I] - 2 & [I]^2 + 3[I] + 2 \end{pmatrix} \\
\tilde{\Gamma}_{\text{sd}} &= \frac{1}{2[I]^2 T_{\text{sd}}} \begin{pmatrix} [I]^2 - [I] + 2 & -[I]^2 - 3[I] - 2 \\ -[I]^2 + 3[I] - 2 & [I]^2 + [I] + 2 \end{pmatrix} \\
\tilde{\Gamma}_{\text{fd}} &= \frac{1}{[I]^2 T_{\text{fd}}} \begin{pmatrix} 1 & 0 \\ 0 & 1 \end{pmatrix}
\end{aligned} \tag{4.41}$$

We can get the same results using a qualitative approach. Taking into account only the dominant processes of alkali-metal-noble gas binary collisions and alkali-metal-noble gas van der Waals molecule formation we can write the differential equation of $\langle F_z \rangle$ as

$$\frac{d\langle F_z \rangle}{dt} = -\frac{1}{T_{\text{sd}}} \langle S_z \rangle - \frac{1}{T_{\text{fd}}} \frac{\eta_{\text{A}}}{[I]^2} \langle F_z \rangle \tag{4.42}$$

where $[I] = (2I + 1)$ and the S-damping and F-damping rates are:

$$1/T_{\text{sd}} = \Gamma_{\text{bin}} + \eta_{\text{A}} f_{\text{S}} \Gamma_{\text{vW}} \quad , \quad 1/T_{\text{fd}} = f_{\text{F}} \Gamma_{\text{vW}}, \tag{4.43}$$

where $\Gamma_{\text{bin}} = [\text{Xe}]\langle\sigma_{\text{bin}}\nu\rangle$, and

$$\begin{aligned}\Gamma_{\text{vW}} &= \frac{1}{T_{\text{vW}}} \left(\eta_K \frac{\phi_\alpha^2}{2} + \frac{2\phi_\gamma^2}{3} \right) = \frac{\kappa[\text{Xe}]}{\tau} \left(\frac{\eta_K}{2} \left(\frac{\alpha\tau}{\hbar} \right)^2 + \frac{2}{3} \left(\frac{\gamma N\tau}{\hbar} \right)^2 \right) \\ &= \frac{\kappa r[G]}{\tau} \tau^2 \left(\frac{\eta_K}{2} \left(\frac{\alpha}{\hbar} \right)^2 + \frac{2}{3} \left(\frac{\gamma N}{\hbar} \right)^2 \right) = \kappa r C \left(\frac{\eta_K}{2x^2} + \frac{2}{3} \right) \omega_\gamma^2\end{aligned}\quad (4.44)$$

Γ_{vW} is the ‘very short‘ lifetime molecular contribution to alkali-metal spin-relaxation, $1/T_{\text{vW}}$ is the molecular formation rate, and $x = \gamma N/\alpha$. Γ_{vW} is a density-independent quantity [34], and it only depends on κ the chemical equilibrium coefficient, C the proportionality coefficient, r the Xe fraction in the total gas density $[\text{Xe}] = r[G]$ (in our experiment $r = 3\%$) and ω_γ . Knowing the differential equation for $\langle F_z \rangle$ and based on the relation between $\langle F_z \rangle$ and $\langle S_z \rangle$ one can get the differential equation for $\langle S_z \rangle$ and solve it for the low polarization limit

$$\lim_{\langle S_z \rangle \rightarrow 0} \frac{d\langle S_z \rangle}{dt} = -\gamma_A \langle S_z \rangle \quad (4.45)$$

where the slowest decay rate, associated with electron-randomization, is

$$\begin{aligned}\gamma_A &= \frac{\Gamma_{\text{bin}}}{1 + \bar{\epsilon}} + \sum_i \left(\eta_i f_{S,i} + f_{F,i} \frac{\eta_i (1 + \epsilon_i)}{(2I_i + 1)^2} \right) \frac{\Gamma_{\text{vW}}}{1 + \bar{\epsilon}} \\ &+ A \frac{\Gamma_{\text{bin}}^2}{\Gamma_{\text{ex}}} + B \frac{\Gamma_{\text{bin}} \Gamma_{\text{vW}}}{\Gamma_{\text{ex}}} + E \frac{\Gamma_{\text{vW}}^2}{\Gamma_{\text{ex}}}\end{aligned}\quad (4.46)$$

where this is the general form that applies to both mono-isotopic and poly-isotopic

alkali-metal atoms, with i accounting for different isotopes. In Eq. 4.46, $\bar{\epsilon} = \sum_i (\eta_i \epsilon_i)$ and the last three terms are first-order corrections that account for small deviation from the spin temperature limit. The parameters A , B and E are functions of $f_{S,i}$ and $f_{F,i}$ determined by the perturbation theory described in [62].

4.3 Experimental Setup and Procedure

We performed our measurements on two sets of four 1-inch-diameter spherical Pyrex cells; one set included a few milligrams of Rb, and the other set contained a few milligrams of Cs metal to analyze Rb and Cs spin-relaxation under comparable conditions. We aimed for four different total gas pressures for both sets of cells, 1.5, 2, 2.5, and 3 amagats, with a fixed gas composition of 94% ^4He , 3% N_2 and 3% enriched ^{129}Xe . Table 4.1 shows a complete description of our cells.

Cell	Volume (cm ³)	^4He (torr)	N_2 (torr)	Xe (torr)	Total (torr)
309A (Rb)	5.6	1149.2	36.8	34.2	1220.1
309B (Rb)	5.3	1534.2	49.6	49.1	1632.8
309C (Rb)	5.5	1918.9	57.0	64.1	2040.0
309D (Rb)	6.1	2294.7	73.3	72.2	2440.2
310A (Cs)	6.3	1143.6	36.6	31.0	1211.2
310B (Cs)	6.4	1523.4	49.0	49.3	1621.6
310C (Cs)	6.3	1856.2	62.6	62.0	1980.8
310D (Cs)	6.5	2294.4	73.7	74.7	2442.8

Table 4.1: Volume and gas pressures of the eight cells, gas pressures are measured at room temperature $\sim 20^\circ \text{C}$. Xe gas we used in our cells is enriched to 90% ^{129}Xe . The errors on the pressures and cell volumes are $\sim 4 - 5\%$ and $\sim 2\%$, respectively.

We do a relaxation in the dark measurement using the pulsed EPR technique. In

this method, the cell is placed in the temperature-controlled oven. The oven temperature was maintained at 130° C, and it was measured by a resistive thermometric device (RTD) affixed right below the cell. The oven was centered between two 24-inch-diameter coils, having Helmholtz configuration and producing a static magnetic field $B_1 \sim 28$ G. A specially designed circuit provided the stability of the static field to control and stabilize the current through the coils, the details of which can be found in [51], enabling us to stabilize the static field to at least a part in 10^5 . To optically pump the sample, we used 40-W diode laser arrays (models M1B15-790-SS4.1 and M1B-892.2-60C-SS4.3 from DILAS for Rb and Cs, respectively). The pump lasers were tuned to Rb and Cs D_1 resonances, and they were narrowed to ~ 0.3 nm with an external Littrow cavity. We used a 1/4 wave plate to make the linearly polarized pump laser beam circularly polarized. We did an optical detection of the alkali-metal polarization based on Faraday rotation using 120-mW lasers (models L785P090 and L850P100 from Thorlabs for Rb and Cs, respectively) narrowed to ~ 0.3 nm. The probe lasers were ≈ 0.6 nm detuned from the D_2 resonances to avoid absorption of the beam, big Faraday rotations, and their effect on the shape of the resonance peaks so that we were able to measure the areas under the peaks accurately. We used a linearly polarized probe beam, propagating transverse to the applied magnetic field. On its way, it passed through a 1/2 wave plate, the cell, a focusing lens, and a polarizing beam splitter cube and got detected by a set of balance photodiodes (model

PDB415A from Thorlabs). The pulsed EPR experiment was done using the Redstone TNMR spectrometer (Tecmag). Using the Tecmag we generated the EPR excitation pulses at the alkali-metal Larmor frequency, Fig. 4.2 shows the sample pulse sequence we programmed in TNMR software. The Tecmag is also the receiver, and it receives the subsequent optically detected FID signals from the photodetectors.

Tecmag, combined with the TNMR software, is a sophisticated setup enabling us to generate pulses with a specific amplitude, frequency, and pulse width. We amplified the RF pulses using the power amplifier (model BT02000-AlphaSA from Tomco) and sent the pulses to the tuned and matched EPR coil. We made sure that the oscillating magnetic field B_1 that these pulses generated was small enough so that the spins were flipped by a small angle $< 10^\circ$, resulting in a small Faraday rotation of the probe beam. To figure out the strength of the B_1 field at a fixed pulse amplitude, we sent pulses with different pulse widths starting from the smallest value and then increased the pulse width until we saw a symmetric spectrum (Fig. 4.3), indicating that the flip angle is 90° and we have done a $\pi/2$ pulse. Then, using the relation

$$\theta = \gamma B_1 t \tag{4.47}$$

where γ is the alkali-metal gyromagnetic ratio, and t is the pulse width; we calculated the strength of B_1 at that fixed pulse amplitude and then for this B_1 strength and amplitude using the Eq. 4.47, we calculate the pulse width that corresponds to a

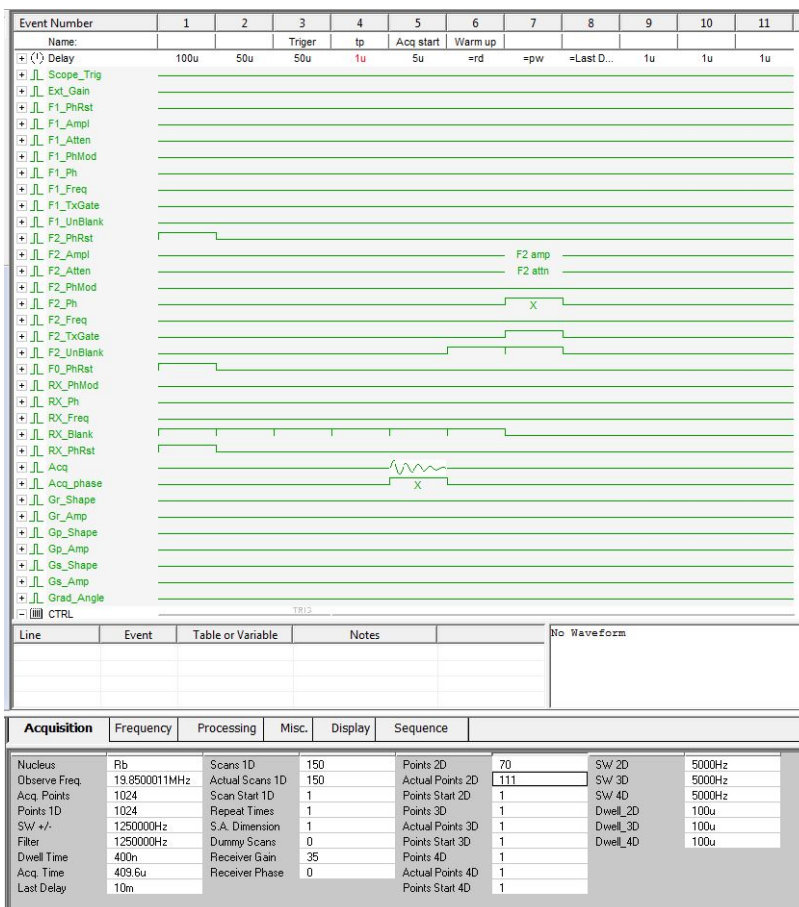


Figure 4.2: Sample pulse sequence for Rb. The sequence starts with a fixed delay of $\sim 150 \mu\text{s}$ (columns 1 and 2) as a warm-up time for Tecmag. Next, the delay table for the chopper (column 3) starts. The Tecmag receives the trigger from the chopper and will continue the pulse sequence based on the delay table entries ($1000 \mu\text{s}$ - $8000 \mu\text{s}$ in the case of Rb and $1000 \mu\text{s}$ - $12000 \mu\text{s}$ in the case of Cs with step size $100 \mu\text{s}$). After the delay time, the receiver window opens (column 5), since we do optical detection, the detection part is decoupled from the RF excitation allowing us to open the detection window even before the pulse comes. Then the pulse with a specific pulse width and amplitude is sent to the RF amplifier and then the corresponding FID signal is received from the photodetector. This sequence repeats based on the number of scans and the entries of the delay table for the chopper.

small flip angle below $< 10^\circ$. Table 4.2 shows typical pulses for Rb and Cs.

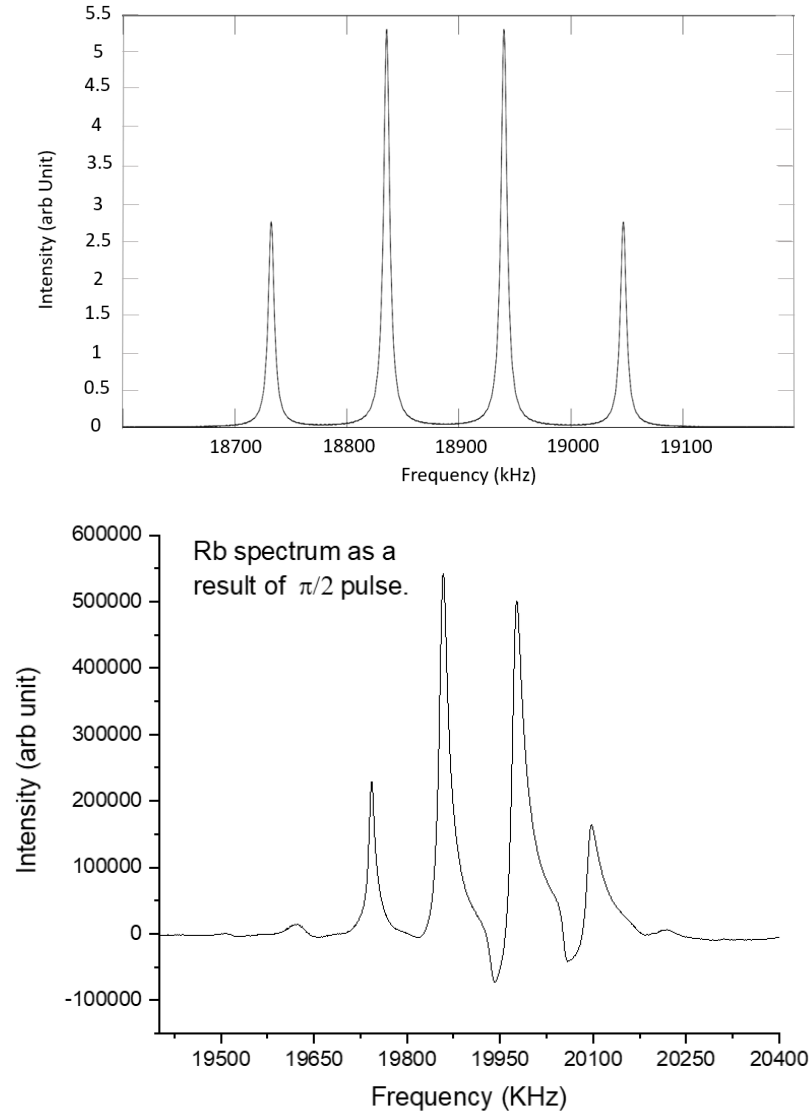


Figure 4.3: Rb spectrum after applying a $\pi/2$ pulse. The top figure is from a simulation being done in MatLab, and the bottom figure is an experimental Rb spectrum after applying a $\pi/2$ pulse.

For the relaxation in the dark measurement, we used an optical chopper running at 40 Hz with a 50% duty cycle, with alternating 12.5 ms light and dark periods.

Alkali-metal	Pulse Width (ns)	B_1 (G)	Frequency (MHz)
Rb	500	0.2	19.8
Cs	300	0.2	9.9

Table 4.2: The RF pulse configuration for different alkali-metals in the relaxation in the dark measurement.

Whenever the chopper sensed the start of a dark time period region, it sent a TTL pulse to the Tecmag, triggering it to start the pulse and acquisition sequence. The sequence was programmed in a way that the trigger started the procedure with progressively increasing delay time of step size $100 \mu\text{s}$. Fig. 4.4 shows the experimental setup of our relaxation in the dark measurement using pulsed EPR.

Using the TNMR software, a Fast Fourier Transform FFT was done on the FID signals received from the Tecmag. In total, for Rb, we took a total of 70 FIDs, each corresponding to a gradually extending delay time in the dark (Fig. 4.5), and in the case of Cs we took 110 FIDs to cover the Cs' slower decay (Fig. 4.6).

Each FID was a result of 150 scans and adjusted gain in order to boost SNR (Fig. 4.7). This procedure was done on three different days, and the final rate was reported as the average of these three days' measurements.

To get the alkali-metal polarization decay vs. time, we acquired all the EPR spectra corresponding to each delay in the dark. Based on the orientation of the EPR coil with respect to the static magnetic field, which was transverse to the static magnetic field, there was a 180° phase difference between the upper manifold $F = 2$ resonance peaks and the lower manifold $F = 1$ resonance peaks, helping us to integrate

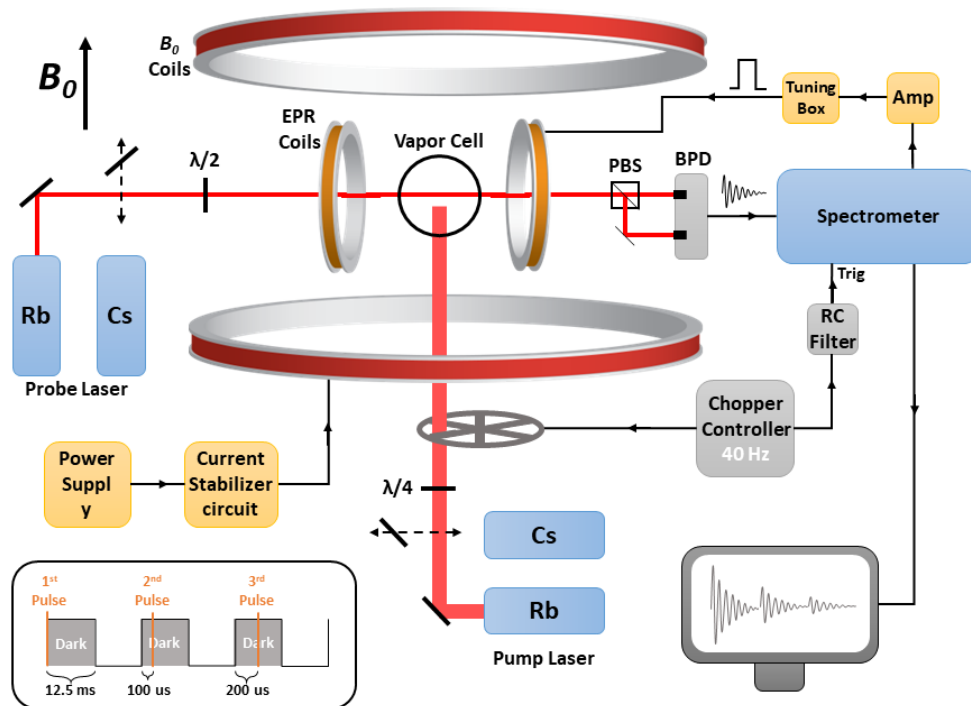


Figure 4.4: The relaxation in the dark measurement using pulsed EPR. The optical chopper runs at 40 Hz and triggers the Tecmag by sending a TTL pulse to start the pulse sequence. Tecmag sends the RF pulse to the Tomco amplifier to get amplified, and after amplification, it is sent to the EPR coil to generate the oscillating magnetic field that will excite the spins. Larmore precession of the spins is detected via Faraday rotation of the probe beam through the balanced photodetectors and is sent to Tecmag. We process the FID signals using TNMR software.

the areas under the upper manifold resonance peaks for all the spectra and knowing the fact that the area under these resonance peaks is proportional to the alkali-metal polarization we were able to use the integrated areas and plot them vs. the delay times in order to replicate the polarization decay and get the relaxation rate from it, Fig. 4.8 shows samples of Rb and Cs polarization decay.

In order to get the slowest decay rate, which is the fundamental electron spin-

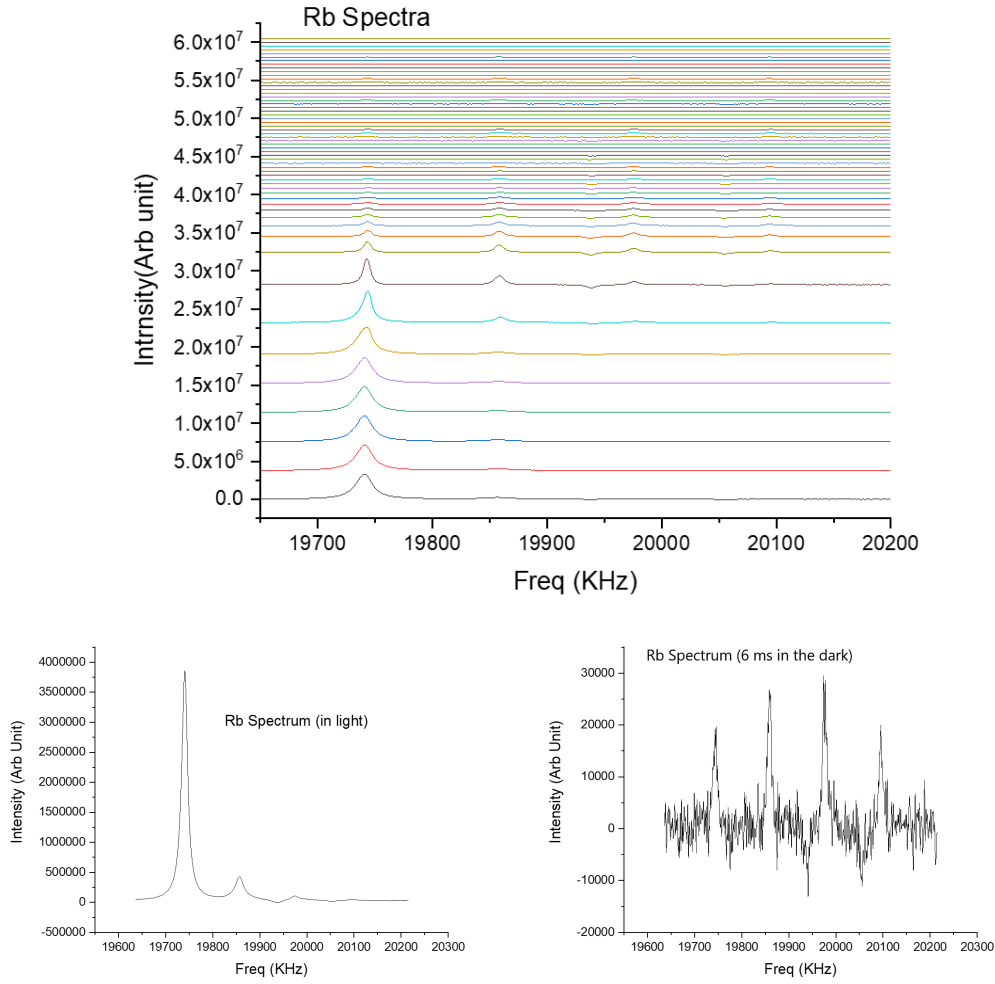


Figure 4.5: The figure on the top shows all the 70 Rb spectra as a result of relaxation in the dark measurement using the optical chopper to detect the Rb polarization decay in the course of time. The bottom left figure is the first spectrum, which was taken in the light, and the bottom right figure is the spectrum corresponding to ~ 6 ms delay time in the dark.

relaxation rate γ_A from the multiexponential relaxation transient (Fig. 4.8), we fitted the transient from its initial point to single exponential decay and recorded the decay time constant and its associated error. This procedure was done repeatedly while progressively excluding data points from the start of the transient and changing the

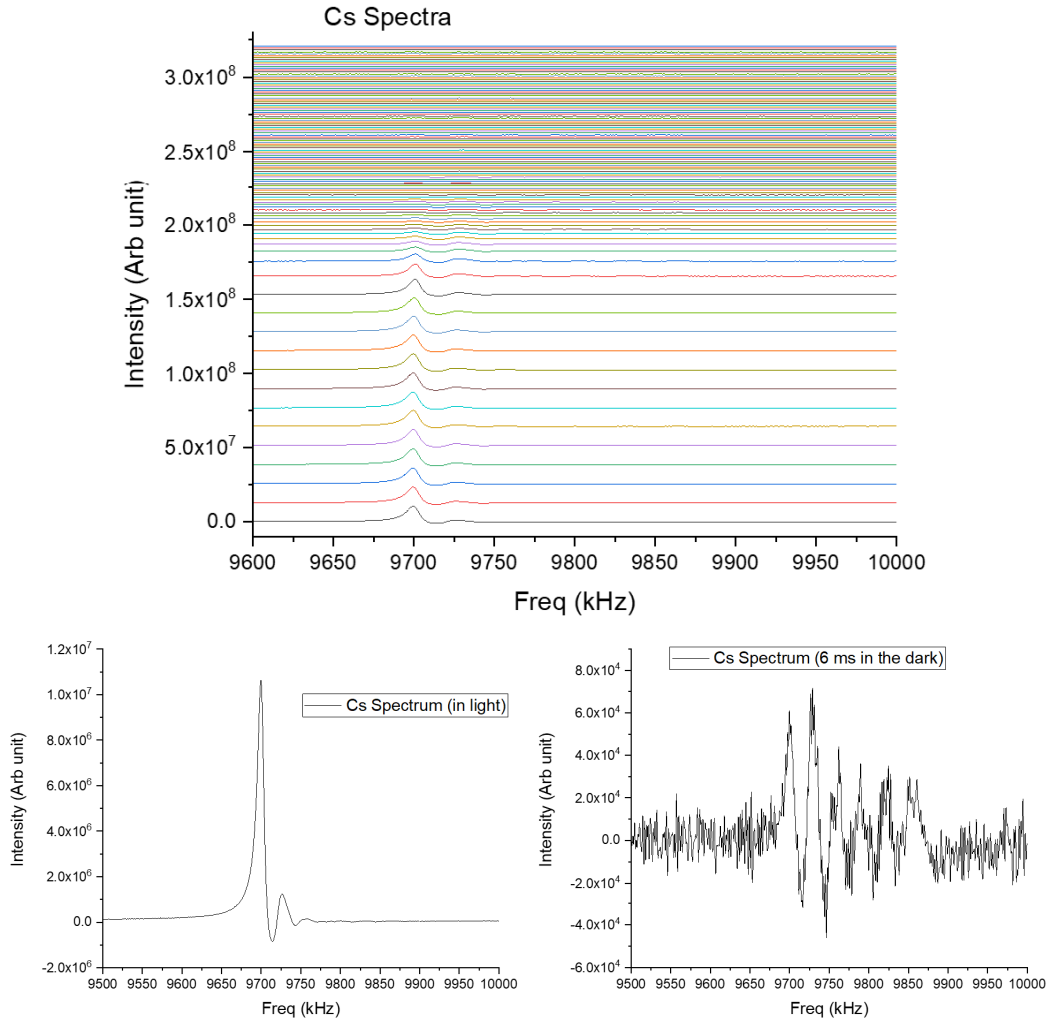


Figure 4.6: The figure on the top shows all the 110 Cs spectra as a result of relaxation in the dark measurement using the optical chopper to detect the Cs polarization decay in the course of time. The bottom left figure is the first spectrum, which was taken in the light, and the bottom right figure is the spectrum corresponding to ~ 6 ms delay time in the dark.

initial point of the fitting until the extracted time constant reached a plateau with a reasonable error of 1-6%, Fig. 4.9 shows samples of decay transient and fitting procedure for both Rb and Cs.

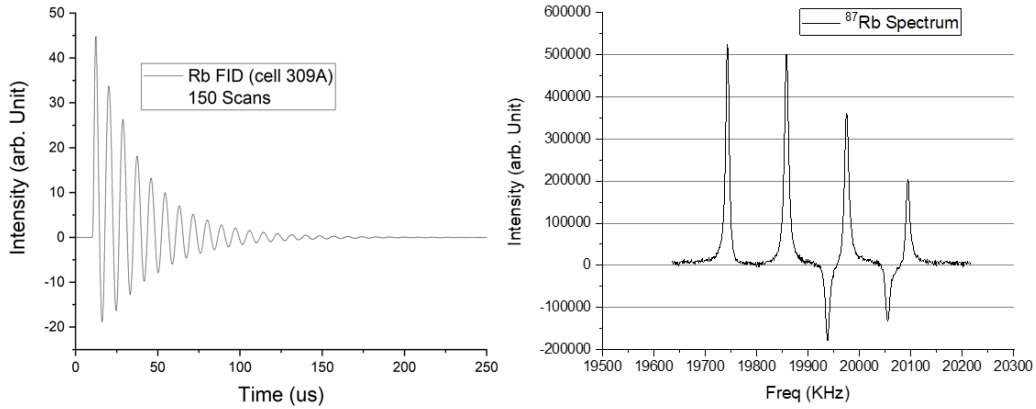


Figure 4.7: Sample FID for Rb, this FID was taken while the pump laser was on.

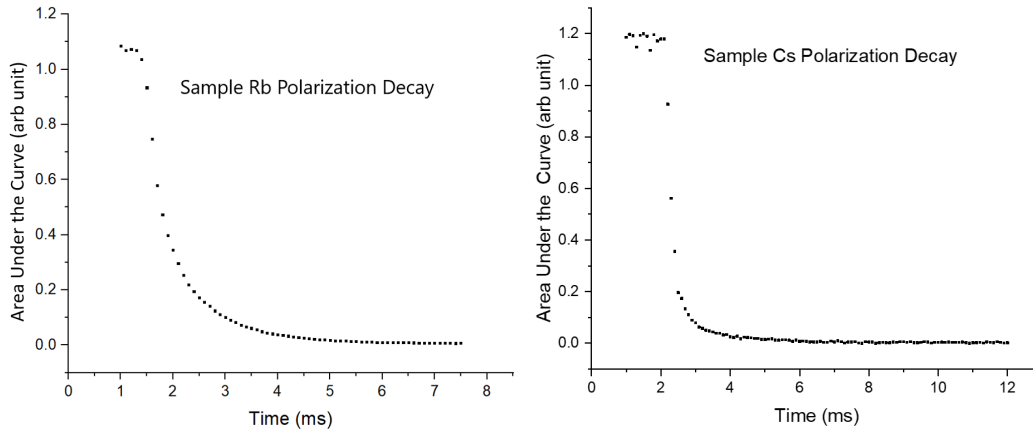


Figure 4.8: Plot of the area under the resonance peaks vs. time for Rb (left) and Cs (right) based on the spectra taken from the measurements in the dark.

4.4 Results and Analysis

Table 4.3 shows the measured spin-destruction rate γ_A with its error for Rb and Cs, and Fig. 4.10 is the plot of the measured spin-destruction rate vs. total gas density.

By looking at values of γ_A for Rb and Cs and comparing them, one can see that

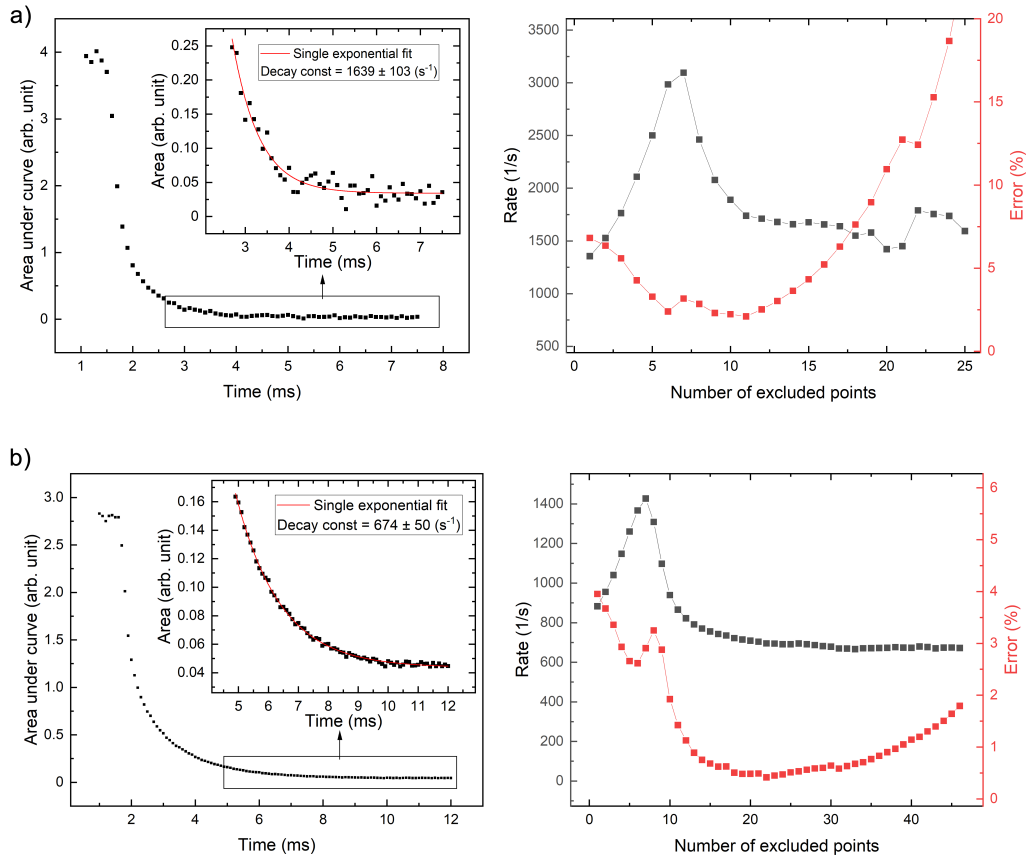


Figure 4.9: Sample Rb (a) and Cs (b) polarization decay and single exponential fitting procedure to get the electron spin-relaxation rate γ_A . The figures on the left show the sample decay transient, and the figures on the right show the fitting procedure of fitting the transient with single exponential decay while eliminating points from the beginning of the transient until the time constant of the single exponential decay stays unchanged within its error.

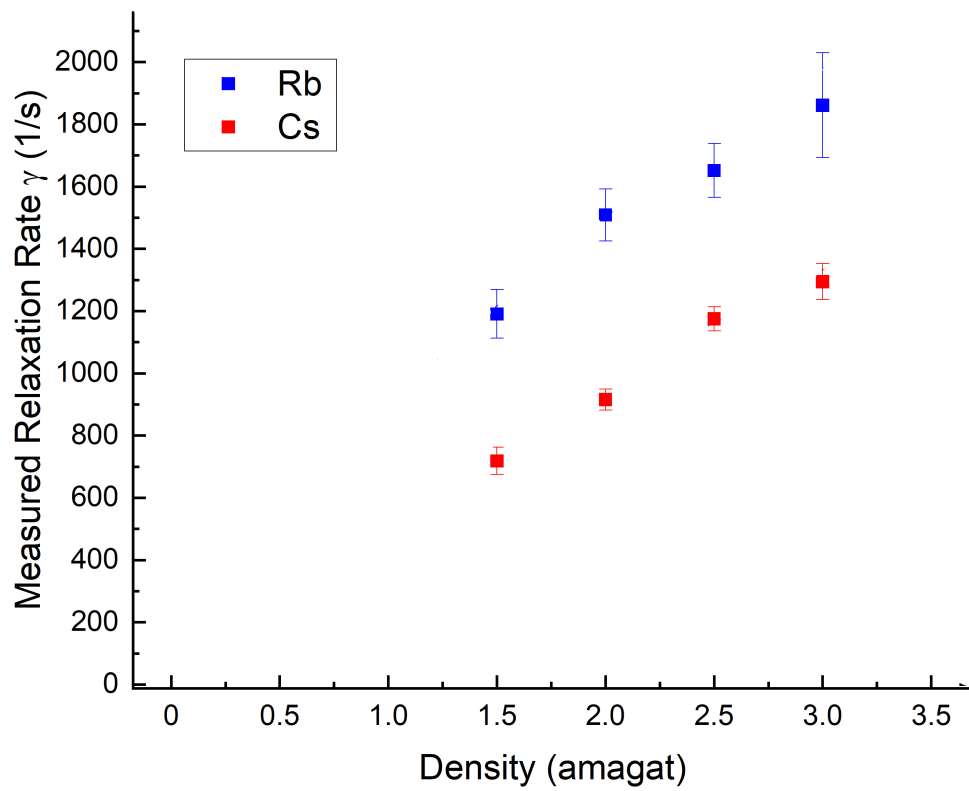


Figure 4.10: Rb and Cs measured spin-relaxation rate γ_A vs. total gas density.

Cell	Total gas density (amagat)	γ_A (1/s)	Γ_A (1/s)
309A (Rb)	1.50	1170±80	12636±864
309B (Rb)	2.00	1504±86	16243±928
309C (Rb)	2.51	1657±105	17895±1134
309D (Rb)	2.99	1865±200	20142±2160
310A (Cs)	1.49	678±45	14916±990
310B (Cs)	1.99	899±35	19778±704
310C (Cs)	2.48	1131±42	24882±924
310D (Cs)	3.00	1238±68	27236±1496

Table 4.3: Values of measured spin-destruction rate γ_A , which comes from the single exponential decay fit of the alkali-metal polarization decay and electron-randomization Γ_A values which are related to γ_A through the paramagnetic coefficient $\Gamma_A = (1 + \bar{\epsilon}) \gamma_A$.

γ_{Cs} is about 30 to 50% smaller than γ_{Rb} over the range of density and the specific temperature 130° C that we performed our experiment. In order to exclude any temperature effect on measurements, we performed the same spin-destruction measurement at two other temperatures 110° C and 150° C on the cells 309A containing Rb and 310A containing Cs with fixed total gas density, the results are shown in table 4.4 and Fig. 4.11.

Temperature(° C)	γ_{Rb} (1/s)	γ_{Cs} (1/s)
110	980±100	642±43
130	1170±80	678±45
150	1181±91	742±52

Table 4.4: Values of measured spin-destruction rate γ_A , for cells 309A and 310A with the fixed total density of ~ 1.5 amagat containing Rb and Cs respectively, at three different temperatures to understand the effect of temperature on the spin-relaxation rate of the alkali-metal atoms.

One can see from the table and figure that no matter what the temperature is for

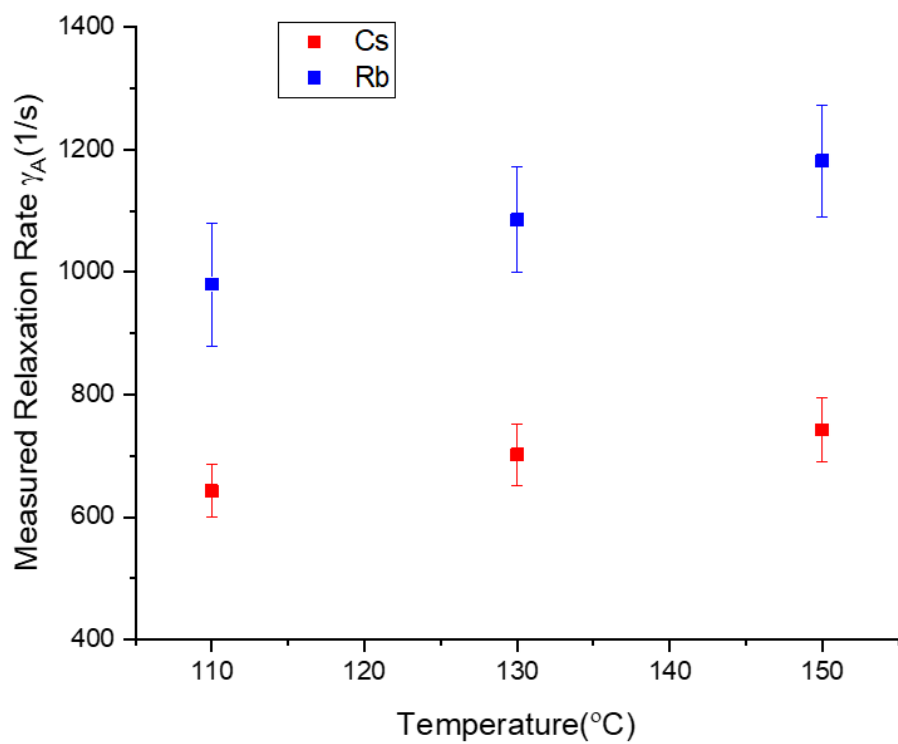


Figure 4.11: Rb and Cs measured relaxation rate γ_A vs. temperature.

fixed gas density and gas composition, γ_{Cs} is smaller than γ_{Rb} with no overlapping of their associated error bars. This observation led us to conclude that this difference between spin-destruction rates is not due to temperature or alkali-metal vapor density, and this observed discrepancy is due to a more fundamental difference between Rb and Cs atoms.

The electron-randomization rate, Γ_{A} can be calculated using the measured relaxation rate and the paramagnetic coefficient. In the case of Rb, because of its poly-isotopic nature $\Gamma_{\text{Rb}} = (1 + \bar{\epsilon}) \gamma_{\text{Rb}}$, with $\bar{\epsilon} = \sum_i \eta_i \epsilon_i$, and for mono-isotopic Cs $\Gamma_{\text{Cs}} = (\epsilon + 1) \gamma_{\text{Cs}}$. The values of ϵ and η are given in table 4.5 and the values of Γ_{A} are given in table 4.3 along with the values of γ_{A} . It is insightful to plot Γ_{A} vs. total gas density, as it can be observed from Fig. 4.12 and values of Γ_{A} in table 4.3 over the studied range of density the electron-randomization for Rb, is $\sim 30\%$ smaller than electron-randomization for Cs, which is due to the effect of the paramagnetic coefficient, also known as the slowing down factor $\epsilon = 1 + \bar{\epsilon}$, which indicates that the measured alkali-metal relaxation rate is slowed down because of the hyperfine coupling of alkali-metal electron with its nuclear spin.

To test our work and make sure that our experimental results match the theoretical results, we utilized Nelson and Walker's theoretical model [34]. In their model, we replaced all the dependent variables with their expressions in terms of $[G]$, the total gas density, and obtained Eq. 4.46. We substituted the constants with the values

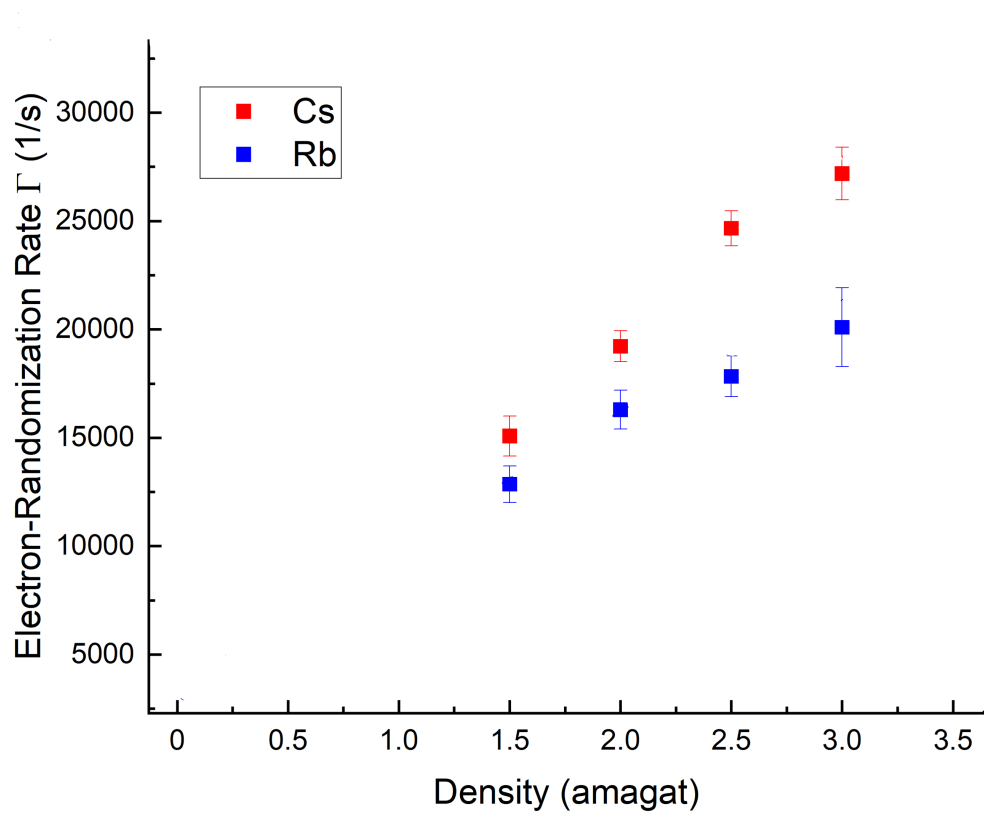


Figure 4.12: Rb and Cs electron-randomization rate Γ_A vs. total density.

given in the table 4.5 and left $[G]$ to be the independent variable. Then, we made the required adjustments to the parameters that were specific to the gas composition, temperature, and the respective alkali-metals.

Constant	Unit	Rb	Cs
ω_{HF}	(rad/s)	$\omega_{HF85} = 1.91 \times 10^{10}$ & $\omega_{HF87} = 4.29 \times 10^{10}$	5.78×10^{10}
ω_{sr}	(rad/s)	8.48×10^8	9.42×10^8
ϵ		$\epsilon_{85} = 11.67$ & $\epsilon_{87} = 5$	21
η		$\eta_{85} = 0.72$ & $\eta_{87} = 0.28$	
x		3.2	2.9
[A]	(amagat)	2.61×10^{-6}	3.72×10^{-6}
I		$I_{85} = 5/2$ & $I_{87} = 3/2$	7/2

Table 4.5: Rb and Cs parameters that are needed to determine the fundamental decay rates γ_{Rb} and γ_{Cs} according to Eq. 4.46.

With these modifications and substitutions, and using Nelson and Walker's [34] values for κ , C , $\langle\sigma_{ex}\nu\rangle$ and $\langle\sigma_{bin}\nu\rangle$ in the case of Rb (table 4.6), we plotted the modified function vs. total gas density on top of our data points and as it can be seen in Fig. 4.13, the blue line is Nelson and Walker's model for 3% Xe, which matches our data points. Indicating that our data points seem to be consistent with the theoretical model, so in the case of Rb, under our experimental condition, it is reasonable to have the same parameters as Nelson and Walker.

In Fig. 4.13, the red line shows the prediction of Nelson and Walker's model in the case of Cs being adjusted to our experimental conditions. For Cs, we used the same values of κ , C and $\langle\sigma_{ex}\nu\rangle$ that Nelson and Walker used for Rb, but ~ 1.4 times bigger $\langle\sigma_{bin}\nu\rangle$ (table 4.6), and as it can be seen in Fig. 4.13 one can say that our

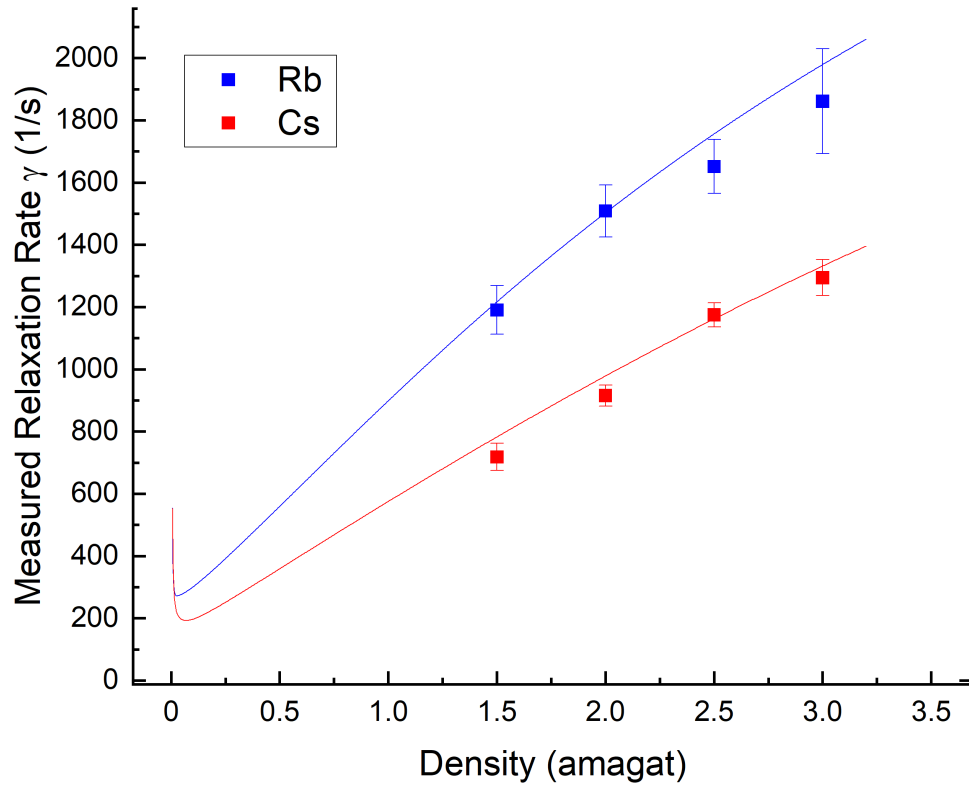


Figure 4.13: Rb and Cs measured relaxation rate γ_A vs. total density for fixed gas composition 94% ^4He , 3% N_2 and 3% Xe at 130°C . The blue line is Nelson and Walker's model adjusted for Rb under our experimental conditions of 3% Xe and 130°C temperature. The red line is what Nelson and Walker's model would predict in the case of Cs under our experimental conditions.

Parameter	Unit	Rb	Cs
κ	(amagat ⁻¹)	4.1×10^{-3}	4.1×10^{-3}
C	(amagat ⁻¹ s ⁻¹)	9.8×10^9	9.8×10^9
$\langle \sigma_{\text{ex}} \nu \rangle$	(amagat ⁻¹ s ⁻¹)	2.3×10^{10}	2.3×10^{10}
$\langle \sigma_{\text{bin}} \nu \rangle$	(amagat ⁻¹ s ⁻¹)	244000	341600
Γ_{vW}	(s ⁻¹)	6428	8024

Table 4.6: Rb and Cs parameters used to plot the solid lines of Fig. 4.13.

points match the predicted theoretical model to a large extent. The larger value of $\langle \sigma_{\text{bin}} \nu \rangle$ in the case of Cs, is supported by the larger spin-exchange and spin-rotation, cross-sections in the case of Xe-Cs than Xe-Rb, reported in [63]. Following Nelson and Walker's [62] steps in order to apply the perturbation theory and get the coefficients A , B , and E regarding the correction terms in Eq. 4.46, in terms of Rb we got

$$\begin{aligned}
A &= -0.0449 \\
B &= -0.0416f_{S85} - 0.0482f_{S87} + 0.00669f_{F85} - 0.0151f_{F87} \\
E &= -0.2536f_{S85}^2 + 0.00909f_{S85}f_{S87} - 0.0286f_{S87}^2 - 0.000933f_{F85}^2 \\
&\quad + 0.0042f_{F85}f_{F87} - 0.00473f_{F87}^2 - 0.00248f_{S85}f_{F85} \\
&\quad + 0.000557f_{S85}f_{F87} + 0.00917f_{S87}f_{F85} - 0.0206f_{S87}f_{F87}
\end{aligned} \tag{4.48}$$

and in the case of Cs,

$$A = -0.0197 \quad B = -0.0394f_S \quad C = -0.0197f_S^2. \tag{4.49}$$

4.5 Conclusion

In this work, we measured the alkali-metal electron spin-relaxation rate and calculated its respective electron-randomization rate for both Xe-Rb and Xe-Cs systems for a fixed gas composition of 94% ^4He , 3% N_2 and 3% Xe over the total gas density range of 1.5-3 amagat. We found out that the electron-randomization rate Γ_A for the Xe-Rb system is $\sim 30\%$ lower than the electron-randomization rate for the Xe-Cs system (table 4.3), $\Gamma_{\text{Rb}} \simeq 0.7\Gamma_{\text{Cs}}$. We tested and compared our results with Nelson and Walker's theoretical model [62] and based on the Fig. 4.13, it is valid to say that by applying the right adjustments to the model to incorporate our experimental conditions, our results match their theoretical predictions to a large extent which resulted in the values for different parameters in table 4.6 based on our experimental conditions.

The measured relaxation rates for these alkali-metals are predominantly due to Xe. Considering the conditions under which we performed the measurements, other relaxation mechanisms are negligible with respect to the contribution of Xe. Hence, it is valid to consider the calculated electron-randomization to be due to Xe and call it $\Gamma_A^{(\text{Xe})}$. This $\Gamma_A^{(\text{Xe})}$ is one of the parameters needed to calculate the alkali-metal-noble gas spin-exchange efficiency

$$\eta_{\text{se}} = \frac{\gamma_{\text{se}}/[\text{A}]}{\Gamma_A^{(\text{Xe})}[\text{Xe}]} = \frac{k_{\text{se}}[\text{Xe}]}{\Gamma_A^{(\text{Xe})}} \quad (4.50)$$

In order to reach a conclusion regarding η_{se} we still need to measure the alkali-metal-noble gas spin-exchange rate γ_{se} . Chapter 5 is dedicated to the study of the alkali-metal-noble gas spin-exchange rate for Xe-Rb and Xe-Cs systems.

CHAPTER 5

SPIN-EXCHANGE RATE COEFFICIENT MEASUREMENTS

5.1 Introduction

SEOP [13, 29] is the preferred technique in producing large quantities of polarized ^{129}Xe and ^3He . In this method, circularly polarized light is used to optically pump the mixture of alkali-metal and noble gas in the vapor phase. The alkali-metal electron spins absorb the angular momentum of photons and get polarized. This polarization is then exchanged between the alkali-metal electron spin and the noble gas nuclear spin through the spin-exchange processes, such as binary collisions and van der Waals molecule formation, resulting in hyperpolarized noble gases. The nuclear spin polarization of these hyperpolarized noble gases is much larger than the thermal equilibrium polarization. This increase in the number of polarized spins will benefit many of their applications, such as MRI [64, 65] and surfaces studies [7, 66]. The most popular noble gases used in the hyperpolarization technique are ^3He and ^{129}Xe , where ^{129}Xe is more favorable for a variety of investigations in the field of science and medicine [67, 68], because of its characteristics and qualities, such as having a strong interaction with other chemical and biological molecules, Xe is soluble in lipids and thus in a wide variety of tissues, having strong chemical shift and etc [69]. For a long time, Rb was the chosen alkali-metal for the SEOP process because of the inexpensive high-power lasers available at the D_1 resonance. Now studies have shown

both experimentally [70, 71] and theoretically [72, 73] that Cs tends to have a higher spin-exchange cross-section with the ^{129}Xe . In addition, at the same temperature, Cs has higher vapor pressure than Rb and its optical pumping rate is $\sim 12\%$ faster than Rb per watt of D_1 laser light [73]. These properties, along with recent progress in producing diode lasers at the longer Cs D_1 wavelength of 895 nm, have increased interest in studying the Xe-Cs system and comparing it to Xe-Rb. For measuring the SEOP efficiency, we need to have information about the spin-destruction rate of the alkali-metal electron as well as the spin-exchange rate between the alkali-metal and the noble gas. For both Xe-Rb and Xe-Cs systems, the spin-exchange happens through binary collisions and van der Waals molecules [12, 28]. There exist many studies on Xe-Rb systems [14, 28, 69, 74], but there are fewer investigations of Xe-Cs. Refs. [75, 76] conducted studies on Xe-Cs van der Waals molecules, and some studies exist on the binary piece of Xe-Cs spin-exchange [73]. However, the previous measurements and studies are old and they were mostly done using a method called ‘the relaxation rate’ method which is particularly bad for Xe because it requires assumptions about the temperature dependence of the wall-relaxation rate. Many of these studies also make assumptions about the alkali-metal number density by using the vapor-pressure curve, which we know is unreliable. That’s why these measurements need to be reproduced by alternative methods. In this work, the goal is to study and

compare the SEOP efficiency for Xe-Rb and Xe-Cs systems,

$$\eta_{\text{se}} = \frac{\gamma_{\text{se}}/[A]}{\Gamma_{\text{A}}^{(\text{Xe})}/[\text{Xe}]} = \frac{\gamma_{\text{se}}[\text{Xe}]}{\Gamma_{\text{A}}^{(\text{Xe})}[A]} = \frac{k_{\text{se}}[\text{Xe}]}{\Gamma_{\text{A}}^{(\text{Xe})}} \quad (5.1)$$

where $[A]$ and $[\text{Xe}]$ are the alkali-metal and noble gas Xe number densities, γ_{se} is the alkali-metal-noble gas spin-exchange rate, $\Gamma_{\text{A}}^{(\text{Xe})}$ is the alkali-metal electron-randomization rate due to Xe, and k_{se} is the alkali-metal-noble gas spin-exchange rate coefficient. For this, we had to measure the alkali-metal electron-randomization rate due to the Xe ($\Gamma_{\text{A}}^{(\text{Xe})}$) and the spin-exchange rate coefficient k_{se} .

We measured the electron-randomization rate via relaxation in the dark and obtained the result that the Rb rate is $\sim 30\%$ slower than the Cs rate. In this work, we have measured the spin-exchange rate coefficient via a method called ‘repolarization’ [77].

5.2 Theory

Fundamental time evolution of the noble gas (Xe in our case) polarization due to spin-exchange collisions with alkali-metal atoms can be described as [29]

$$\frac{dP_{\text{Xe}}}{dt} = k_a[A] (\bar{P}_{\text{A}} - P_{\text{Xe}}) - \Gamma_w P_{\text{Xe}} + k_b[A] \left(-\frac{\bar{P}_{\text{A}}}{2} - P_{\text{Xe}} \right) \quad (5.2)$$

the first term in Eq. 5.2 is the spin-exchange term between the alkali-metal atom and noble gas atom, $P_A = \langle S_z \rangle / S$ is the volume averaged spin polarization of alkali-metal and $P_{Xe} = \langle K_z \rangle / K$ is the noble gas nuclear spin polarization. Where S_z and K_z are the alkali-metal electron and noble gas nuclear longitudinal spin with z being the direction of the applied static magnetic field, S and K are the alkali-metal spin and noble gas nuclear quantum numbers respectively and k_a is the isotropic hyperfine interaction coefficient arising from the Fermi contact fields that the two nuclei create. The spin-exchange between the alkali-metal electron and noble gas nucleus happens during these Fermi contact hyperfine interactions. The second term Γ_w is the relaxation that arises from the noble gas collisions with the container wall [13, 29]. The third term with the coefficient k_b is the spin-exchange term between the alkali-metal atom and noble gas atom due to the anisotropic hyperfine interaction. This term arises from the effect of the alkali-metal electron magnetic field on the noble gas magnetic moment through-space (as opposed to contact), and it has been shown both experimentally and theoretically that this term is small compared to the isotropic interaction [13, 29]. Hence, we can neglect the term k_b , and we set $k_a = k_{se}$. The isotropic interaction polarizes the noble gas atoms parallel to the alkali-metal electron spin, and the anisotropic interaction polarizes the noble gas atom anti-parallel to the

alkali-metal electron spin [29]. The solution to Eq. 5.2 is

$$P_{\text{Xe}}(t) = \frac{k_{\text{se}}[\text{A}]}{k_{\text{se}}[\text{A}] + \Gamma_{\text{w}}} (\bar{P}_{\text{A}} - e^{-(k_{\text{se}}[\text{A}] + \Gamma_{\text{w}})t}) \quad (5.3)$$

One can see from Eq. 5.3 that the noble gas polarization build-up rate is

$$\Gamma_{\text{Xe}} = k_{\text{se}}[\text{A}] + \Gamma_{\text{w}} \quad (5.4)$$

and when we wait long enough the steady-state noble gas polarization is

$$P_{\text{Xe}}(\infty) = \frac{k_{\text{se}}[\text{A}]}{\Gamma_{\text{Xe}}} \bar{P}_{\text{A}} \quad (5.5)$$

Eqs. 5.4 and 5.5 point to two methods for measuring k_{se} . The first method is known as the ‘relaxation rate’ method in which Γ_{Xe} is measured as a function of alkali-metal density $[\text{A}]$, and the slope of the graph is the spin-exchange rate coefficient k_{se} , while the intercept is Γ_{w} [78, 79]. One assumption in this method is that Γ_{w} is temperature independent, and it requires measuring the alkali-metal density $[\text{A}]$ or estimating it from vapor-pressure curves.

The second method relies on Eq. 5.5, and it’s called the ‘rate balance’ method

[77]. One can solve Eq. 5.5 for k_{se}

$$k_{\text{se}} = \frac{P_{\text{Xe}}\Gamma_{\text{Xe}}}{P_{\text{A}}[A]} \quad (5.6)$$

all the quantities on the right-hand side of this equation, including the alkali-metal density, must be measured. But there is no need for any assumption regarding Γ_{w} since any effect on Γ_{w} due to the temperature will affect P_{Xe} and Γ_{Xe} in a way that their product stays constant [77].

The third method that we used in our measurement is the ‘repolarization‘ method introduced by Baranga [47]. This method utilizes the measurement in the dark, which will simplify things, and the key points of this method are that there is no need for any assumption about Γ_{w} , and one does not need to measure the alkali-metal number density. This method relies on the spin-exchange process between the alkali-metal and noble gas, where the polarization transfers between the polarized alkali-metal atom electron and the nuclei of the noble gas atoms during collisions. This process is a two-way process, meaning the same way that polarized alkali-metal can transfer its electron spin polarization to the noble gas nuclear spin, the reverse can happen as well. As explained before, angular momentum transfer between the alkali-metal and the noble gas happens during binary collisions or van der Waals molecule formation in the presence of a third body. For a noble gas, like Xe, at a low gas pressure of a few tens of torr, the van der Waals molecules play a significant role in both spin-exchange

and spin-relaxation of atoms compared to the binary collisions. Since the lifetime of these molecules is in the order of nanoseconds being long enough, F is a good quantum number, and only $\Delta F = 0$ transitions are allowed. At these low pressures, to diminish the effects of van der Waals molecules, one has to have a high magnetic field of a few hundred Gauss [12]. On the other hand, at higher gas pressures of multi-atmosphere, where we perform our experiments, the van der Waals molecules' lifetime is so short that they can be neglected compared to the binary collisions. The spin-dependent interactions such as the spin-rotation interaction $\mathbf{N} \cdot \mathbf{S}$ and the isotropic hyperfine interaction (binary spin-exchange) $\mathbf{K} \cdot \mathbf{S}$ between the alkali-metal atoms and noble gas atoms are responsible for the alkali-metal spin-loss process

$$V(R) = \gamma(R) \mathbf{N} \cdot \mathbf{S} + \alpha(R) \mathbf{K} \cdot \mathbf{S} \quad (5.7)$$

the first term is the coupling between the alkali-metal electron spin \mathbf{S} and the rotation angular momentum of the colliding pair \mathbf{N} ; it roots back in the magnetic field generated by the moving charges in the collision and the isotropic hyperfine interaction between \mathbf{S} and noble gas nuclear spin \mathbf{K} is from the magnetic field inside the nucleus of the noble gas atom [29]. spin-loss happens during interactions in Eq. 5.7, while the spin-rotation $\mathbf{N} \cdot \mathbf{S}$ causes the alkali-metal to lose polarization, the isotropic hyperfine interaction $\mathbf{K} \cdot \mathbf{S}$ transfer spin polarization back-and-forth between the alkali-metal electron and the noble gas nucleus. In the absence of pumping light and in the spin

temperature limit, the total alkali-metal longitudinal spin $F_z = S_z + I_z$ and polarization time evolution are [29]

$$\frac{dF_z}{dt} = D\Delta^2\langle F_z \rangle - \Gamma_w\langle S_z \rangle + k_{se}[\text{Xe}] (\langle K_z \rangle - \langle S_z \rangle) \quad (5.8)$$

$$\frac{dP_A}{dt} = D\Delta^2 P_A - \frac{\Gamma_w}{\varepsilon} P_A + \frac{k_{se}[\text{Xe}]}{\varepsilon} (P_{\text{Xe}} - P_A) \quad (5.9)$$

In both Eq. 5.8 and Eq. 5.9, the first term is the diffusion term, which is negligible since, in our case, the collisional losses are greater than the diffusion losses; the second term is the alkali-metal electron spin-relaxation term due to all other collisional processes except the spin-exchange interaction with the noble gas, and the last term is the spin transfer term in which the alkali-metal atom both loses its polarization to the noble gas atom and gains polarization from the polarized noble gas atom known as the ‘back polarization’. Based on the definitions one can see that $k_{se}[\text{Xe}] + \Gamma_w = \Gamma_A$ which is the alkali-metal electron-randomization rate and $\frac{k_{se}[\text{Xe}]}{\varepsilon} + \frac{\Gamma_w}{\varepsilon} P_A = \frac{\Gamma_A}{\varepsilon} = \gamma_A$ which is the measured alkali-metal electron spin-relaxation rate and ε is the slowing down factor. At the steady state using Eq. 5.9 one can get k_{se} [77]

$$k_{se} = \frac{\Gamma_A P_A}{P_{\text{Xe}}[\text{Xe}]} \quad (5.10)$$

resulting in alkali-metal polarization to be

$$P_A = \frac{k_{se}P_{Xe}[Xe]}{\Gamma_A} \quad (5.11)$$

this equation states that in the absence of the pumping light, the alkali-metal polarization is a balance between the rate at which it gets its polarization back from the noble gas through the spin-exchange process and the rate at which it loses its polarization during these collisions. For measuring the spin-exchange rate coefficient k_{se} using the ‘repolarization‘ method Eq. 5.10, there are a few parameters that need to be measured experimentally:

- Γ_A : the alkali-metal electron-randomization rate (A detailed explanation of the theory and how we measured the spin-destruction rate is given in Chapter 4).
- $[Xe]$: the noble gas number density.
- P_{Xe} : the noble gas polarization, which has reached a steady state.
- P_A : the alkali-metal steady state polarization in the absence of light, which arises from the spin-exchange with the polarized noble gas, transferring polarization back to the alkali-metal electron spin.

5.2.1 The Noble Gas Density

The Xe density [Xe] is measured precisely while we are making the cells and filling them with different gases using the ideal gas law, as explained in Chapter 3, but for experimental purposes, it will be easier to measure $P_{\text{Xe}}[\text{Xe}]$ together as one parameter.

5.2.2 The Noble Gas Polarization

The Xe polarization is measured by measuring the alkali-metal frequency shift due to the Xe polarization. Groover [27] was the first one who showed that the polarized noble gas atom will induce a shift in the electron paramagnetic resonance frequency of the alkali-metal atom. This effect is a two-way effect, meaning polarized alkali-metal atoms will cause a shift in the nuclear magnetic resonance of the noble gas, as well. The Fermi-contact interaction $\alpha \mathbf{K} \cdot \mathbf{S}$ between the alkali-metal electron spin \mathbf{S} and the noble gas nuclear spin \mathbf{K} , is responsible for these frequency shifts by producing an average additional magnetic field, as well as the spin-exchange between the two species. The coupling coefficient α depends on the inter-atomic separation R and can be expressed as [80]

$$\alpha(R) = \frac{8\pi}{3} g_s \mu_B \frac{\mu_K}{K} |\psi(R)|^2 \quad (5.12)$$

where $\psi(R)$ is the wave function of alkali-metal valance electron, μ_K is the noble gas magnetic moment, μ_B is the Bohr magneton, and $g_s = 2$ is the electron g factor. As a result of this interaction, the magnetic moments of the two species cause each

to experience a strong magnetic field from the other. This interaction and change in the magnetic field that the polarized spins cause will result in a shift in their Larmor precession frequency [29]. At low enough magnetic fields, one can neglect the quadratic Zeeman effect on the splitting of the hyperfine resonances of the alkali-metal atom. The frequency shift that the alkali-metal experiences due to the polarized noble gas is [29]

$$\Delta|\nu_A| = \frac{8\pi}{3} \frac{d\nu}{dB} \kappa_{\text{AXe}} M_{\text{Xe}} = \frac{8\pi}{3} \frac{1}{h} \frac{g_s |\mu_B|}{(2I+1)} \frac{\mu_K}{K} \kappa_{\text{AXe}} [\text{Xe}] \langle K_z \rangle \quad (5.13)$$

A similar relation holds for the frequency shift of the noble gas nuclear magnetic resonance frequency as well. I and K are the alkali-metal and noble gas nuclear spins, respectively. K_z is the longitudinal noble gas nuclear spin, h is Planck's constant, and $d\nu/dB$ is the alkali-metal gyromagnetic ratio. For a given noble gas magnetization, the scale of the shift is determined by κ_{AXe} and the alkali-metal gyromagnetic ratio. κ_{AXe} is called the enhancement factor, and the way it is defined in [27], it is a ratio of magnetic field increment that the valence electron of the alkali-metal atom experiences to the field increment that the noble gas with the same density and nuclear polarization will produce in a spherical cell. κ_{AXe} can be written as [80]

$$\kappa_{\text{AXe}} = (\kappa_0 - \kappa_1) + \epsilon_{\text{AXe}} \kappa_1 \quad (5.14)$$

where $(\kappa_0 - \kappa_1)$ refers to the alkali-metal-noble gas binary collision and $\epsilon_{\text{AXe}}\kappa_1$ refers to the van der Waals molecules contribution. In [80], the definitions of κ_0 and κ_1 are given but at high pressure regime κ_{AXe} goes to κ_0 which is a pressure-independent quantity

$$\kappa_0 = \int_0^\infty \eta^2 |\psi(R)|^2 e^{-V(R)/K_B T} 4\pi R^2 dR \quad (5.15)$$

In Eq. 5.15, $V(R)$ is the van der Waals potential, describing the force between the alkali-metal and the noble gas atoms [29], so in this limit, and knowing the fact that $P_{\text{Xe}} = \langle K_z \rangle / K$, the alkali-metal EPR frequency shift due to the polarized noble gas is

$$\Delta|\nu_A| = \frac{8\pi}{3} \frac{d\nu}{dB} \kappa_0 \mu_{\text{Xe}} P_{\text{Xe}}[\text{Xe}] \quad (5.16)$$

One can get the term $P_{\text{Xe}}[\text{Xe}]$ from this equation

$$P_{\text{Xe}}[\text{Xe}] = \frac{3}{8\pi} \frac{\Delta|\nu_A|}{\frac{d\nu}{dB} \kappa_0 \mu_{\text{Xe}}} \quad \longrightarrow \quad P_{\text{Xe}}[\text{Xe}] = \frac{3}{8\pi} \frac{\Delta|\nu_A|}{\frac{\gamma_A}{2\pi} \kappa_0 \frac{\gamma_{\text{Xe}}}{2\pi} hK} \quad (5.17)$$

So, to get $P_{\text{Xe}}[\text{Xe}]$ we need to measure the alkali-metal frequency shift due to the noble gas polarization $\Delta\nu_A$ and use the known constants such as the enhancement factor κ_0 , alkali-metal gyromagnetic ratio $\frac{\gamma_A}{2\pi}$, noble gas gyromagnetic ratio $\frac{\gamma_{\text{Xe}}}{2\pi}$, Planck's constant h and the noble gas nuclear spin K .

5.2.3 The Alkali-Metal Back Polarization

The last piece to Eq. 5.10 is the alkali-metal back polarization P_A in the dark, which is from the exchange with the polarized noble gas. To measure the back polarization of the alkali-metal atom, one can employ the measurement in the dark. As it is stated in [77] and shown in Chapter 4, at high polarization, and while pumping light is on, the area under the alkali-metal, resonance peaks represent the alkali-metal polarization at that stage

$$P = \frac{[F(F+1) - (m-1)(m-2)]A - [F(F+1) - m(m-1)]}{[F(F+1) - (m-1)(m-2)]A + [F(F+1) - m(m-1)]} \quad (5.18)$$

where A is the ratio of the area under the $|F \ m\rangle \rightarrow |F \ m-1\rangle$ transition peak to the area under the $|F \ m-1\rangle \rightarrow |F \ m-2\rangle$ transition peak. In the case of ^{87}Rb , with $I = 3/2$, taking the two peaks representing $|2 \ 2\rangle \rightarrow |2 \ 1\rangle$ and $|2 \ 1\rangle \rightarrow |2 \ 0\rangle$ transitions, we get

$$P_{\text{Rb}} = \frac{3A - 2}{3A + 2} \quad (5.19)$$

and in the case of Cs, with $I = 7/2$, by taking the two peaks representing $|4 \ 4\rangle \rightarrow |4 \ 3\rangle$ and $|4 \ 3\rangle \rightarrow |4 \ 2\rangle$ transitions, one can get

$$P_{\text{Cs}} = \frac{7A - 4}{7A + 4} \quad (5.20)$$

Knowing the absolute polarization in the light (high polarization where the formula holds) for these alkali-metal atoms and relating that polarization to the total area under all the resonance peaks, it is straightforward to use that value and map out the polarization decay using the area under the peaks for all the spectra that we get from the measurement in the dark, we can get the absolute polarization in the dark.

5.3 Experimental Setup and Procedure

For measuring the alkali-metal and noble gas spin-exchange rate coefficient k_{se} based on Eq. 5.10, there are a few parameters that need to be measured. The noble gas Xe number density is measured while making the cells using the ideal gas law as explained in Chapter 3, the alkali-metal back polarization P_A from polarized Xe, while the pumping light is blocked and being in the dark, the alkali-metal electron-randomization Γ_A and the Xe polarization P_{Xe} . Experiments are done on the same cells that we used in the alkali-metal spin-relaxation measurements in Chapter 4. Two sets of 1-inch-diameter, spherical Pyrex cells, one set had a few milligrams of Rb, and the other set had a few milligrams of Cs metal with four different total pressures 1.5, 2, 2.5, and 3 amagats with fixed gas composition of 94% ^4He , 3% N_2 and 3% enriched ^{129}Xe (table 4.1). The optical pumping setup is shown in Fig. 3.14, where we used two 40-W diode laser arrays (models M1B15-790-SS4.1 and M1B-892.2-60C-SS4.3 from DILAS for Rb and Cs, respectively) to pump the samples optically. The

lasers were tuned to D_1 resonance of Rb and Cs, and they were narrowed to ~ 0.3 nm via an external Littrow cavity. The pump light was linearly polarized, and we used a $1/4$ wave plate to make the linearly polarized light circularly polarized for optical pumping purposes. We did optical detection via Faraday rotation for this experiment. We used two 120-mW diode lasers from Photodigm DBR lasers (models PH780 DBR and PH852 DBR for Rb and Cs, respectively) tuned to ≈ 0.6 nm off the D_2 resonances of Rb and Cs with line widths of 0.7 and 0.5 MHz in case of Rb and Cs respectively. We detected the Faraday rotation of the linearly polarized probe light using a set of balance photodiodes (model PDB415 A from ThorLabs). Our optical detection setup is explained and shown in Chapter 3, section 5. For measuring the alkali-metal electron-randomization and back polarization from the polarized noble gas atoms, we repeated the relaxation in the dark measurement using pulsed EPR as described in Chapter 4. We used an optical chopper with a 50% duty cycle on the path of our pump beam with a frequency of 40 Hz and a period of 25 ms (12.5 ms blocking the light and 12.5 ms letting the light pass through), and the Redstone NMR spectrometer (tecmag) to both generate the EPR pulses and receive the free induction decay FID signal of the sample from the photodetector. The details of the equipment and how we did the experiment are described in detail in Chapter 4. Here, we made some changes to the way we performed the experiment. In this measurement, we wanted to get the value of polarization from the ratio of areas

under the alkali-metal resonance peaks using Eq. 5.18. Hence we had to perform our experiment at a magnetic field B_0 that would resolve the alkali-metal resonance peaks completely. So, in the case of Rb, we did the measurements at $B_0 \sim 28$ G with the ^{87}Rb EPR frequency of ~ 19.8 MHz and in the case of Cs, we performed our experiment at $B_0 \sim 46$ G with Cs EPR frequency ~ 15.8 MHz. For each alkali-metal atom, we took 57 spectra pulsing with a delay table starting from $1000 \mu\text{s}$ to $12200 \mu\text{s}$ with a step size of $200 \mu\text{s}$. To generate a small oscillating magnetic field B_1 using RF pulses, we chose a pulse amplitude of 15(in TNMR unit) and pulse width of 300 ns, for both Rb and Cs to ensure a small flip angle and hence a small Faraday rotation signal so that the shape of our signal will be intact, and the area under the resonance peaks will be a true representation of the alkali-metal polarization. The schematic of the relaxation in the dark measurement using pulsed EPR is shown in Fig. 4.4. In order to boost our SNR, each FID is a result of 500 scans, and the adjusted receiver gain, each FID corresponds to a delay time in the chopper timetable. Then, using the TNMR software, we took a Fast Fourier Transform (FFT) of the FIDs to get the alkali-metal spectra (Fig. 5.1 and Fig. 5.2).

In the case of Rb, measurements were done at 130°C , and in the case of Cs, they were done at 110°C to create the condition of having almost the same number densities for each alkali-metal atom while doing the experiment to have a more reliable comparison of the results.

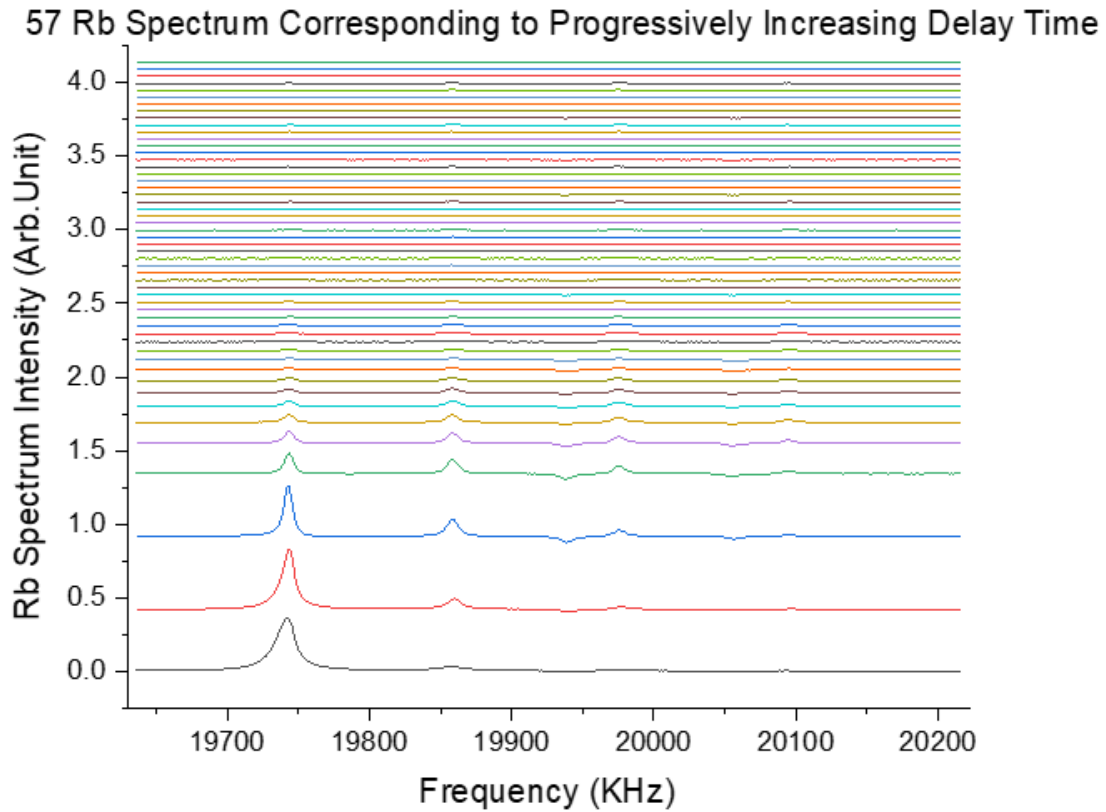


Figure 5.1: Rb spectra from the relaxation in the dark measurement. Shows the polarization decay of the alkali-metal atom as the delay time or, correspondingly, the time spent in the dark increases.

For each sample cell, first, we measured the relaxation in the dark and then the frequency shift measurement under the same condition, with the optical chopper on while doing the measurement to make sure that the frequency shifts that we measured presented the true, noble gas polarization that created the back polarization of the alkali-metal atoms. This sequence was repeated five times for each cell, so the reported results are the average of five measurements, and for reproducibility check,

57 Cs Spectra Corresponding to Progressively Increasing Delay Time

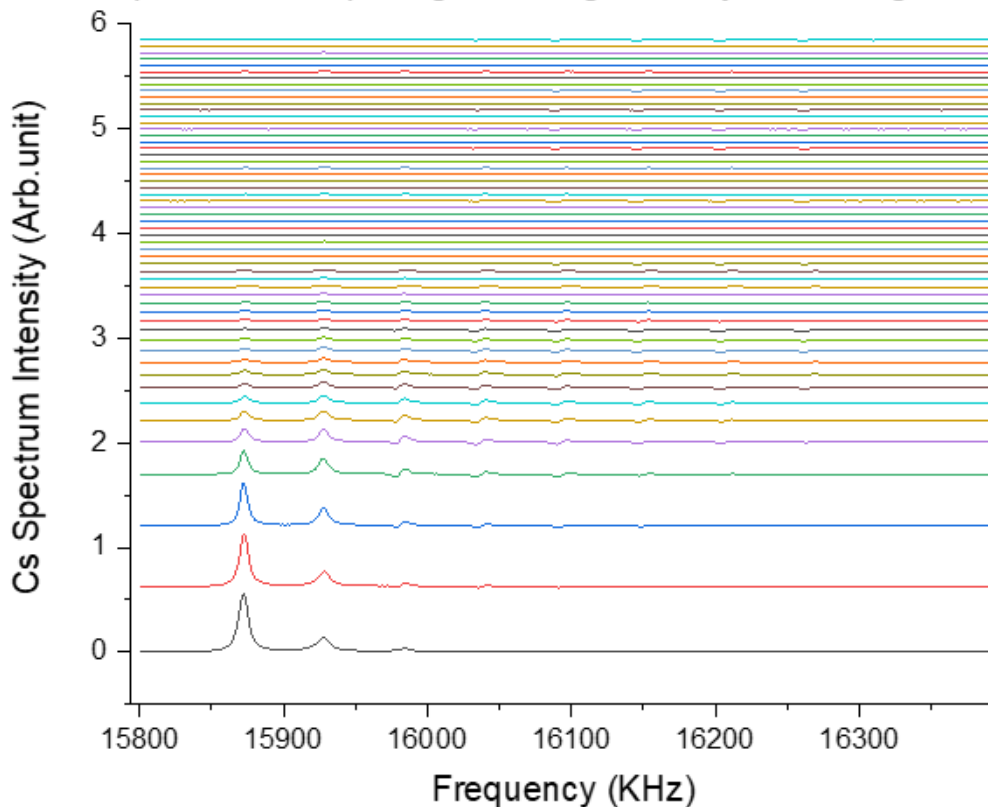


Figure 5.2: Cs spectra from the relaxation in the dark measurement. Shows the polarization decay of the alkali-metal atom as the delay time or, correspondingly, the time spent in the dark increases.

the experiments were done on different days as well.

For the measurement of relaxation in the dark, we used the optical chopper running at 40 Hz to block the pump light, and it sent the trigger to tecmag to start the EPR pulse sequence. We took 57 spectra for each cell corresponding to the delay table of 1000 μ s to 12200 μ s with a step size of 200 μ s to get the polarization decay

of the alkali-metal atoms (Fig. 5.3).

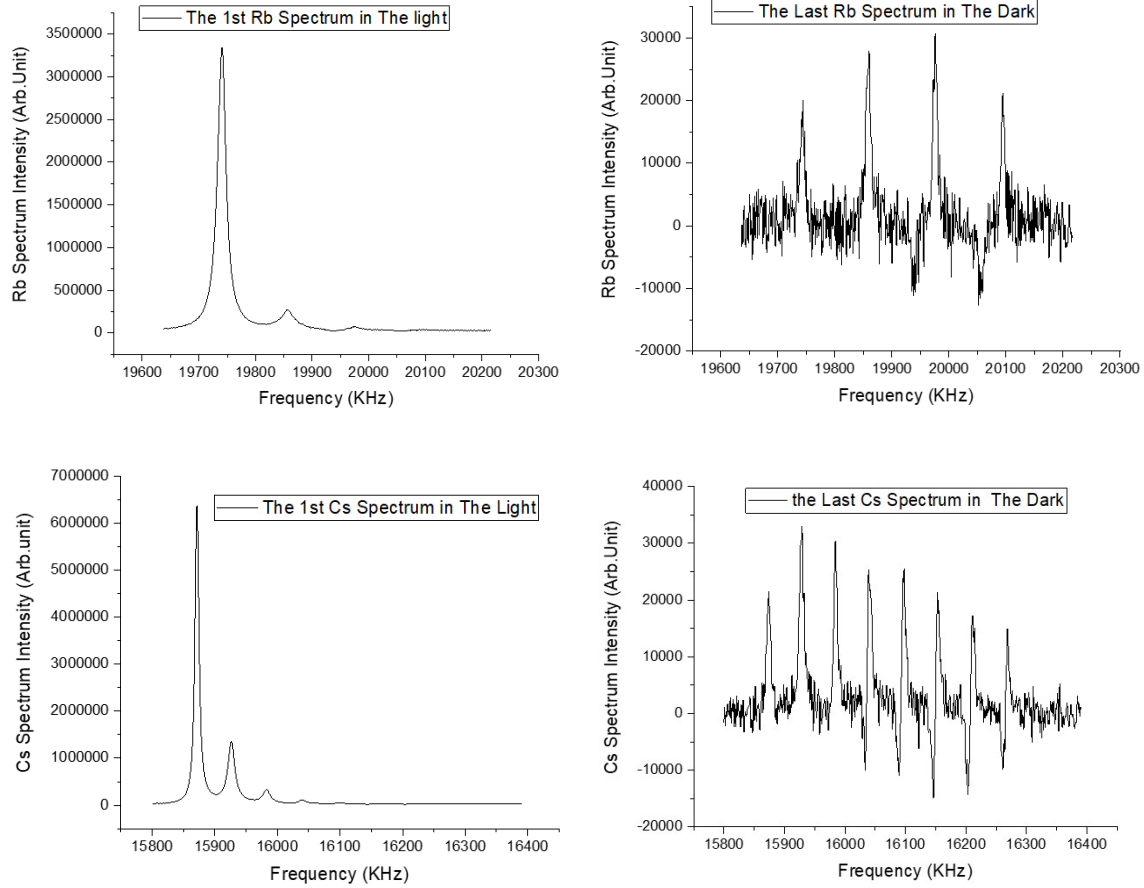


Figure 5.3: The figure on the top left shows the Rb spectrum in the light, and the top figure on the right shows the Rb spectrum after being in the dark for 10 ms. The figures on the bottom show the Cs spectrum in the light (left) and Cs spectrum after being 10 ms in the dark (right).

Using the spectra in the light Fig. 5.3 and Eq. 5.18 we calculated the polarization of alkali-metal atom in the light, and since the polarization is proportional to the total area under the curve, we integrated the area under every spectrum of the 57 spectra, and calculated the polarization for each spectrum and plotted the alkali-metal

polarization decay vs. time (Fig. 5.4 and Fig. 5.5).

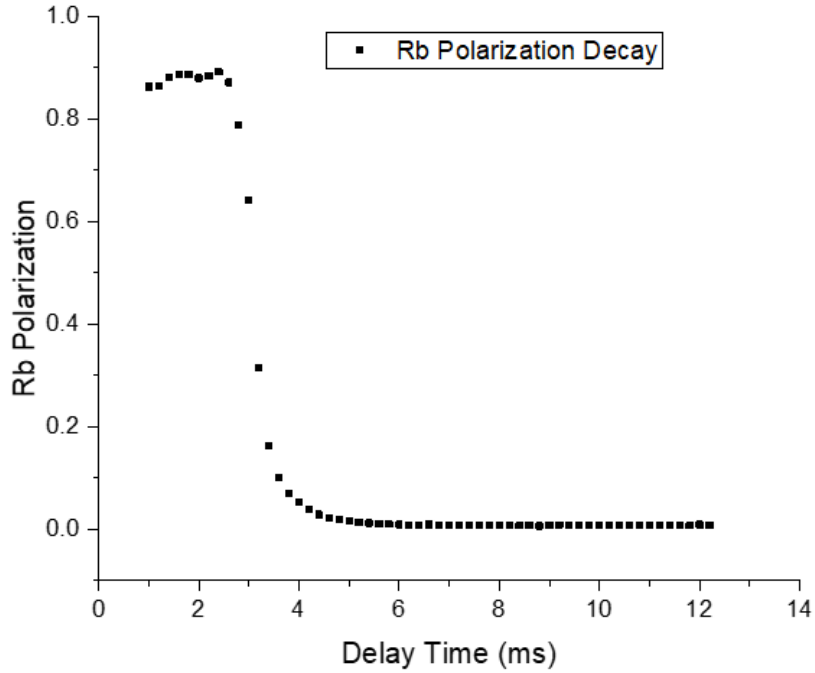


Figure 5.4: Rb polarization decay vs. time as a result of the measurement in the dark. The value of polarization at each timestamp is calculated by integrating the total area under the corresponding spectrum and using the polarization in the light and its area as a reference to calculate the polarization value.

For measuring Xe polarization, we measured the alkali-metal frequency shift since the size of the frequency shift is proportional to the magnetization of the polarized atoms. In our case, the alkali-metal frequency shift is proportional to the Xe magnetization. Therefore, the alkali-metal frequency shift can be used for Xe polarimetry and get the Xe polarization based on Eq. 5.5. In the frequency shift measurement, we follow the frequency of the alkali-metal paramagnetic resonance. Everything in

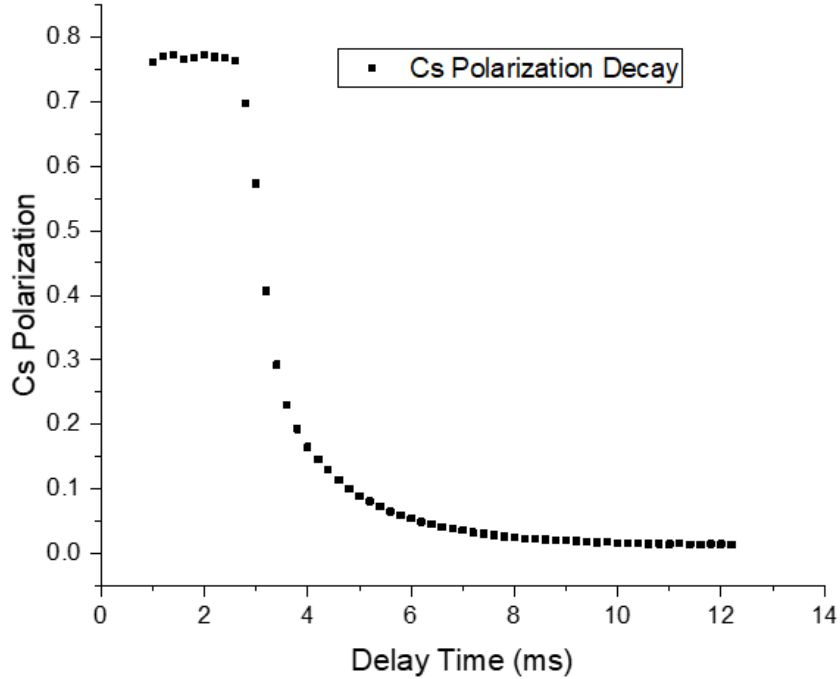


Figure 5.5: Cs polarization decay vs. time as a result of the measurement in the dark. The value of polarization at each timestamp is calculated by integrating the total area under the corresponding spectrum and using the polarization in the light and its area as a reference to calculate the polarization value.

the Eq. 5.5 is known except for the alkali-metal frequency shift, which we measured, and then the polarization of noble gas was determined.

Atom	Nuclear Spin	Gyromagnetic Ratio(kHz/G)	κ_0
^{87}Rb	$I = 3/2$	$ \gamma_1/2\pi = 699.58$	518 ± 8 [81]
Cs	$I = 7/2$	$ \gamma_1/2\pi = 349.86$	629 ± 10 [81]
Xe	$K = 1/2$	$ \gamma_1/2\pi = 1.18$	

Table 5.1: The values of constants in Eq. 5.5. The values of the gyromagnetic ratios for the alkali-metal atoms are the corrected values based on the effect of the static magnetic field.

The design of the experiment is to monitor and follow the alkali-metal EPR frequency using the locking setup and record the change in the alkali-metal EPR frequency as the Xe polarization gets destroyed by using RF pulses. Electronics and equipment needed for the measurement of alkali-metal frequency shift are quite complicated, but here is a broad view of the experimental setup and principles behind it. Fig. 5.6 shows the schematic and different pieces of the experimental setup for frequency shift measurement.

To follow the alkali-metal EPR frequency, we use the traditional locking system that generates an error signal based on an absorptive peak derivative to lock into the EPR frequency and follow it. To get the alkali-metal hyperfine transition, a continuous wave (CW) RF generates the oscillating magnetic field B_1 at the alkali-metal EPR frequency, and this B_1 field is applied parallel to the probe beam and transverse to the pump beam, and the static magnetic field B_0 . Like in the pulsed EPR experiment, the B_1 field will induce transitions between the hyperfine sub-levels of the alkali-metal atom and will flip the spins by a small angle into the transverse plane. In the transverse plane, the spins start the steady state precession about the static magnetic field. This precession results in the Faraday rotation of the linearly polarized beam. This Faraday rotation signal will be manifested as an oscillating voltage at the photodiode with the same frequency as the excitation frequency. The photodiode output signal is fed into an RF mixer (Model ZAD-1-1 15542 from Mini-

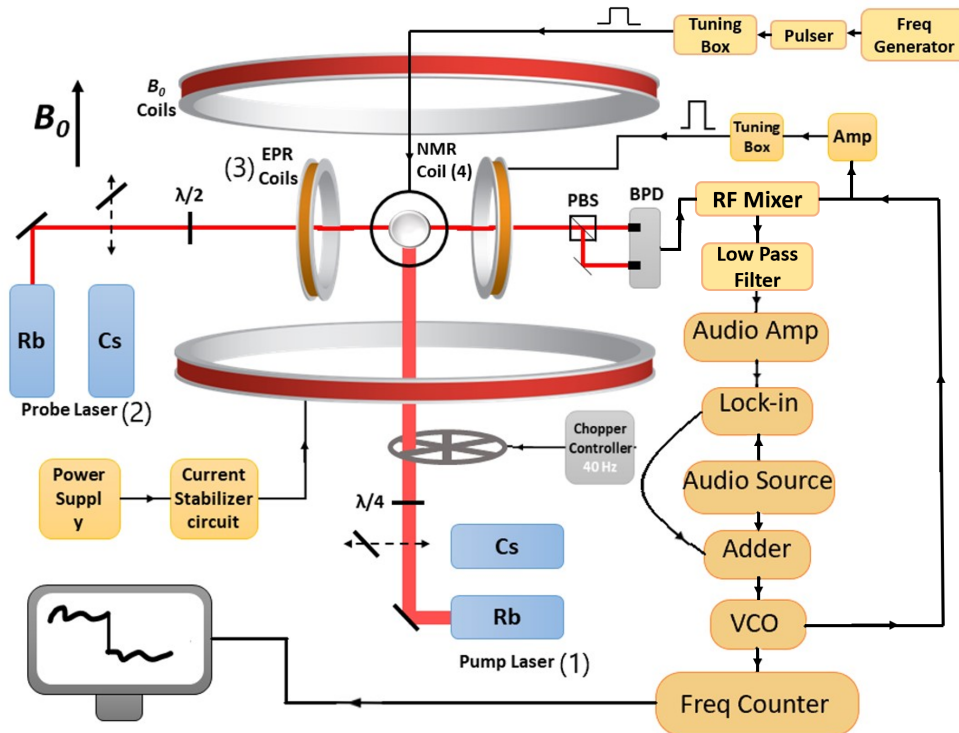


Figure 5.6: Rb and Cs frequency shift measurement schematics and setup in our lab. For measuring the alkali-metal frequency shift, the VCO provides the RF signal and sends it to the RF amplifier, and then the EPR coils to generate the oscillating magnetic field B_1 to excite the alkali-metal spins. The Faraday rotation signal from the photodiode is sent to an RF mixer to mix with the reference signal and get demodulated to an audio frequency. The signal from the mixer gets amplified, and then it is fed to the lock-in amplifier, which is referenced to the modulated frequency from the audio source. The lock-in amplifier generates the error signal based on the derivative of the EPR absorptive peak, and this error signal gets processed using the adder circuit. Then, it is sent back to the VCO, which will output an RF frequency to make the lock-in amplifier output voltage zero. This frequency is shown on the frequency counter. Using the frequency generator and the home-built RF pulse generator, a train of $\sim \pi/2$ pulses is sent to the NMR coil to flip the Xe nuclear spins and saturate them to generate the maximum change in the magnetic field that the alkali-metal electron spins sense and hence get the maximum frequency shift.

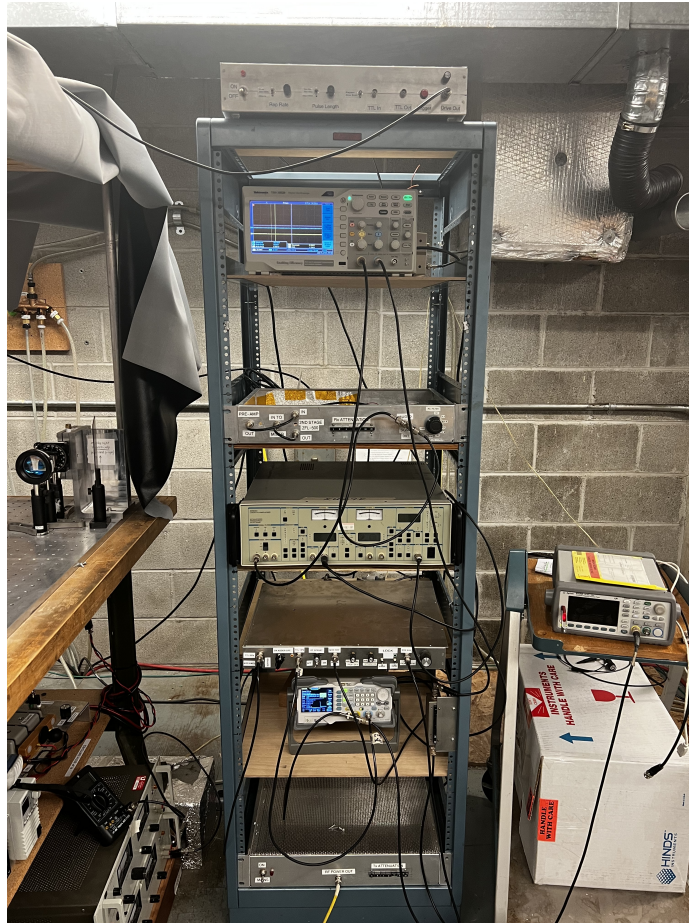


Figure 5.7: The frequency shift measurement electronics used in our laboratory.

Circuits) to get mixed with the same frequency as the alkali-metal EPR frequency and gets demodulated to the audio frequency. Because the mixer outputs the sum and difference of the input frequencies, which here are the same, the output of the mixer will be a DC signal corresponding to the relative amplitude of the two inputs. The purpose of CW RF is to provide a steady state excitation of the alkali-metal spins, and hence this DC level, as the output of the mixer, represents the size of the modulation of the photodiode output, which is a true representation of how much spin

is in the transverse plane. The frequency generator (Model DG1022 from RIGOL) can both do a frequency sweep and receive a DC voltage to program the output frequency (voltage control oscillator). The frequency sweep part is used to generate the alkali-metal spectrum, which can be seen on the oscilloscope, and the VCO is used in the locking scheme to follow the EPR frequency. For following the EPR frequency, the B_1 frequency is modulated at 200 Hz with a modulation amplitude of 4 kHz. When the photodiode output is demodulated, this B_1 modulation, which translates to a 200 Hz envelope modulation of B_1 at the photodiode, will be outputted as a 200 Hz sine wave from the mixer, and then it is fed into the lock-in amplifier (Model SR530 from Stanford Research Systems) to generate the error signal, that is fed back to the VCO to make it follow the EPR frequency. Based on the frequency of the RF excitation with respect to the EPR frequency, the amplitude of modulation out of the RF mixer varies. On either side of the resonance peak, this amplitude is large, and on the top of the peak, it is small. So, when the output of the RF mixer is fed into the lock-in amplifier, the output of the lock-in amplifier is a derivative of the resonance peak. This derivative signal is positive on the left side of the peak, negative on the right side of the peak, and zero on the peak. The zero crossing is the error signal, which is sent to the VCO to follow the EPR frequency. The output of the VCO is then shown on the frequency counter (Model 53220A from Agilent) as a function of time (Fig. 5.8).

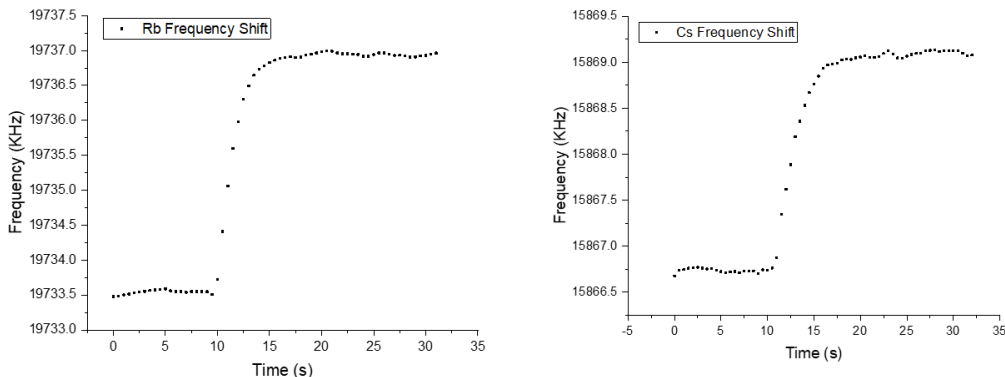


Figure 5.8: Rb and Cs sample Frequency Shift. The frequency counter dwell time was 500 ms. The VCO was locked to the EPR frequency. We allowed the system to become fully polarized and reach equilibrium while the optical chopper was on. Then, using an RF pulse generator, we sent a train of pulses to the NMR coil to destroy the Xe magnetization, which changed the magnetic field sensed by the alkali-metal electron and resulted in the EPR frequency shift. We kept sending the pulses until the Xe magnetization was fully destroyed and the alkali-metal EPR frequency was stable.

The electronics and set up for frequency shift measurement can be divided into two parts. One part includes the VCO, RF mixer, and RF amplifier, which are responsible for generating the B_1 field and demodulating the photodiode output frequency to audio frequency. The other part consists of the audio amplifier, lock-in amplifier, audio source, and the adder circuit, which generate the modulation of excitation frequency, process the error signal from lock-in amplifier, and feed it back to the VCO to make the VCO follow the EPR frequency. After being able to lock to the EPR frequency and follow it by creating a change in the noble gas polarization based on the Fermi-contact interaction, the magnetic field sensed by the alkali-metal spins

changes, which will result in a shift in the EPR frequency, which can be followed, using the locking scheme, and can be seen on the frequency counter. To generate the change in the noble gas polarization, we used a surface coil right below the cell, a frequency generator, and a home-built RF pulse generator. A train of RF pulses at the NMR frequency of Xe, 34k Hz at ~ 28 G and 52 kHz at ~ 46 G, with a pulse width of 100 μ s and repetition rate of 125 ms was sent to an audio amplifier, and then the NMR coil to generate an oscillating magnetic field that excites the noble gas spins and flip them $\sim 90^\circ$. The pulse train destroyed the Xe magnetization, which resulted in a change in the magnetic field the alkali-metal sensed and caused a shift in the alkali-metal EPR frequency. We kept the pulse generator on until the alkali-metal EPR frequency reached an equilibrium. Then, the pulse generator was turned off to allow the Xe to be repolarized and reach its equilibrium value. This process was repeated after each measurement of alkali-metal electron-randomization and back polarization, and each time, three measurements of frequency shift were taken.

5.4 Results and Analysis

After getting the alkali-metal polarization decay vs. time, we followed the steps explained in Chapter 4 in order to fit the low polarization part of the polarization decay transient to a single exponential. The time constant of the single exponential decay represents the alkali-metal spin-relaxation rate, and the Y_0 , the vertical offset or the plateau of the single exponential decay, shows the steady state polarization

that the alkali-metal polarization reaches when it is in equilibrium with the polarized noble gas in the absence of the pump light (Fig. 5.9).

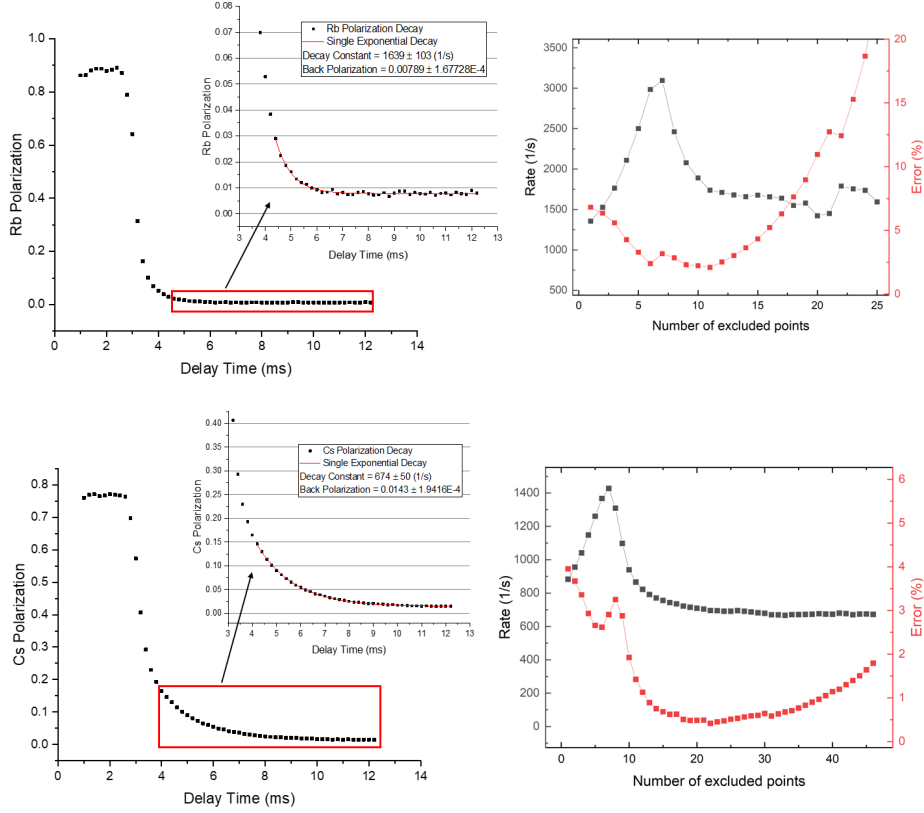


Figure 5.9: Rb and Cs polarization decay single exponential fit procedure. Points were progressively eliminated from the beginning of the decay transient, and the fit was done until the value of the relaxation rate reached a plateau (figures on the right). The single exponential time constant and the Y_0 values from the fit were recorded as the alkali-metal spin-relaxation time and back polarization.

By comparing this alkali-metal polarization decay with a polarization decay transient for the same cell under the same conditions, but with the Xe polarization destroyed with a train of $\pi/2$ pulses (to make sure there is no polarized Xe throughout

the whole relaxation in the dark measurement), one can see that, in this case, the alkali-metal polarization decays to zero (Fig. 5.10). Fig. 5.11 shows the difference in Rb polarization decay for sample cell 309D between the two cases of having polarized Xe throughout the relaxation in the dark measurement and not having polarized Xe.

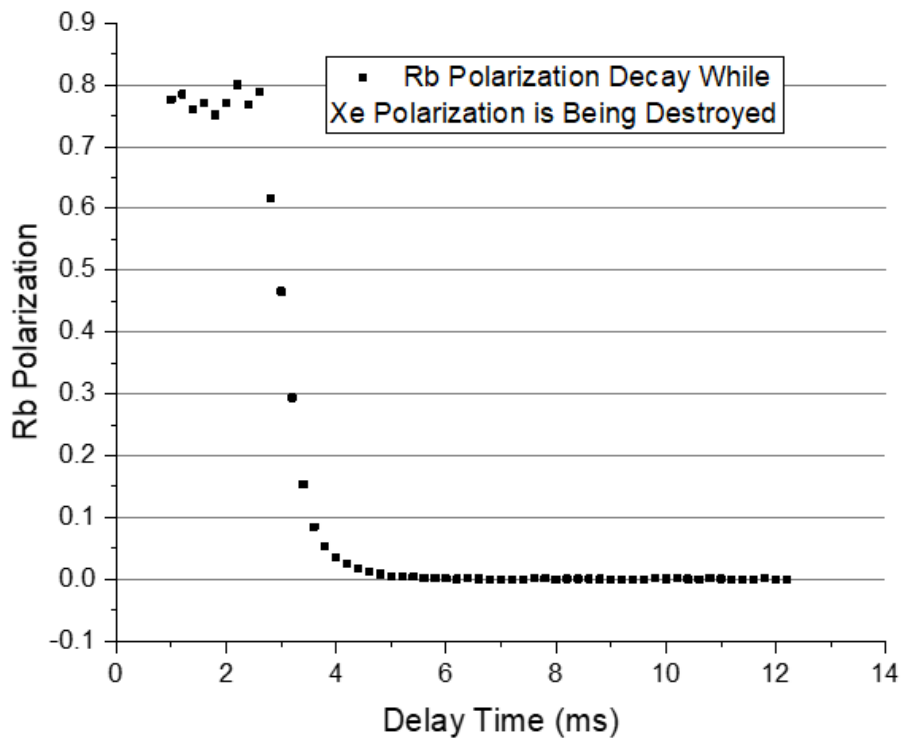


Figure 5.10: Rb polarization decay vs. time, the Xe polarization was destroyed by a train of $\pi/2$ pulses throughout the whole decay to make sure there is no source of polarization to repolarize Rb.

For calculating the alkali-metals frequency shifts, the data from the frequency counter was transferred to the computer and was plotted vs. time using OriginLab software. The frequency counter dwell time was set to 500 ms, and for calculating

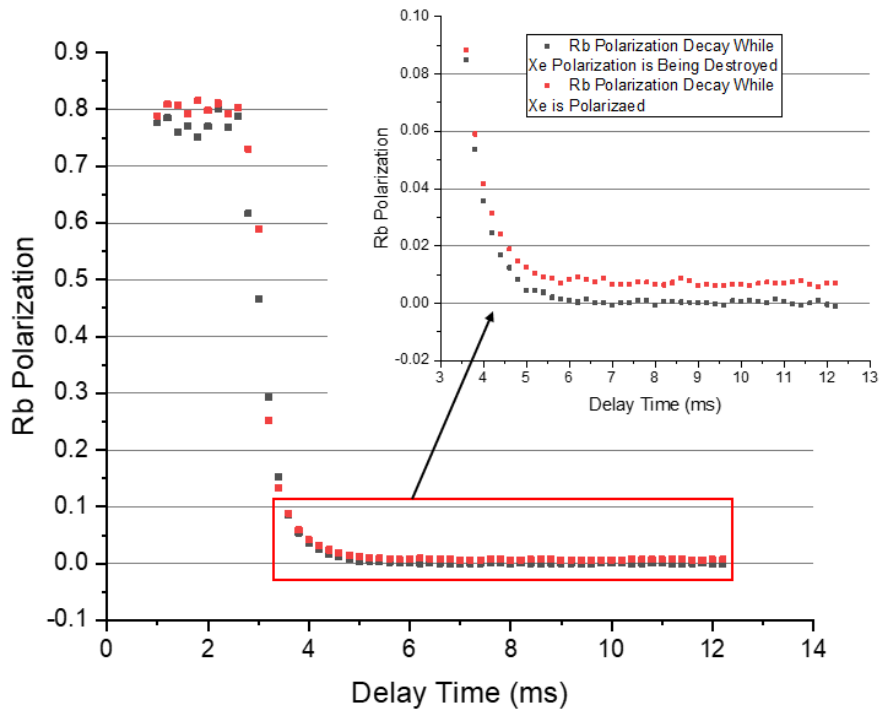


Figure 5.11: Rb polarization decay vs. time, for both cases of having polarized Xe and not having polarized Xe during the relaxation in the dark measurement, on top of each other. It can be seen that in the case of having no polarized Xe, the Rb polarization decays to zero, but in the case that we have polarized Xe, Rb polarization decays to a non-zero level, which indicates the equilibrium state that it reaches with polarized Xe.

the value of the frequency shift, about 10 s of data before the shift and 10 s of data after the shift in the plateau regions (corresponding to about 20 data points on each side) were averaged, and then subtracted to get the frequency shift. The error on the frequency shift is based on the standard deviation of the points that were averaged, Fig. 5.12 shows a sample frequency shift calculation for Rb and Cs.

The results of frequency shifts, spin-destruction rates, and back polarization for

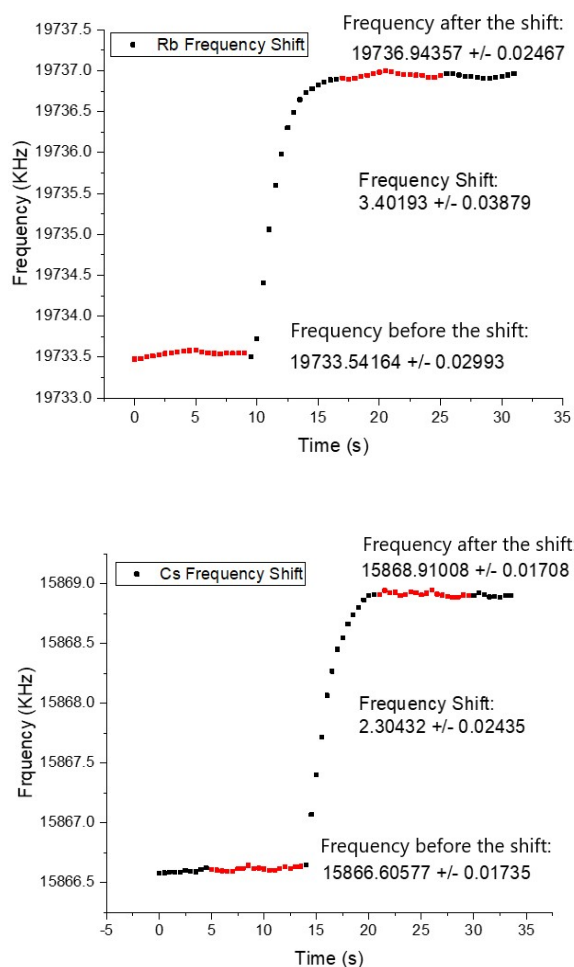


Figure 5.12: Rb and Cs frequency shift calculation. About 10 seconds before and after the shift, corresponding to about 20 points on each side, were chosen to be averaged to get the EPR frequencies before and after the shift. The shifts were calculated by subtracting these two frequencies, and the errors were based on the standard deviation of the chosen points.

both Xe-Rb and Xe-Cs are presented in table 5.2. Using the values and constants in table 5.1 along with the values of the slowing down factor ($\varepsilon = 10.8$ for natural abundance of Rb and 22 for Cs) and the respective equations, It is straightforward to

get the spin-exchange rate coefficient k_{se} and Xe polarization P_{Xe} , which are presented in table 5.3.

Cell	$\Delta\nu_{\text{A}}$ (KHz)	γ_{A} (1/s)	Γ_{A} (1/s)	P_{A}
309A (Rb)	1.89±0.11	1170±80	12636±864	0.0095±0.0004
309C (Rb)	3.48±0.13	1657±105	17895±1134	0.0074±0.0002
309D (Rb)	3.58±0.05	1865±200	20142±2160	0.0067±0.0002
310A (Cs)	1.08±0.06	642±43	14124±946	0.0129±0.0007
310B (Cs)	1.86±0.07	845±56	18590±1245	0.0121±0.0003
310C (Cs)	2.22±0.11	1074±71	23628±1582	0.0095±0.0005
310D (Cs)	2.36±0.08	1169±78	25718±1722	0.0087±0.0002

Table 5.2: Values of measured alkali-metal frequency shift $\Delta\nu_{\text{A}}$, spin-destruction rate γ_{A} , electron-randomization rate Γ_{A} , and back polarization P_{A} from polarized Xe, which come from the single exponential fit of the alkali-metal polarization decay and frequency shift measurements.

Cell	$k_{\text{se}} \times 10^{-16}$ (Cm ³ /s)	P_{Xe}	$[\text{Xe}] \times 10^{19}$ (Cm ³)
309A (Rb)	7.52±0.34	0.157±0.007	0.12
309C (Rb)	4.47±0.20	0.154±0.005	0.21
309D (Rb)	4.43±0.20	0.141±0.004	0.24
310A (Cs)	12.21±0.96	0.164±0.011	0.10
310B (Cs)	8.73±0.40	0.177±0.007	0.16
310C (Cs)	7.29±0.52	0.168±0.008	0.20
310D (Cs)	6.85±0.27	0.148±0.005	0.25

Table 5.3: Calculated values of spin-exchange rate coefficient k_{se} and steady-state Xe polarization P_{Xe} using the measured values in table 5.2, the constants and parameters in table 5.1 and Eqs. 5.10 and 5.5.

In general based on [12] and [70], the spin-exchange rate is

$$\gamma_{\text{se}} = [\text{A}] \left(\frac{k_{\text{se-M}}}{[\text{G}]} + k_{\text{se-B}} \right) \quad (5.21)$$

where $k_{\text{se-M}}$ and $k_{\text{se-B}}$ denote the molecular and binary pieces of the spin-exchange

rate coefficient and $[G]$ is the total gas density, resulting in the total spin-exchange rate coefficient to be

$$k_{se} = \frac{k_{se-M}}{[G]} + k_{se-B} \quad (5.22)$$

By plotting k_{se} vs. $1/\text{total density}$, useful information regarding the spin-exchange rate for different spin-exchange mechanisms can be extracted (Fig. 5.13).

The intercept of the line fit in both graphs represents the binary collision contribution to the spin-exchange rate coefficient k_{se-B} since the intercept corresponds to a very high total gas density, and at high densities, the binary collisions are the dominant process for the spin-exchange between the alkali-metal atoms and Xe. The slope of the line fit indicates the van der Waals molecules' contribution to the spin-exchange k_{se-M} . The results for the binary piece k_{se-B} are comparable to the results that Jau et al. [69, 73] got for the binary piece of spin-exchange rate coefficient in the case of Xe-Rb and Xe-Cs systems, and any observed discrepancy between the values may arise from variations in temperature and gas compositions employed during the respective experiments, and the fact that they performed the experiment at high magnetic field ~ 9 T and then extrapolated the low magnetic field results from their high magnetic field results. The noticeable errors associated with our fit parameters arise from the nature of the linear fit and the fact that we have very few data points.

By plotting the k_{se} values for Xe-Rb and Xe-Cs systems vs. $1/\text{total density}$ on the same graph, one can get a better understanding of the difference between the two

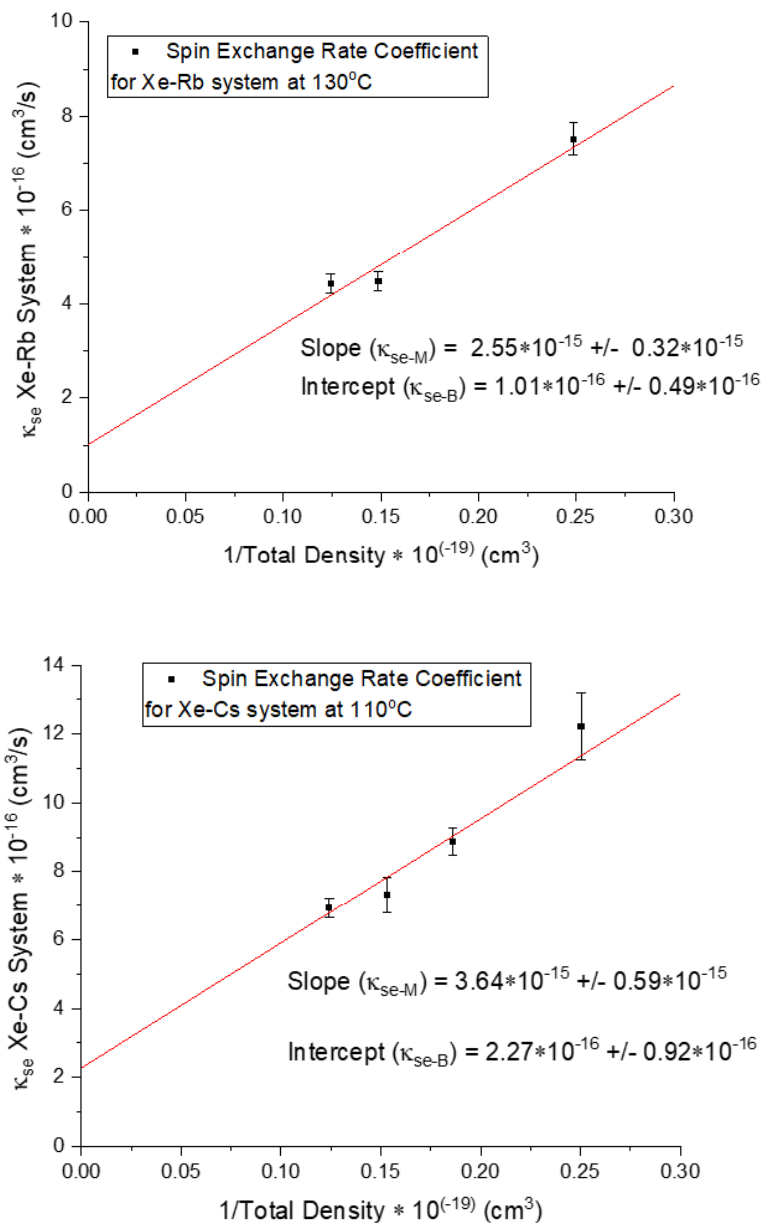


Figure 5.13: Xe-Rb and Xe-Cs spin-exchange rate coefficient vs. $1/\text{total density}$. The parameters of the linear fit will provide us with information about the contributions of binary collisions and van der Waals molecules to the spin-exchange process.

systems (Fig. 5.14).

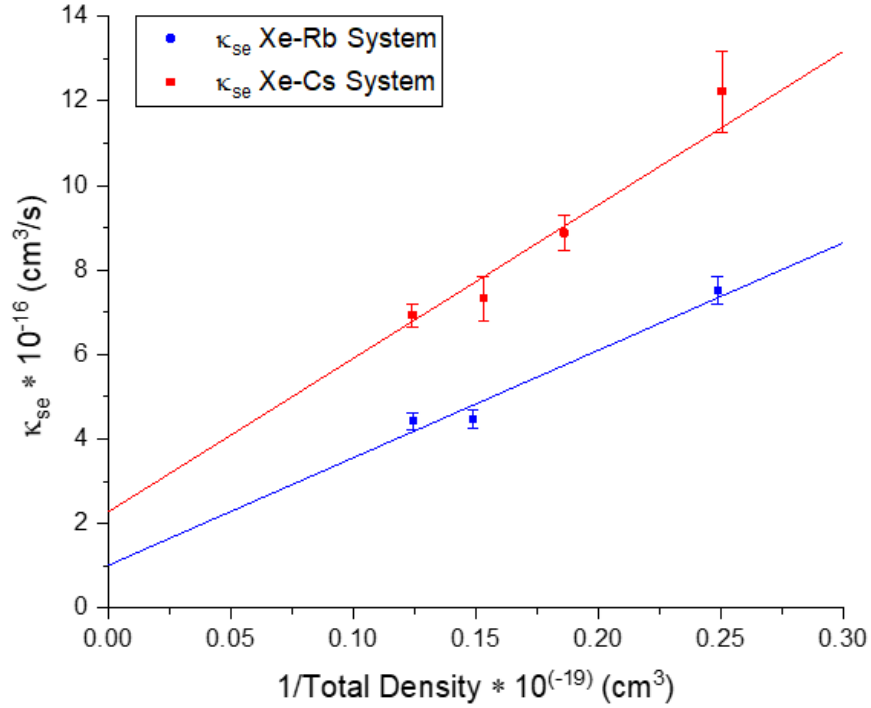


Figure 5.14: Spin-exchange rate coefficient for Xe-Rb and Xe-Cs systems vs. 1/total density on the same graph. It suggests that at any corresponding total density and respective temperatures k_{se} for Xe-Cs system is larger than Xe-Rb system.

The data plotted in Fig. 5.14 shows that the Xe-Cs system seems to have a higher spin-exchange rate coefficient than the Xe-Rb system by $\sim 35\%$, which may suggest that Cs is a better candidate for spin-exchange optical pumping process to polarize Xe, but by referring to the electron-randomization rate vs. density figure (Fig. 4.12), where it suggested that Cs has a larger electron-randomization rate than Rb, one can see that this will cancel the effect of the higher spin-exchange rate coefficient to some

extent.

5.5 Conclusion

We measured the alkali-metal spin-exchange rate coefficient for both Xe-Rb and Xe-Cs systems for a fixed gas composition of 94% ^4He , 3% N_2 and 3% Xe over the total gas density range of 1.5-3 amagat. We found out that the spin-exchange rate coefficient k_{se} for the Xe-Rb system is $\sim 35 - 40\%$ lower than the spin-exchange rate coefficient for Xe-Cs system (table 5.3), $k_{\text{se,Xe-Rb}} \sim 0.63 k_{\text{se,Xe-Cs}}$. Our values for the binary piece of k_{se} is comparable to values that exists in the literature [69, 73], and any discrepancies may arise from the different magnetic field B_0 , temperature, gas composition, and total gas densities since the value of k_{se} depends on the Xe partial pressure. By this comparison between Xe-Rb and Xe-Cs systems, one may suggest that since the k_{se} for the Xe-Cs system is larger than the one for the Xe-Rb system, Cs can be a better partner for polarizing Xe. But in order to decide which alkali-metal is better for polarizing Xe, it is best to refer to the spin-exchange efficiency, which will take into account both the spin-exchange rate coefficient and the alkali-metal electron-randomization effects.

$$\eta_{\text{se}} = \frac{\gamma_{\text{se}}/[\text{A}]}{\Gamma_{\text{A}}^{(\text{Xe})}/[\text{Xe}]} = \frac{\gamma_{\text{se}}[\text{Xe}]}{\Gamma_{\text{A}}^{(\text{Xe})}[\text{A}]} = \frac{k_{\text{se}}[\text{Xe}]}{\Gamma_{\text{A}}^{(\text{Xe})}} \quad (5.23)$$

We used the values for k_{se} and $[\text{Xe}]$ from table 5.3 and $\Gamma_{\text{A}}^{(\text{Xe})}$ from table 5.2 and Eq.

5.23 to get the spin-exchange efficiency for both systems. The values are reported in the table 5.4.

Cell	η_{se}
309A (Rb)	0.0604 ± 0.0035
309C (Rb)	0.0475 ± 0.0024
309D (Rb)	0.0471 ± 0.0023
310A (Cs)	0.0789 ± 0.0067
310B (Cs)	0.0687 ± 0.0034
310C (Cs)	0.0567 ± 0.0041
310D (Cs)	0.0591 ± 0.0024

Table 5.4: Calculated values of spin-exchange efficiency η_{se} .

The values in table 5.4 suggest that Cs has slightly better spin-exchange efficiency than Rb in our experimental regime, commonly seen in magnetic resonance imaging polarizers, but not dramatically better to imply the absolute idea of Cs being inherently the best partner for polarizing Xe. However one may conclude that Cs is a better partner due to its other practical advantages, like having $\sim 12\%$ more photons per watt of D_1 laser power, and at a given temperature it has a higher vapor pressure than Rb.

CHAPTER 6

SUMMARY AND CONCLUSION

In this dissertation, in Brian Saam's lab, I had the opportunity to investigate the alkali-metal-noble gas spin-exchange efficiency for Xe-Rb and Xe-Cs systems. For that, there were two principal quantities that needed to be studied and measured experimentally. The alkali-metal spin-destruction or the electron-randomization rates, and the alkali-metal-noble gas spin-exchange rate coefficient. The motivation behind doing these studies was the absence of experimental studies on these quantities for Xe-Cs. Second, the studies on the Xe-Rb system needed a fresh revisit due to the different and inconsistent reported values. Last, but not least, Rb was the alkali-metal of choice for the SEOP process to polarize noble gas atoms like Xe, and this comparison between the two systems of Xe-Rb and Xe-Cs, was needed to know which alkali-metal serves as a better agent for SEOP and polarizing Xe.

In the second chapter, I presented a brief and overall description of the SEOP theory and different pieces of it like alkali-metal magnetic resonance, the alkali-metal spin-destruction, and the alkali-metal-noble gas spin-exchange.

In Chapter 3, I described our general apparatus for the relaxation in the dark measurement for studying the alkali-metal spin-destruction rate and the alkali-metal frequency shift measurements for studying the alkali-metal-noble gas spin-exchange rate coefficient.

The fourth chapter, presents our work on the measurement of the alkali-metals Rb and Cs spin-destruction and electron-randomization rates. We did the so-called ‘relaxation in the dark’ measurement using the pulsed EPR technique. We got the results that γ_A for Cs is $\sim 30 - 40\%$ smaller than γ_A for Rb, but taking into account that effect of the paramagnetic coefficient ϵ or the slowing down factor ε , we got the electron-randomization rate Γ_A for both Rb and Cs. Γ_{Rb} came out to be $\sim 30\%$ smaller than Γ_{Cs} due to the difference in the values of ε ($\varepsilon_{\text{Rb(nat.)}} = 10.8$ and $\varepsilon_{\text{Cs}} = 22$), suggesting that Cs has a bigger electron-randomization rate than Rb, and hence a slower polarization decay.

In Chapter 5, we studied the other piece to the spin-exchange efficiency η_{se} which is the spin-exchange rate coefficient for both Xe-Rb and Xe-Cs systems. For measuring the k_{se} we had to measure Xe polarization for which we utilized the alkali-metal EPR frequency shift measurement due to polarized Xe. Our experimental results of k_{se} suggested that the Xe-Rb system has $\sim 30 - 40\%$ smaller spin-exchange rate coefficient compared to the Xe-Cs system, which was comparable to the existing results in the literature.

By taking into account the results for both experiments and knowing the values for Γ_A and k_{se} for both systems, we calculated the efficiency for these systems. The results showed that Cs may have a better SEOP efficiency than Rb by $\sim 20 - 30\%$, suggesting that Cs may be a better partner for polarizing Xe. Besides the results

of SEOP efficiency, Cs has other advantages compared to Rb such as higher vapor pressure at a given temperature and $\sim 12\%$ more photons per watt of D_1 laser power.

The entire project detailed in this dissertation was started with the intention of better understanding the physics involved in the SEOP as well as making useful contributions to the field.

REFERENCES

- [1] Y.-Y. Jau et al. “Intense, Narrow Atomic-Clock Resonances”. In: *Phys. Rev. Lett.* 92.11 (Mar. 2004), p. 110801.
- [2] J. C. Allred et al. “High-Sensitivity Atomic Magnetometer Unaffected by Spin-Exchange Relaxation”. In: *Phys. Rev. Lett.* 89.13 (Sept. 2002), p. 130801.
- [3] Ana-Maria Oros and N Jon Shah. “Hyperpolarized xenon in NMR and MRI”. In: *Phys. Med. Biol.* 49.20 (Sept. 2004), R105–R153.
- [4] M. S. Rosen et al. “Polarized Xe129 optical pumping/spin exchange and delivery system for magnetic resonance spectroscopy and imaging studies”. In: *Rev. Sci. Instrum.* 70.2 (Feb. 1999), pp. 1546–1552.
- [5] H. Batelaan et al. “Optically Pumped Electron Spin Filter”. In: *Phys. Rev. Lett.* 82.21 (May 1999), pp. 4216–4219.
- [6] M. S. Albert et al. “Biological magnetic resonance imaging using laser-polarized ^{129}Xe ”. In: *Nature* 370.6486 (July 1994), pp. 199–201.
- [7] D. Rafferty et al. “High-field NMR of adsorbed xenon polarized by laser pumping”. In: *Phys. Rev. Lett.* 66.5 (Feb. 1991), pp. 584–587.
- [8] J P Butler et al. “Measuring surface-area-to-volume ratios in soft porous materials using laser-polarized xenon interphase exchange nuclear magnetic resonance”. In: *J. Phys.: Condens. Matter* 14.13 (Mar. 2002), pp. L297–L304.
- [9] M. V. Romalis and M. P. Ledbetter. “Transverse Spin Relaxation in Liquid ^{129}Xe in the Presence of Large Dipolar Fields”. In: *Phys. Rev. Lett.* 87 (6 July 2001), p. 067601.
- [10] B.M. Goodson et al. “The Physics of Hyperpolarized Gas MRI”. In: *Hyperpolarized and Inert Gas MRI*. Elsevier, 2017, pp. 23–46.
- [11] Boyd M. Goodson et al. *Hyperpolarization Methods for MRS*. Dec. 2015.
- [12] W. Happer et al. “Polarization of the nuclear spins of noble-gas atoms by spin exchange with optically pumped alkali-metal atoms”. In: *Phys. Rev. A* 29.6 (June 1984), pp. 3092–3110.
- [13] S. Appelt et al. “Theory of spin-exchange optical pumping of ^3He and ^{129}Xe ”. In: *Phys. Rev. A* 58.2 (Aug. 1998), pp. 1412–1439.

- [14] C. H. Volk, T. M. Kwon, and J. G. Mark. “Measurement of the ^{87}Rb - ^{129}Xe spin-exchange cross section”. In: *Phys. Rev. A* 21.5 (May 1980), pp. 1549–1555.
- [15] Eric G Sorte. *Investigation of a new model of dipolar-coupled nuclear spin relaxation and applications of dynamic nuclear polarization*. The University of Utah, 2011.
- [16] Jan H. Ardenkjær-Larsen et al. “Increase in signal-to-noise ratio of $> 10,000$ times in liquid-state NMR”. In: *Proc. Natl. Acad. Sci.* 100.18 (Aug. 2003), pp. 10158–10163.
- [17] Kan-Nian Hu et al. “High-frequency dynamic nuclear polarization using mixtures of TEMPO and trityl radicals”. In: *J. Chem. Phys.* 126.4 (Jan. 2007), p. 044512.
- [18] Kent R. Thurber and Robert Tycko. “Theory for cross effect dynamic nuclear polarization under magic-angle spinning in solid state nuclear magnetic resonance: The importance of level crossings”. In: *J. Chem. Phys.* 137.8 (Aug. 2012), p. 084508.
- [19] Andrea Capozzi et al. “Optimal Glass-Forming Solvent Brings Sublimation Dynamic Nuclear Polarization to ^{129}Xe Hyperpolarization Biomedical Imaging Standards”. In: *The Journal of Physical Chemistry C* 119.9 (Feb. 2015), pp. 5020–5025.
- [20] Alfred Kastler. “Optical Methods of Atomic Orientation and of Magnetic Resonance”. In: *J. Opt. Soc. Am.* 47.6 (June 1957), p. 460.
- [21] F. D. Colegrove and P. A. Franken. “Optical Pumping of Helium in the 3S_1 Metastable State”. In: *Phys. Rev.* 119 (2 July 1960), pp. 680–690.
- [22] F. D. Colegrove, L. D. Schearer, and G. K. Walters. “Polarization of He^3 Gas by Optical Pumping”. In: *Phys. Rev.* 132 (6 Dec. 1963), pp. 2561–2572.
- [23] Tetsuo Hadeishi and Chung-Heng Liu. “Nuclear Alignment of the 1S_0 Ground State of ^{131}Xe by Electron Pumping and Metastability-Exchange Collisions”. In: *Phys. Rev. Lett.* 19 (5 July 1967), pp. 211–213.
- [24] V Lefevre-Seguin and M Leduc. “Metastability-exchange and depolarising collisions in xenon and krypton”. In: *J. Phys. B: At. Mol. Phys.* 10.11 (Aug. 1977), pp. 2157–2164.

- [25] Louis-S. Bouchard et al. “NMR Imaging of Catalytic Hydrogenation in Microreactors with the Use of para-Hydrogen”. In: *Science* 319.5862 (Jan. 2008), pp. 442–445.
- [26] M. A. Bouchiat, T. R. Carver, and C. M. Varnum. “Nuclear Polarization in He³ Gas Induced by Optical Pumping and Dipolar Exchange”. In: *Phys. Rev. Lett.* 5 (8 Oct. 1960), pp. 373–375.
- [27] B. C. Grover. “Noble-Gas NMR Detection through Noble-Gas-Rubidium Hyperfine Contact Interaction”. In: *Phys. Rev. Lett.* 40.6 (Feb. 1978), pp. 391–392.
- [28] G. D. Cates et al. “Rb–¹²⁹Xe spin-exchange rates due to binary and three-body collisions at high Xe pressures”. In: *Phys. Rev. A* 45.7 (Apr. 1992), pp. 4631–4639.
- [29] Thad G. Walker and William Happer. “Spin-exchange optical pumping of noble-gas nuclei”. In: *Rev. Mod. Phys.* 69.2 (Apr. 1997), pp. 629–642.
- [30] Thad G Walker. “Fundamentals of Spin-Exchange Optical Pumping”. In: *J. Phys: Conf. Ser.* 294 (June 2011), p. 012001.
- [31] T. E. Chupp et al. “Polarized, high-density, gaseous ³He targets”. In: *Phys. Rev. C* 36 (6 Dec. 1987), pp. 2244–2251.
- [32] C. D. Jeffries. *Dynamic nuclear orientation*. New York, Interscience Publishers, 1963.
- [33] W.Th. Wenckebach, T.J.B. Swanenburg, and N.J. Poulis. “Thermodynamics of spin systems in paramagnetic crystals”. In: *Phys. Rep.* 14.5 (Nov. 1974), pp. 181–255.
- [34] I. A. Nelson and T. G. Walker. “Rb-Xe spin relaxation in dilute Xe mixtures”. In: *Phys. Rev. A* 65.1 (Dec. 2001), p. 012712.
- [35] WILLIAM HAPPER. “Optical Pumping”. In: *Rev. Mod. Phys.* 44.2 (Apr. 1972), pp. 169–249.
- [36] David J. Griffiths. *Introduction to Quantum Mechanics*. Cambridge University Press, 2016, p. 465. ISBN: 9781107179868.
- [37] Mark E. Limes. *¹²⁹Xe Relaxation and Rabi Oscillations*. Springer International Publishing, 2015.

- [38] Richard P. Feynman. *Statistical Mechanics*. CRC Press, Mar. 2018.
- [39] G. Breit and I. I. Rabi. “Measurement of Nuclear Spin”. In: *Phys. Rev.* 38.11 (Dec. 1931), pp. 2082–2083.
- [40] Zayd Ma. *Frequency shifts during spin-exchange optical pumping of ^3He and ^{129}Xe and applications of hyperpolarized ^{129}Xe* . University of Utah, 2012.
- [41] Alfred Kastler. “Quelques suggestions concernant la production optique et la détection optique d’une inégalité de population des niveaux de quantification spatiale des atomes. Application à l’expérience de Stern et Gerlach et à la résonance magnétique”. In: *J. Phys. Radium* 11.6 (1950), pp. 255–265.
- [42] W. Happer and W. A. Van Wijngaarden. “An optical pumping primer”. In: *Hyperfine Interact.* 38.1-4 (Dec. 1987), pp. 435–470.
- [43] Earl Babcock. *Spin-exchange optical pumping with alkali-metal vapors*. University of Wisconsin-Madison, 2005.
- [44] A. R. Young et al. “Three-dimensional imaging of spin polarization of alkali-metal vapor in optical pumping cells”. In: *Appl. Phys. Lett.* 70.23 (June 1997), pp. 3081–3083.
- [45] A. Ben-Amar Baranga et al. “Alkali-metal-atom polarization imaging in high-pressure optical-pumping cells”. In: *Phys. Rev. A* 58.3 (Sept. 1998), pp. 2282–2294.
- [46] Charles P. Slichter. *Principles of magnetic resonance*. Springer-Verlag, 1978, p. 397. ISBN: 0387084762.
- [47] A. Ben-Amar Baranga et al. “Polarization of ^3He by Spin Exchange with Optically Pumped Rb and K Vapors”. In: *Phys. Rev. Lett.* 80.13 (Mar. 1998), pp. 2801–2804.
- [48] L. Wilmer Anderson, Francis M. Pipkin, and James C. Baird. “ N^{14} - N^{15} Hyperfine Anomaly,” in: *Phys. Rev.* 116.1 (Oct. 1959), pp. 87–98.
- [49] W. Franzen. “Spin Relaxation of Optically Aligned Rubidium Vapor”. In: *Phys. Rev.* 115.4 (Aug. 1959), pp. 850–856.
- [50] Adrian Biran and Rubén López-Pulido. “Basic Ship Hydrostatics”. In: *Ship Hydrostatics and Stability*. Elsevier, 2014, pp. 23–75.

- [51] A. I. Nahlawi et al. “High-precision determination of the frequency-shift enhancement factor in Rb- ^{129}Xe ”. In: *Phys. Rev. A* 100.5 (Nov. 2019), p. 053415.
- [52] B. Driehuys et al. “High-volume production of laser-polarized ^{129}Xe ”. In: *Appl. Phys. Lett.* 69.12 (Sept. 1996), pp. 1668–1670.
- [53] M. V. Romalis, E. Miron, and G. D. Cates. “Pressure broadening of Rb D_1 and D_2 lines by ^3He , ^4He , N_2 , and Xe : Line cores and near wings”. In: *Phys. Rev. A* 56.6 (Dec. 1997), pp. 4569–4578.
- [54] J. N. Zerger et al. “Polarization of ^{129}Xe with high power external-cavity laser diode arrays”. In: *Appl. Phys. Lett.* 76.14 (Apr. 2000), pp. 1798–1800.
- [55] M. V. Romalis. “Narrowing of high power diode laser arrays using reflection feedback from an etalon”. In: *Appl. Phys. Lett.* 77.8 (Aug. 2000), pp. 1080–1081.
- [56] B. Chann, I. Nelson, and T. G. Walker. “Frequency-narrowed external-cavity diode-laser-array bar”. In: *Optics Letters* 25.18 (Sept. 2000), p. 1352.
- [57] M. Kristensen, M. A. van Eijkelenborg, and J. P. Woerdman. “Faraday effect as a probe of hindered electronic precession in atoms”. In: *Phys. Rev. Lett.* 72.14 (Apr. 1994), pp. 2155–2158.
- [58] E. Vliegen et al. “Faraday rotation density measurements of optically thick alkali metal vapors”. In: *Nuclear Instruments and Methods in Physics Research Section A: Accelerators, Spectrometers, Detectors and Associated Equipment* 460.2-3 (Mar. 2001), pp. 444–450.
- [59] Z. Wu et al. “Optical determination of alkali metal vapor number density using Faraday rotation”. In: *Appl. Opt.* 25.23 (Dec. 1986), p. 4483.
- [60] J. Pascale and J. Vandeplanque. “Excited molecular terms of the alkali-rare gas atom pairs”. In: *J. Chem. Phys.* 60.6 (Mar. 1974), pp. 2278–2289.
- [61] Bien Chann. *Studies of spin-exchange optical pumping*. University of Wisconsin - Madison, 2003.
- [62] Ian Andrew Nelson. *Physics of practical spin-exchange optical pumping*. University of Wisconsin, Madison, 2001.
- [63] Thad G. Walker. “Estimates of spin-exchange parameters for alkali-metal-noble-gas pairs”. In: *Phys. Rev. A* 40.9 (Nov. 1989), pp. 4959–4964.

- [64] Hunter Middleton et al. “MR Imaging with Hyperpolarized³He Gas”. In: *Magn. Reson. Med.* 33.2 (Feb. 1995), pp. 271–275.
- [65] J R MacFall et al. “Human lung air spaces: potential for MR imaging with hyperpolarized He-3.” In: *Radiology* 200.2 (Aug. 1996), pp. 553–558.
- [66] Z. Wu et al. “Experimental studies of wall interactions of adsorbed spin-polarized ¹³¹Xe nuclei”. In: *Phys. Rev. A* 42.5 (Sept. 1990), pp. 2774–2784.
- [67] M. P. Ledbetter and M. V. Romalis. “Nonlinear Effects from Dipolar Interactions in Hyperpolarized Liquid ¹²⁹Xe”. In: *Phys. Rev. Lett.* 89.28 (Dec. 2002), p. 287601.
- [68] Xin Zhou. “Hyperpolarized Noble Gases as Contrast Agents”. In: *Methods in Molecular Biology*. Humana Press, 2011, pp. 189–204.
- [69] Yuan-Yu Jau, Nicholas N. Kuzma, and William Happer. “High-field measurement of the ¹²⁹Xe-Rb spin-exchange rate due to binary collisions”. In: *Phys. Rev. A* 66.5 (Nov. 2002), p. 052710.
- [70] X. Zeng et al. “Experimental determination of the rate constants for spin exchange between optically pumped K, Rb, and Cs atoms and ¹²⁹Xe nuclei in alkali-metal–noble-gas van der Waals molecules”. In: *Phys. Rev. A* 31.1 (Jan. 1985), pp. 260–278.
- [71] D. Levron et al. “Magnetic resonance imaging of hyperpolarized ¹²⁹Xe produced by spin exchange with diode-laser pumped Cs”. In: *Appl. Phys. Lett.* 73.18 (Nov. 1998), pp. 2666–2668.
- [72] D. K. Walter, W. Happer, and T. G. Walker. “Estimates of the relative magnitudes of the isotropic and anisotropic magnetic-dipole hyperfine interactions in alkali-metal–noble-gas systems”. In: *Phys. Rev. A* 58.5 (Nov. 1998), pp. 3642–3653.
- [73] Yuan-Yu Jau, Nicholas N. Kuzma, and William Happer. “Measurement of ¹²⁹Xe-Cs binary spin-exchange rate coefficient”. In: *Phys. Rev. A* 69.6 (June 2004), p. 061401.
- [74] Matthew P Augustine and Kurt W Zilm. “Optical pumping magnetic resonance in high magnetic fields: Measurement of high field spin exchange cross sections”. In: *Chem. Phys. Lett.* 280.1-2 (Nov. 1997), pp. 24–30.

- [75] Julia Hsu, Z. Wu, and W. Happer. “Cs induced ^{129}Xe nuclear spin relaxation in N_2 and He buffer gases”. In: *Phys. Lett. A* 112.3-4 (Oct. 1985), pp. 141–145.
- [76] B. Patton, N. N. Kuzma, and W. Happer. “Chemical shift of hyperpolarized ^{129}Xe dissolved in liquid nitrogen”. In: *Phys. Rev. B* 65.2 (Dec. 2001), p. 020404.
- [77] B. Chann et al. “Measurements of ^3He spin-exchange rates”. In: *Phys. Rev. A* 66.3 (Sept. 2002), p. 032703.
- [78] B. Larson et al. “Optical pumping of Rb in the presence of high-pressure ^3He buffer gas”. In: *Phys. Rev. A* 44.5 (Sept. 1991), pp. 3108–3118.
- [79] K.P. Coulter et al. “Neutron polarization with polarized ^3He ”. In: *Nuclear Instruments and Methods in Physics Research Section A: Accelerators, Spectrometers, Detectors and Associated Equipment* 270.1 (July 1988), pp. 90–94.
- [80] S. R. Schaefer et al. “Frequency shifts of the magnetic-resonance spectrum of mixtures of nuclear spin-polarized noble gases and vapors of spin-polarized alkali-metal atoms”. In: *Phys. Rev. A* 39.11 (June 1989), pp. 5613–5623.
- [81] S. Zou et al. “Collisional electron paramagnetic resonance frequency shifts in Cs-Rb-Xe mixtures”. In: *Phys. Rev. A* 106.1 (July 2022), p. 012801.